EXPLORING ULTRAFAST QUANTUM DYNAMICS OF ELECTRONS BY ATTOSECOND TRANSIENT ABSORPTION

by

Chen-Ting Liao

A Dissertation Submitted to the Faculty of the

COLLEGE OF OPTICAL SCIENCES

In Partial Fulfillment of the Requirements
For the Degree of

DOCTOR OF PHILOSOPHY

In the Graduate College

THE UNIVERSITY OF ARIZONA

2017

THE UNIVERSITY OF ARIZONA
GRADUATE COLLEGE

As members of the Dissertation Committee, we certify that we have read the dissertation prepared by Chen-Ting Liao, titled *Exploring Ultrafast Quantum Dynamics of Electrons by Attosecond Transient Absorption* and recommend that it be accepted as fulfilling the dissertation requirement for the Degree of Doctor of Philosophy.

Arvinder Sandhu — Date: 20 April, 2017

R. Jason Jones — Date: 20 April, 2017

Khanh Kieu — Date: 20 April, 2017

Final approval and acceptance of this dissertation is contingent upon the candidate's submission of the final copies of the dissertation to the Graduate College.

I hereby certify that I have read this dissertation prepared under my direction and recommend that it be accepted as fulfilling the dissertation requirement.

Dissertation Director: Arvinder Sandhu — Date: 20 April, 2017

STATEMENT BY AUTHOR

This dissertation has been submitted in partial fulfillment of requirements for an advanced degree at the University of Arizona and is deposited in the University Library to be made available to borrowers under rules of the Library.

Brief quotations from this dissertation are allowable without special permission, provided that accurate acknowledgment of source is made. Requests for permission for extended quotation from or reproduction of this manuscript in whole or in part may be granted by the head of the major department or the Dean of the Graduate College when in his or her judgment the proposed use of the material is in the interests of scholarship. In all other instances, however, permission must be obtained from the author.

SIGNED: Chen-Ting Liao

ACKNOWLEDGEMENTS

This research work would not have been possible without the help and support of many individuals. I wish to express my sincere appreciation to the following parties.

First and foremost, to my advisor Prof. Arvinder Sandhu for his leadership and friendship. I would like to thank Arvinder for taking me in his research group since 2012 summer. He has been very helpful and inspiring throughout my graduate research, and he is always accessible for discussing all aspects of the research ideas, experimental implementation, and theoretical modeling. He also has been tremendously helpful in all kinds of my writings and oral preparations, providing just the right balance of guidance and patience.

I would like to recognize the contributions from our theorist collaborators Prof. Mette Gaarde and Prof. Kenneth Schafer from Louisiana State University, Prof. C. William McCurdy, Dr. Xuan Li, and Dr. D. Haxton from Lawrence Berkeley National Lab, Prof. Robert Lucchese from Texas A&M University, and Prof. Luca Argenti from the University of Central Florida. Their knowledge, insights, and theoretical calculations and simulations helped to guide and to shape my understanding of atomic and molecular physics, and their contributions were an integral portion of my dissertation work.

I am also grateful to Prof. R. Jason Jones and Prof. Khanh Kieu for serving as the members of my dissertation committee. I have learned a lot through their classes and labs, as well as private discussions in both science and career choices.

I would like to thank former lab members Niranjan Shivaram and Henry Timmers. They mentored me and were invaluable sources of knowledge in the lab about attosecond science and technology. Also, I would like to thank all of the graduate students and undergraduates I have worked with throughout my years in Sandhu Lab: Dheeraj Golla, Marc Bourgeois, Alex Plunkett, Nathan Harkema, Ian Arnold, Arpit Dave, Alexandra Brasington, and others. They provided support in my years in helping optical alignment, equipment setup, data acquisition, and result discussion. Our conversations in the office were wonderful distractions that helped to expand my understanding and viewpoints in both science and life.

I am grateful to my lovely fianceė, Huimin, for her relentless encouragement, company, and support throughout this journey. All our adventures in grad school and beyond are treasures that I keep dear in my heart. Lastly, I wish to express my heartfelt gratitude to my parents who raised me, inspire me, support me, and sculpted my character in a way that leads to who I am today.

DEDICATION

To all sentient and curious beings.
To all who love light.

TABLE OF CONTENTS

TABLE OF CONTENTS – *Continued*

TABLE OF CONTENTS – *Continued*

LIST OF FIGURES

LIST OF FIGURES – *Continued*

LIST OF FIGURES – *Continued*

LIST OF FIGURES – *Continued*

LIST OF FIGURES – *Continued*

LIST OF FIGURES – *Continued*

LIST OF FIGURES – *Continued*

LIST OF FIGURES – *Continued*

LIST OF FIGURES – *Continued*

LIST OF FIGURES – *Continued*

LIST OF TABLES

ABSTRACT

Quantum mechanical motion of electrons in atoms and molecules is at the heart of many photophysical and photochemical processes. As the natural timescale of electron dynamics is in the range of femtoseconds or shorter, ultrashort pulses are required to study such phenomena. The ultrashort pulse light-matter interaction at high intensity regime can however dramatically alter the atomic and molecular structures. Our current understanding of such transient electronic modification is far from complete, especially when complicated light-induced couplings are involved. In this dissertation, we investigated how a femtosecond strong-field pulse can control or modify the evolution of atomic or molecular polarization, representing electric dipole excitation in various systems. Extreme ultraviolet (XUV) attosecond pulse trains are used to coherently prepare superposition of excited states in various atomic and molecular systems. A subsequent phase-locked infrared (IR) femtosecond pulse is applied to perturb the dipoles, and transient changes in the transmitted XUV spectra are measured. This scheme is termed as XUV attosecond transient absorption spectroscopy. In the first study, we applied this technique to study the modification of Rydberg states in dilute helium gas. We observed several transient changes to the atomic structure, including the ac Stark shift, laser-induced quantum phase, laser-induced continuum structure, and quantum path interference. When the experiments were extended to the study of a dense helium gas sample, new spectral features in the absorption spectra emerged which cannot be explained by linear optical response models. We found that these absorption features arise from the interplay between the XUV resonant pulse propagation and the IR-imposed phase shift. A unified physical model was also developed to account for various scenarios. Extending our work to argon atoms, we studied how an external infrared field can be used to impulsively control different photo-excitation pathways and the transient

absorption lineshape of an otherwise isolated autoionizing state. It is found that by controlling the field polarization of the IR pulse, we can modify the transient absorption line shape from Fano-like to Lorentzian-like profiles. Unlike atoms, in our study of autoionizing states of the oxygen molecule, we observed both positive and negative optical density changes for states with different electronic symmetries. The predictions of two distinct and simplified dipole perturbation models were compared against both the experimental results and a full theoretical calculation in order to understand the origin of the sign of absorption change. We relate this symmetry-dependent sign change to the Fano parameters of static photoabsorption. The same approach was applied to study molecular nitrogen, in which we observed the decay dynamics of IR perturbed doubly-excited Rydberg states with many vibrational progressions. In addition, we also conducted experiments to investigate Rydberg state dynamics of other molecular systems such as carbon dioxide. In summary, we experimentally explored the ephemeral light-induced phenomena associated with excited states of atoms and molecules. These studies provide real-time information on ultrafast electronic processes and provide strategies for direct time-domain control of the light-matter interaction.

CHAPTER 1

Introduction

> "A ***kṣaṇa*** (Sanskrit), the shortest space of time, a moment, the 90th part of a thought and 4500th part of a minute, during which 90 or 100 are born and as many die," *Mahasangha-vinaya*, AD 400 [25]).

1.1 Time Matters: Ultrafast Science and Technology

How short is an instant? In a blink of an eye? In a flash? The answer has evolved with the tremendous advancement of electronic and optical technologies in recent decades, especially with the advent of ultrafast light pulses. In fact, the field of ultrafast science and technology can be dated back to 1878 when Eadweard Muybridge invented high-speed photography. At that time, he successfully filmed a galloping horse with his innovative work in freeze-frame photographic studies of motion in the millisecond timescale. What he had done was essentially controlling the shutter speed and limiting the exposure rate while using continuous light. Later in the 1930s, Harold Edgerton's development of high-intensity xenon flash lamp as a pulsed light source for illumination pushed the temporal resolution of high-speed imaging to microsecond resolution. This approach is distinctively different from what Eadweard Muybridge had done. Instead of controlling the shutter on the camera or the detector, Harold Edgerton was controlling the temporal signature of the light source. The work of these two scientists and engineers paved the way for future technological advancements that are essential for ultrafast science.

Starting from the 1960s, laser scientists and engineers have created ultrashort pulses of light that last only nanoseconds to picoseconds based on Q-switching (Hellwarth 1961 [26]) and modelocking (DeMaria *et al.* 1966 [27]) techniques. In the late 1970s, a femtosecond laser pulse was first demonstrated and applied to re-

search [28, 29]. Depending on event of interest, various time-resolved technologies have to be utilized to visualize and to freeze their motion in time, as illustrated in Fig. 1.1. Figure 1.1 shows the order of magnitude in temporal duration, and relevant events in that timescale, from the age of the observable universe in exaseconds to the natural timescale of electron motions in attoseconds. In the timescale of milliseconds, microseconds, to nanoseconds, high-speed motions can be directly observed by employing fast mechanical or electronic shutters with short detector exposures. Examples include galloping horses, a bullet through an apple, computer clock cycle (semiconductor based electronic switch), respectively. However, due to physical limitations, the response or switching rate of modern electronic devices cannot exceed tens of gigahertz (hundreds of picosecond). Although there is an electronic limit to how fast the exposure rates of detectors can be, state-of-the-art technologies overcome this limit by creating shorter optical bursts, which can be used as a strobe.

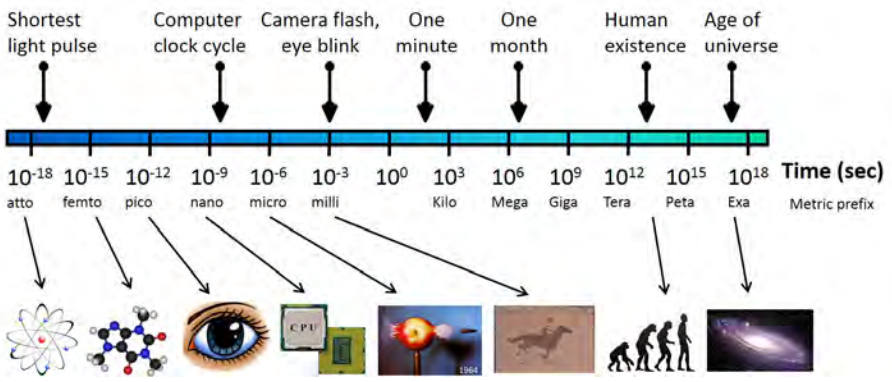

Figure 1.1: The order of magnitude in temporal duration and relevant events in that timescale.

After the 1980s, the development of convenient and powerful solid-state Ti:Sapphire lasers boosted both fundamental research as well as practical applications of femtosecond lasers. A notable research example is in the field of femtochemistry that continues with the theme of freezing events in time. Prof. Ahmed H. Zewail at Caltech won the 1999 Nobel Prize in Chemistry for his pioneering studies of the transition states of chemical reactions using femtosecond spectroscopy [30].

In this picosecond to femtosecond timescale, the dynamics of molecular vibration, rotation, and isomerization can be observed as schematically shown in Fig. 1.1. Outside research laboratories, femtosecond lasers have been extensively used in modern electronics industry for micromachining, and in medicine for laser-assisted surgeries.

After the invention of femtosecond lasers and their associated scientific achievements, it took more than 20 years to break the femtosecond barrier in temporal resolution. Thanks to the techniques such as chirped pulse amplification (CPA) [31] and Kerr lens modelocking (KLM), scientists generated few femtosecond laser pulses in the late 1990s [32]. Soon after the discovery of high harmonic generation (HHG) process in femtosecond strong-field regime [33, 34], researchers also proposed the creation of subfemtosecond pulses based on HHG in the 1990s. Combining the precision measurements of Hänsch's group [35] at the Max Planck Institute for Quantum Optics, and the ultrafast laser expertise of Krausz's group at the Technical University of Vienna, they and their colleagues successfully produced and measured attosecond pulses in 2001 (Hentschel *et al.,* 2001 [36]). Today, this advanced tabletop laser HHG source has enabled few-femtosecond to attosecond laser-like pulses, which opened a new research field called attosecond science.

1.2 Attosecond Science

Attosecond science, also known as attoscience, inherits the benefits of decades of research in ultrafast sciences, which utilizes ultrafast light sources to study atomic physics, molecular physics, physical chemistry, chemical physics, nonlinear optics, strong-field physics, condensed matter physics, material science, etc [37]. One of the shared aims in attosecond science community is to make molecular movies in real time [38]–monitoring the electron dynamics on their natural timescales. The research interests of the attosecond science community include the generation and characterization of shorter and stronger attosecond pulses (as in attosecond optics and attosecond photonics), as well as utilizing these pulses to study photodynamics (as in attosecond physics and attosecond chemistry).

Fifteen years into its inception, the attosecond technology is still evolving. Real attosecond-pump attosecond-probe experiments are still very difficult to perform due to the lack of high intensity or high flux attosecond sources [37, 39, 40]. One of the technical goals is to make the attosecond light sources stronger, by overcoming the low efficiency ($10^{-5} \sim 10^{-6}$) of HHG process. Also, many researchers aim to extend the photon energy of the extreme ultraviolet (XUV) attosecond source to soft X-ray range at hundreds of eV, and use the water window to explore biomolecules and materials using inner shell transitions. Recent efforts have focused on next-generation high-energy femtosecond laser development to achieve these goals. The new approaches include boosting driving laser power by thin-disk laser technologies [41], and constructing long-wavelength driving laser amplifiers in mid-infrared (MIR) by optical parametric chirped pulse amplification (OPCPA) technology [42].

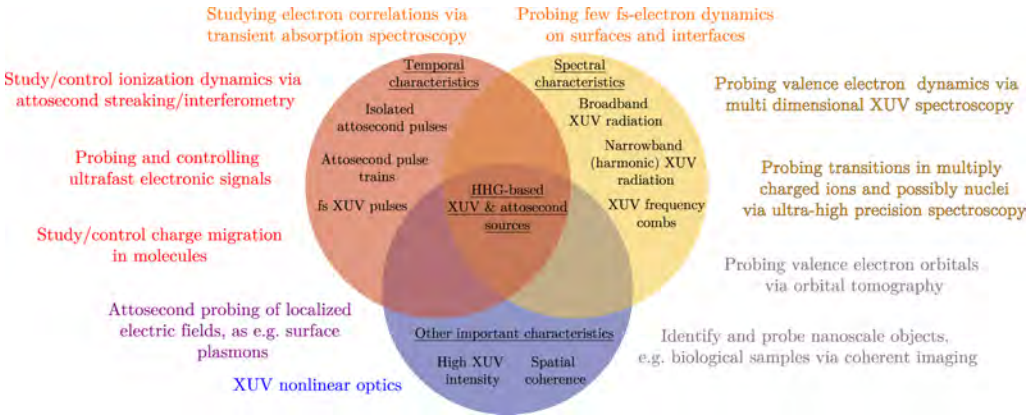

Figure 1.2: Current and future research directions for high-harmonic and attosecond sources, linked to the main source properties enabling the application, from R. Reid *et al.,* 2016. ©IOP Publishing. Reproduced with permission.

The attosecond science and technology have captured the rapidly growing imagination and expectations of the scientific communities in physics, chemistry, and material sciences with their promises of unveiling and manipulating fast-evolving photodynamics in nature. Figure 1.2 show an organized roadmap for current and future application directions of attosecond and HHG light sources reproduced from Ref. [43].

1.3 Quantum Dynamics of Photoabsorption

When light irradiates an atom or a molecule, many photo-initiated processes could happen such as excitation, fluorescence, phosphorescence, chemical transformation, conformational change, internal conversion, intramolecular charge transfer or migration, relaxation, etc. Although many of these general phenomena can be beautifully illustrated in Jablonski diagram, as shown in Fig. 1.3, detailed dynamics associated with these processes are not always known. The quantum mechanical motion of electrons in atoms and molecules and their interaction with light is at the heart of many photophysical and photochemical processes. Examples include light harvesting in photosynthesis [44], the prevention of ultraviolet (UV) radiation induced DNA damage by relaxation through conical intersections [45], and the initiation of vision through isomerization in Rhodopsin [46]. Such dynamical processes proceed through complicated couplings, that involve electrons, nuclei, holes, the external electromagnetic fields, or a mixture of above. However, many of these coupling parameters are usually not well understood, such as those responsible for connecting microscopic quantum dynamics to mesoscopic or macroscopic functions. Generally, it is very challenging to measure and to obtain information on electronic wave packet dynamics in complex and non-equilibrium systems, even with the techniques such as quantum process tomography [47].

Due to the fact that the natural electronic timescales range between attoseconds to few femtoseconds, ultrashort light sources are needed to probe these ultrafast processes. In addition, light sources that have short wavelengths of $\sim$100 nm–1 nm in the range of XUV to X-rays, present an opportunity to pinpoint the location of the dynamical processes on the spatial scale of nanometers. This new field is known as attosecond nanophysics or attosecond nanoscopy. In a widely used experimental procedure, an ultrafast pulse (pump pulse) prepares excited states, and then another ultrafast pulse (probe pulse) monitors, perturbs, or controls the following process. This methodology is termed pump-probe measurement or manipulation. One of the common approaches in this scheme is to use XUV attosecond pulse(s) combined

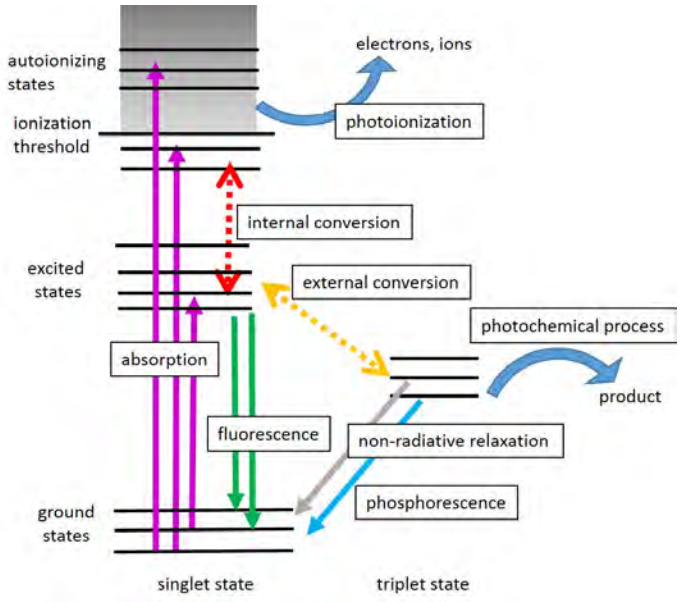

Figure 1.3: Light-matter interactions in an atom or a molecule illustrated in Jablonski diagram.

with a phase-locked and time-delayed near infrared (NIR) laser pulse to conduct temporally and energetically resolved spectroscopy.

As one of the most common forms of light-matter interaction, the photoabsorption of electromagnetic radiation in matter provides us rich information to understand the electronic structure of an atom or a molecule. Figure 1.4 shows simplified physical picture of possible photoabsorption processes in atoms, molecules, and solids from Ref. [1]. In spectroscopy or spectrophotometry, the optical density (OD), also termed absorbance, is usually measured to quantify optical absorption. The OD of a medium is a logarithmic ratio of the radiation transmitted through a target sample (I_t), to the radiation falling upon a target sample (I_0), i.e., $OD = -log_{10}(I_t/I_0)$ as in Fig. 1.5. In linear absorption regime, the Beer's law reads $I_t = I_0 e^{-a_t L}$, so the unitless OD can be written as $OD = (ln10)^{-1} a_t L = (ln10)^{-1} \sigma n L$, where L is the interaction length, n is the medium number density, a_t is the absorption or attenuation coefficient, and σ is the absorption cross section in the unit of area. The convenient unit of the cross section is in barn (b) or megabarn (Mb), where 1 Mb = 10^{-18} cm^2 = 10^{-22} m^2. The OD is also related to optical depth by a factor of $ln(10) \sim 2.3026$.

We can further write down absorption cross section as $\sigma(\omega) = 8\pi\alpha\omega Im[d(\omega)/\mathcal{E}(\omega)]$, where ω is the angular frequency or the energy (in atomic unit, a.u.), α is the fine-structure constant ($\alpha \sim 1/137$), Im represents imaginary part, $d(\omega)$ is the electric dipole moment, and $\mathcal{E}(\omega)$ is the electric field of incident radiation. Here we adapt semi-classical picture that the medium (an atom or a molecule) is treated quantum mechanically, and the light is treated classically as the electromagnetic wave.

Conventional static photoabsorption measurements using continuous light sources do not provide us temporal information. Therefore, one has to rely on ultrashort light pulses to resolve the photodynamics in a medium, and this approach is labeled time-resolved photoabsorption spectroscopy. In the time-domain picture, we can write time-dependent electric dipole as $d(t) = \langle\Psi_j(t)|d_{ij}|\Psi_i(t)\rangle$, and we can further relate this time-dependent dipole $d(t)$ to the conventional frequency-domain dipole $d(\omega)$ by the Fourier transform, namely, $\mathcal{F}[d(t)] = \int d(t)e^{-i\omega t}dt = d(\omega)$. The d_{ij} is the element of dipole moment, and $\Psi_j(t)$ and $\Psi_i(t)$ are time-dependent wavefunctions of j and i quantum states of our sample system of interest, respectively. Therefore, by resolving time-dependent absorption, the evolution of quantum wavefunction of the sample, namely, the quantum dynamics of photoexcited electrons in atoms and molecules, can be understood.

Ultrafast transient absorption spectroscopy utilizes a pump pulse and a probe pulse to temporally resolve and monitor absorption spectrum over time as shown in Fig. 1.5. Starting from the 1950s, Eigen, Norrish, and Porter *et al.* applied nanosecond transient absorption to study the dissociation process of molecular hydrogen iodide into a hydrogen and an iodine atom. There are many commercial nanosecond transient absorption spectrometers available. In the 1980s, picosecond and femtosecond transient absorption were developed, leading to the groundbreaking work by Nobel laureate A. Zewail. Today, there are many ongoing research efforts using femtosecond transient absorption [48] that strive to understand complicated electron dynamics in complex correlated systems, such as large biomolecules or proteins, or two-dimensional quantum materials such as graphene and transition metal dichalcogenide monolayers.

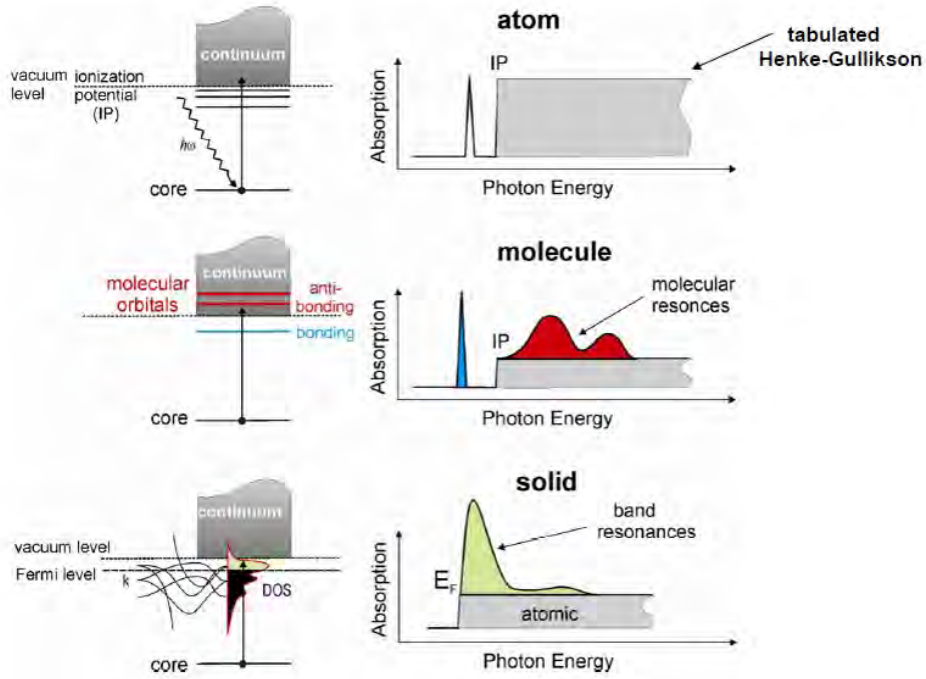

Figure 1.4: The photoabsorption process in atoms, molecules, and solids. Retrieved from J. Stöhr 1992, X-ray absorption spectra in a nutshell [1].

In attosecond science, one of the most successful and versatile techniques for measurement of electron dynamics relies on streak cameras, which measures photoelectron or photoions by pump-probe based attosecond streaking. This kind of measurement can be achieved by velocity map imaging (VMI) setup, magnetic bottles, etc. However, attosecond streaking has some weakness and limitations. For example, it intrinsically requires strong laser field that could distort the system under investigation, and the strong laser field can create a significant background of electrons through strong field ionization processes. Secondly, it detects charged fragments including electrons and ions, which limits measurement speed and signal-to-noise ratio [49]. Generally, the measurement scheme that relies on charge detection is susceptible to space-charge effects and distortions.

The attosecond transient absorption spectroscopy (ATAS), or the ATA spectroscopy, is the complementary all-optical approach in attosecond sciences, and it is a natural extension of femtosecond transient absorption spectroscopy. Since the first

demonstration of ATAS in resolving valence electron motion in krypton [50], ATAS has drawn lots attention to study atomic and molecular gases, liquid droplets and vapors, and condensed matter. In this dissertation, bulk of my research work focuses on applying ATAS to study ultrafast quantum dynamics of electrons in atoms and molecules.

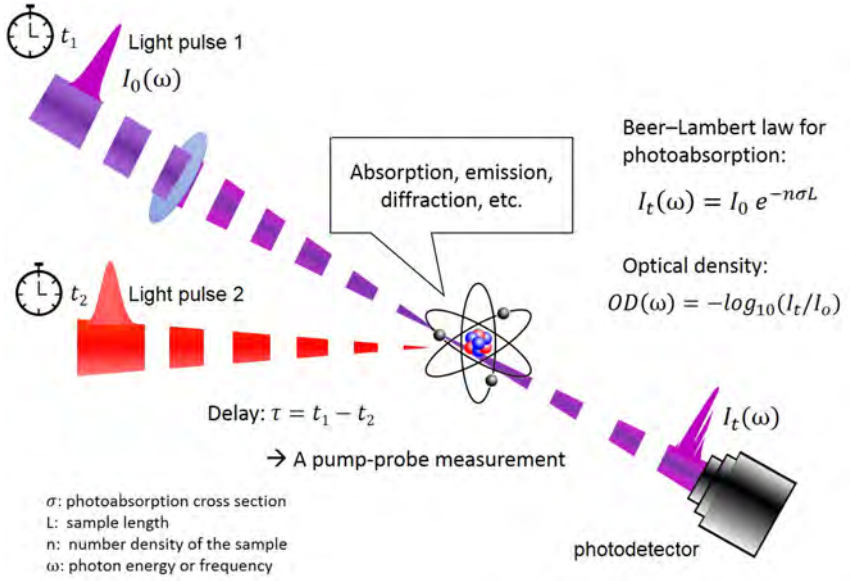

Figure 1.5: General experimental apparatus for transient photoabsorption spectroscopy.

CHAPTER 2

Experimental Methods and Setup

In this chapter, I will introduce general experimental setup and principles. First of all, I will discuss strong and ultrashort femtosecond laser pulse generation in visible (VIS) and near-infrared (NIR) range with pulse duration compression and wavelength conversion techniques by hollow-core fiber pulse compressor and optical parametric amplifier (OPA), respectively. I will also briefly discuss femtosecond pulse characterization techniques. Secondly, I will introduce the generation of laser-like extreme ultraviolet (XUV) attosecond pulses via high harmonic generation (HHG), which includes the creation of attosecond pulse trains (APTs) and the future implementation of isolated attosecond pulse (IAP) by optical gating. Also, I will introduce the technique to characterize attosecond pulses. In addition, I will also show APTs with even harmonics generation, and discuss the potential for the generation of circularly polarized harmonics. Following the ultrafast light source generation, manipulation and characterization, I will introduce the experimental apparatus to perform attosecond science, especially for the ATAS.

2.1 Femtosecond IR Laser System

2.1.1 Ti:sapphire Laser Oscillator and Amplifier

In our lab, we use a Kerr-lens modelocking based Ti:sapphire laser oscillator (Griffin-I, KM Labs) to generate $\sim$ 30 fs pulses at 78 MHz repetition rate with few nJ pulse energy, $\sim$ 400 mW averaged power, central wavelength $\lambda \sim 780$ nm, $\sim$ 40 nm bandwidth, without actively stabilized carrier-envelope phase (CEP). Our femtosecond laser oscillator is shown on the top portion of Fig. 2.1. This laser oscillator is pumped by a continuous-wave (cw) Nd:YAG laser (Verdi V6, Coherent). By adjusting the prism pair position in the oscillator, we can tune the central wavelength by $\sim$10

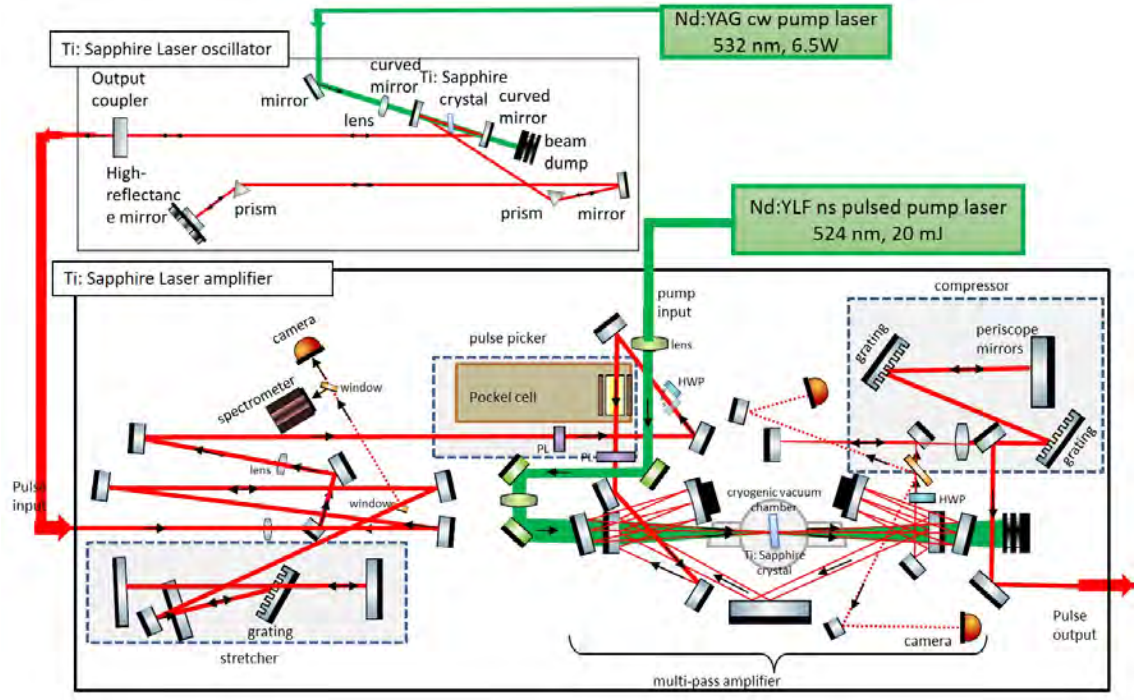

Figure 2.1: Schematic optical layout of the Ti:Sapphire laser system. The system includes a Ti:Sapphire femtosecond laser oscillator, pumped by a cw Nd:YAG laser, and a Ti:Sapphire single-stage multi-pass amplifier, pumped by a pulsed Nd:YLF laser.

nm to adjust XUV HHG central energy slightly for red-shifted or blue-shifted HHG spectrum.

The seeding pulse from the oscillator is sent to a single-pass cryo-cooled Ti:sapphire laser amplifier (Dragon, KM Labs), shown on the bottom portion of Fig. 2.1. The amplification is based on chirped pulse amplifier (CPA) technique. In the CPA process, a pulse is first chirped by a grating pair, and then sent into a Pockel cell. Our Pockel cell converts 78 MHz pulse trains to 1 kHz pulse trains. Then, the picked pulse is sent to a multi-pass amplification setup, namely, the ring. The ring utilizes a Ti:sapphire crystal cooled by liquid nitrogen and pumped by a ns pulsed Nd:YLF laser (Photonics Industries, DM30-527). The solid-state Nd:YLF laser has 20 W average power, with 170 ns pulse duration, and wavelength 527 nm. We usually use 9–11 passes in the ring to reach high power with one thousandth

contrast between amplified spontaneous emission (ASE) and the main pulse. The contrast can mainly be optimized by alignment of the Pockel cell, the multi-pass ring, and the arrival time of the pumping pulse. After being amplified in the ring, the pulse is then compressed by another grating pair. The amplified femtosecond pulse has a 30–40 fs pulse duration at 1 kHz repetition rate, 2 mJ pulse energy, 780 nm central wavelength, and without actively stabilized CEP.

2.1.2 Optical Parametric Amplifier (OPA)

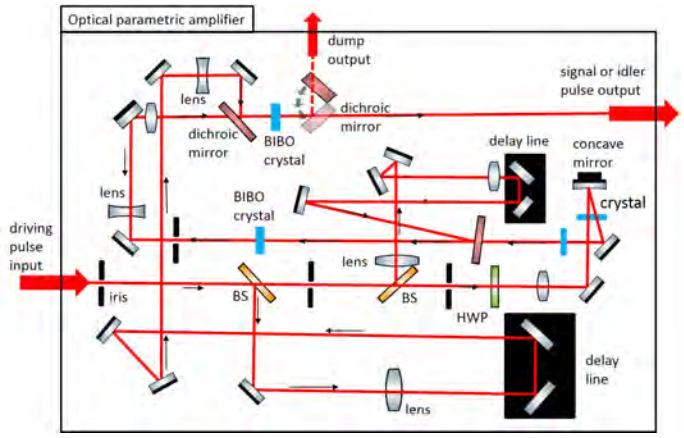

Figure 2.2: Schematic optical layout of the two-stage optical parametric amplifier (OPA).

In some experiments, an optical parametric amplifier (OPA) (Palitra-FS, Continuum) was used to convert NIR ($\lambda \sim 780$ nm) femtosecond pulse to longer wavelength at NIR to MIR range. Our OPA setup is shown in Fig. 2.2. The most efficient wavelength conversion range occurs when 1200—1800 nm wavelength was used. The highest efficiency of converting the input pumping power to the output signal power achieved by us is ~20%. This OPA is a two-stage collinear OPA. First, a small amount of energy from an amplified femtosecond pulse is split to generate white light continuum seeding pulse through a nonlinear crystal, and then the optical parametric generation (OPG) is implemented with the other femtosecond pulse to produce two output pulses with a lower frequency, called the signal and the idler. On the second state, the signal or the idler is further amplified through the

process of difference frequency generation. After doubling the frequency by a thin beta barium borate (BBO) crystal, the final output wavelength is measured by a spectrometer (SPM-002-X, PhotonControl). The shortest pulse duration from our OPA is ∼30 fs at ∼1500 nm when pumped by a ∼40 fs pulse at ∼780 nm pulse. The OPA pulse duration is also measured by our FROG setup.

2.1.3 Hollow-core Fiber (HCF) Pulse Compressor

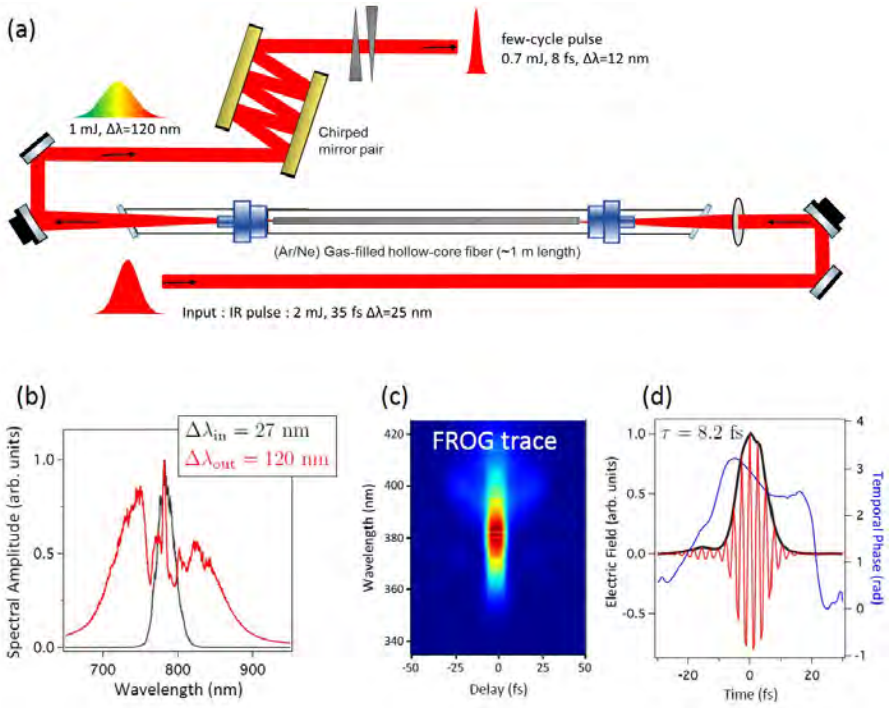

Figure 2.3: (a) Schematic setup of hollow core fiber (HCF) pulse compressor. (b) Spectra before and after the HCF, respectively. (c) Measured FROG trace of the few-cycle pulse. (d) Reconstructed field and phase from the few-cycle pulse.

Typical laser pulse duration from our Ti:sapphire amplifier is about 35–45 fs. In order to further shorten the pulse duration to generate few-cycle pulse, we build a gas-filled hollow-core fiber (HCF) setup as is shown in Fig. 2.3. First, a femtosecond pulse is focused and coupled into Argon or Neon gas-filled HCF, with fiber core diameter 250–750 um, 1 m in length. The highest coupling efficiency ∼ 60 % can be reached when the focused laser spot size is about 65% of core diameter. Due to the

self-phase modulation (SPM) process, the bandwidth of the input pulse is broaden to about 120 nm. After collimation, the output pulse is then compressed by chirped mirror pairs (Layertec) with 4–6 pairs of bounces, where each bounce provide group velocity dispersion (GVD) $\sim$ -45 fs^2 at λ $\sim$600–900 nm. Over broadened spectrum after the HCF is useless, since the bandwidth that our chirped mirrors can support is limited. In addition, too many bounces will produce multiple pulses because that chirped mirrors can only compensate group delay dispersion (GDD), but higher order terms. A thin fused silica wedge pair are also used after chirped mirrors to fine tune the GVD. The shortest few-cycle pulse we can generate so far is about 8 fs, which is equivalent to $\sim$3 optical cycles (o.c.) in 780 nm.

2.1.4 Characterization of Femtosecond Pulses by Frequency-resolved Optical Gating (FROG)

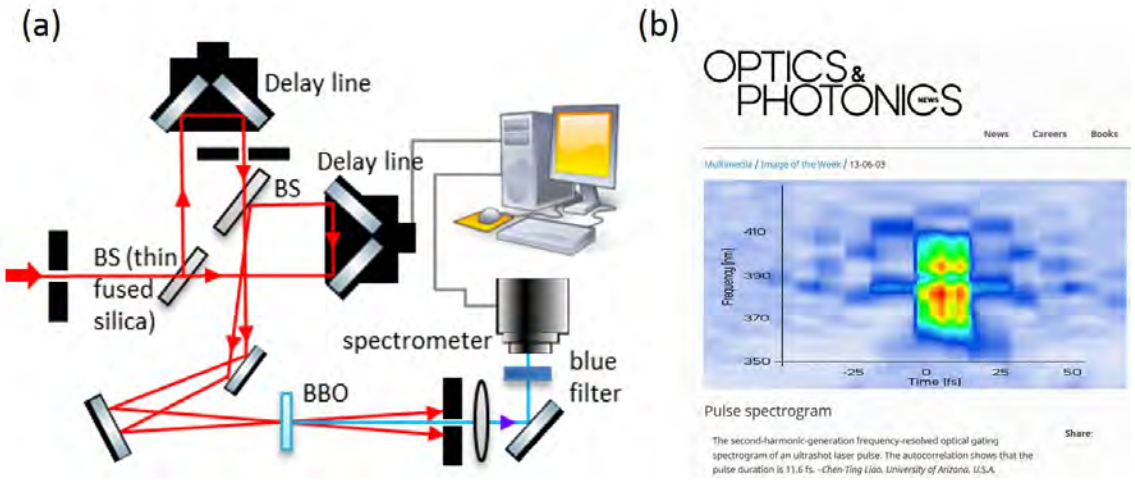

Figure 2.4: (a) Schematic optical layout of the home-made SHG FROG setup. (b) An example of a FROG spectrogram. Adapted from C.-T. Liao, Optics & Photonics News, 13-06-2013.

The speed of the electronics based photodetection with conventional oscilloscope (real-time oscilloscope) has only tens of GHz range sampling rate, so the optoelectronics can only measure nanosecond pulses. A state-of-the-art broadband sampling oscilloscope (equivalent-time sampling oscilloscope) measures picosecond pulses. As

a result, one has to use the autocorrelation techniques such as the self-referenced spectral interferometry to characterize femtosecond pulses from a laser oscillator, a laser amplifier, an OPA, or a HCF compressor. These techniques include the spectral phase interferometry for direct electric-field reconstruction (SPIDER), the frequency-resolved optical gating (FROG), the two-dimensional spectral shearing interferometry (2DSI), and the dispersion scan [51–54]. In our lab, we use second harmonic generation (SHG) FROG to characterize averaged femtosecond pulse duration as shown in Fig. 2.4. The FROG is a spectrally resolved autocorrelation technique, which measures self-referenced spectrograms as

$$S(\omega, t_d) = \int |\mathcal{E}_{SHG}(t)\mathcal{E}_{SHG}(t - t_d)e^{i\omega t}dt|^2, \tag{2.1}$$

where $E_{SHG}(t - t_d)$ is SHG signal from a thin BBO crystal at delay t_d.

A FROG spectrogram $S(\omega, t_d)$ (FROG trace) measured by the spectrometer is processed using a commercial iterative algorithm (FROG Pulse-Retrieval Code, Swamp Optics) to obtain the complete information of the laser pulse including the temporal phase and the electric field.

2.2 Attosecond XUV Pulse Generation

2.2.1 High Harmonic Generation (HHG) for Attosecond Pulse Trains (APTs)

In the process of HHG, a strong laser field with fundamental photon energy ω (usually in NIR range) is up-converted to weaker but higher harmonics $n\omega$ in VUV (vacuum ultraviolet) to XUV range (tens of eV to hundreds of eV in energy). Here, the upper range of n could be as large as hundreds. This process is very different compared to that in conventional nonlinear optics regime such as second ($n = 2$) or third harmonic generation ($n = 3$) process. The HHG process is sometimes termed extreme nonlinear optics. The laser intensity here ($>10^{14}$ W/cm^2) is considered strong when comparing to the Coulomb field of an atom. The Keldysh parameter, γ, can further quantify this, by defining the ratio of the laser frequency, ω, to the tunneling rate, Γ_t, or the ratio of the ionization (binding) energy, I_p, to the

ponderomotive energy, U_P. When $\gamma >> 1$ and $\gamma << 1$, the multiphoton process and the tunneling process dominate, respectively.

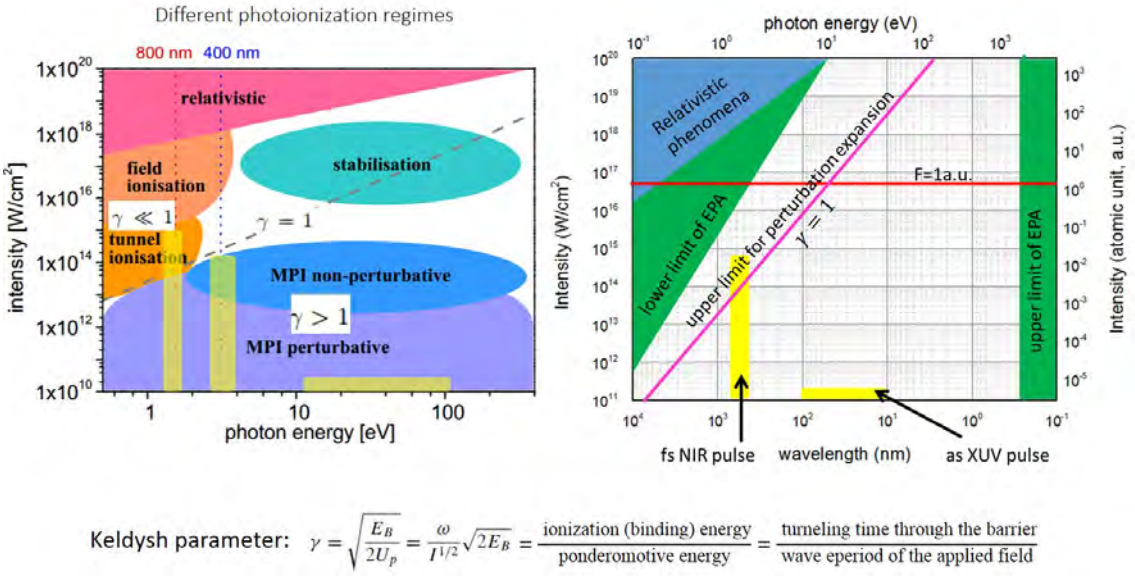

Figure 2.5: (a) Different photoionization regimes categorized by the Keldysh parameter. (b) Different approximation regimes categorized by the Keldysh parameter. Figures adapted from Ref. [2–6].

The HHG process can be understood classically as a simple three-step model illustrated in Fig. 2.6(a). The first step is the tunneling process of an electron leaving its nucleus. The tunneling rate is high when the strong laser field is comparable to Coulomb potential ($\sim 5\times10^9$ V/cm for a hydrogen atom) with laser peak intensity in the order of 10^{14} W/cm^2. This tunneling rate can be estimated based on Ammosov-Delone-Krainov (ADK) theory. The second step of HHG is the acceleration of the liberated electron due to the laser field in the first half laser cycle, and the electron will return when the laser field changes its sign during the second half cycle. There is small probability that the returning electron will collide and recombine with its parent nucleus, and this is the third step in HHG. The residual energy that electron gained in the laser field will be released in the form of VUV and XUV photons. The maximal energy, i.e., the cutoff energy, of the released photon is the sum of kinetic recollision energy, E_{KE}, and the binding energy or the pondermotive energy, U_P, of

the atom $\omega_{cut} = E_{KE} + 3.17U_P$, where $U_p = e^2\mathcal{E}^2/(4m\omega^2)$. Figure 2.5(a) shows different photoionization regimes, categorized by multi-photon ionization (MPI), field ionization, tunnel ionization, and among others. Figure 2.5(b) shows different range of validity of various approximations such as electric dipole approximation (EPA, also named long wavelength approximation) and the perturbation expansion [2–6].

Depending on the birth time and recollision time, we can categorize released and recombined electrons into short or long trajectories. This matters for macroscopic phase-matching conditions, and it relates the intrinsic chirping in the XUV attosecond bursts called attochirp. The electron recollision happens every half laser cycle, so the harmonics only include odd harmonics (n = 1,3,5,7,...) based on Fourier transform relation as shown in Fig. 2.6, which demonstrate attosecond bursts (attosecond pulse trains, APTs) generation. In this classical picture, we notice that when increasing driving laser wavelength, we can increase the energy gain of electrons and push cutoff energy higher. However, if we consider quantum mechanical picture regarding the wave nature of the electrons, the dispersion of electron wave packets will decrease the recollision probability and produce less XUV photon.

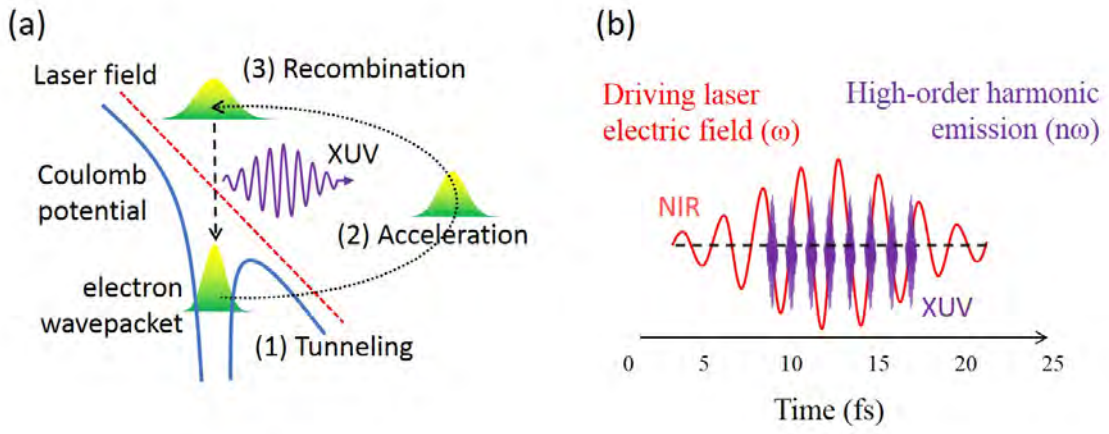

Figure 2.6: (a) The classical three-step model for the HHG. Three steps include tunneling, acceleration, and the recombination of liberated electron wavepackets in the superimposed laser and Coulomb fields. (b) A sketch of HHG-based APTs generation in the time-domain perspective.

2.2.2 HHG from a Hollow-core Waveguide and a Gas Cell

Above discussion on the HHG only considered the process from a single active electron (SAE) approximation. When generating XUV, one also has to take macroscopic conditions into account, such as phase-matching conditions. The simplified phase match condition for the HHG is [55]

$$k \sim \frac{2\pi}{\lambda} + \frac{2\pi N_a \delta(\lambda)}{\lambda} - N_e r_e \lambda - \frac{u_{nm}^2 \lambda}{4\pi a_{cor}^2}, \tag{2.2}$$

where λ is the driving laser wavelength, N_a is the density of neutral atoms, $\delta(\lambda)$ is the refractive index difference for the fundamental and the n-th harmonic, N_e is the electron density, r_e is classical electron radius, u_{nm} is the coefficient from Bessel function for different mode propagating in a waveguide, and a_{cor} is the inner core diameter of the waveguide. Thus, the first term is the wave vector of vacuum, and the second term is the wave vector in a neutral gas, the third term is from the free electron due to the ionization, and the last term is the contribution from a capillary waveguide geometry, which is absent when a gas cell is used. Essentially, when generating HHG, one would like to minimize the phase mismatch term $\Delta k = nk_0 - k_n$, where n is an integer number of n-th harmonics.

In our experiment, an NIR pulse is focused by a 500 mm focal length concave silver mirror into a gas-filled capillary waveguide or a gas cell for HHG as shown on Fig. 2.7. The waveguide is a hollow-core capillary glass capillary with 150 - 250 μm inner diameter, and 30 mm in length. There are two laser-drilled holes on the top of the waveguide as inlets of the gas. In addition to the waveguide, we also implement a gas cell setup to generate HHG. The geometry of the gas cell is designed as a semi-infinite gas cell (SIGC), where an aluminum foil or a thin aluminum plate can both be used as a gas-vacuum barrier with a hole drilled in situ by NIR pulse. In our design, the waveguide and the SIGC setup are interchangeable with least amount of disruption to the vacuum systems and optical alignment. A 200 nm thick aluminum thin film filter is used to block residual NIR pulse after a waveguide or a SIGC.

Depending on different gases introduced in the HHG chamber, we can produce

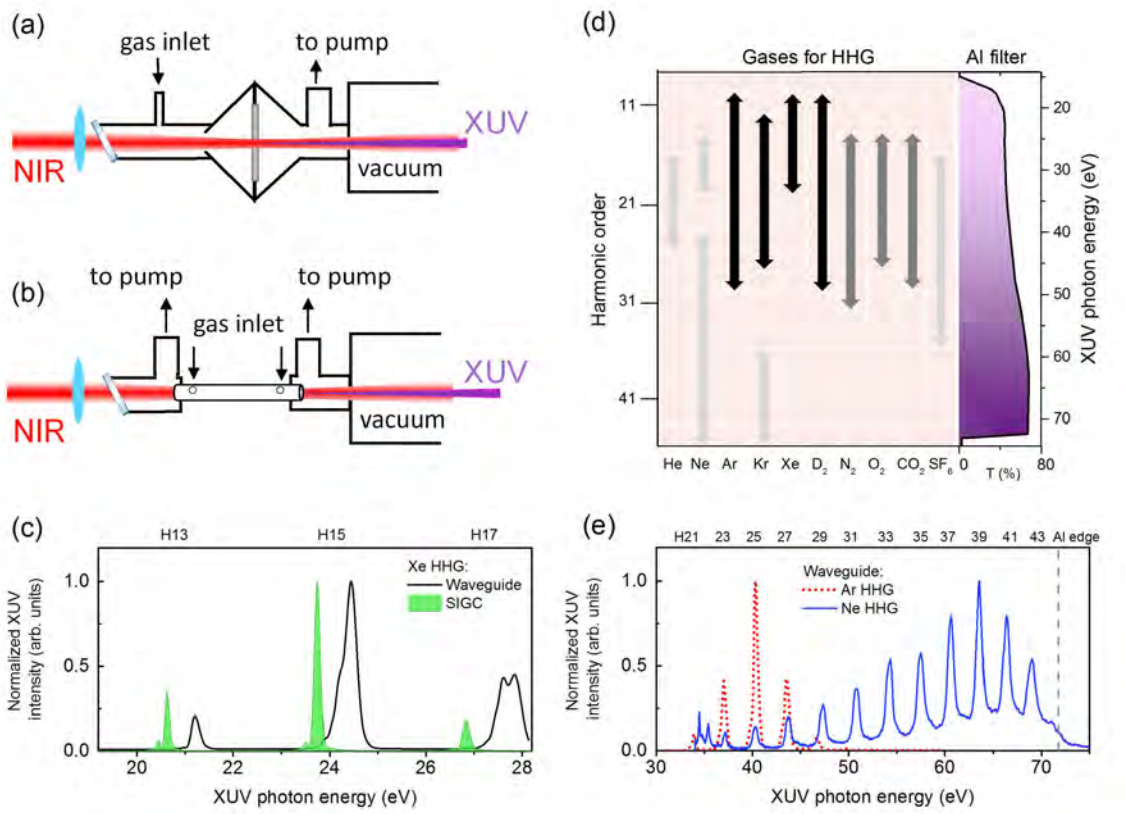

Figure 2.7: Schematic setup for HHG in (**a**) a semi-infinite gas cell (SIGC), and in (**b**) a gas-filled capillary waveguide. (**c**) Typical HHG spectra generated from Xe gas in a SIGC (green) and a waveguide (black), respectively. (**d**) Experimental survey of HHG spectral range from various gases based on our laser parameters and HHG setup. The aluminum filter transmission (T%) for XUV is shown on the side for reference. The length of the arrows indicate the spectral range in which we can generate reasonably strong XUV (few nJ per NIR pulse). Black, dark gray, and light gray arrows indicate relative intensity of the XUV emission. (**e**) Representative HHG spectra for higher XUV photon energies from Ar (red dotted) and Ne (blue solid) gases, respectively. This figure is adapted from Ref. [7]

XUV over a wide energy range with tunable harmonics in each case. A brief experimental survey on HHG spectra generated from many common gases is shown in Fig. 2.7(d). The length of the arrows in this figure represents the spectral range in which we can produce reasonably strong XUV, which is roughly at the level of few nJ per NIR pulse. The color (black, dark gray, light gray) of the arrows represents the relative spectral intensity of that XUV, from the strongest (black), moderately

strong (dark gray), to weak (light gray). We also show an aluminum filter transmission spectrum (T%) on the right-hand side of the Fig. 2.7(d), where we calculated the transmission assuming 2 nm Al_2O_3 oxidization layer on the top of 200 nm thick aluminum filter. The transmission data are calculated using CXRO data in Ref. [56]. Some representative HHG spectra covering the XUV energy range from 20 eV to 70 eV ($\sim$62 nm to 18 nm) are shown in Fig. 2.7(c) and (e).

The XUV emission is in the form of odd harmonics due to the centrosymmetric nature of atomic gases, where the nth harmonic will have photon energy $n\omega_{\text{NIR}}$, where ω_{NIR} is the fundamental driving NIR frequency corresponding to the central wavelength in the range 778–788 nm. The use of molecular gases, however, can include weak 'even' harmonic emission as well. It should be mentioned that the reported XUV spectral ranges and relative intensities are based on our femtosecond NIR pulse parameters, as well as our focusing and interaction geometry in the form of a waveguide or a SIGC. In general, the waveguide and the SIGC produce similar HHG spectral profile. However, individual harmonics from a waveguide will have slightly higher photon energy, i.e. $n\omega_{\text{NIR}} + \omega_{\text{shift}}$, where the blue shift ω_{shift} is typically < 0.5 eV, as shown in Fig. 2.7(c). Thus, one can see that the origin of the blue shift comes from the fact that more plasma is generated from a SIGC geometry then that from a waveguide, which changes the phase match conditions for HHG. Besides, Fig. 2.7(c) shows that each individual harmonic from the waveguide has a broader bandwidth compared to that from a SIGC. As for the spectral intensity, SIGC usually has stronger peak intensity comparing to that in a waveguide, and this is due to the coupling losses in a waveguide based HHG. The mechanisms behind the spectral range tuning of XUV emission from various gases in a waveguide or in a SIGC can be attributed to the detailed phase matching considerations, which is beyond the scope of this paper. Detailed discussion of HHG phase-matching conditions can be found in Ref. [57, 58].

2.2.3 Even and Circularly-polarized Harmonics Generation

As discussed previously, a typical HHG only includes odd harmonics because of the symmetry that atomic and molecular gases are isotropic medium and the high harmonic bursts are produced every one-half cycle of the laser field. One has to break the symmetry of the gas medium or the sinusoidal nature of the laser field cycle in order to generate even harmonics. In Fig. 2.8(a), a simple two-color setup to break laser cycle symmetry is demonstrated. For example, the fundamental pulse has 800 nm wavelength and its second harmonic has 400 nm wavelength. The setup is intended to introduce a collinear and temporally overlapped second harmonic to break the symmetry in the HHG process. First, a thin BBO crystal is introduced to get the SHG from the fundamental harmonic. Due to the phase match condition of the eeo or the ooe condition in nonlinear optics, the field polarization of the SHG is perpendicular to the fundamental. Also, the second harmonic will have different GVD compared to that of the fundamental. Thus, a subsequent calcite plate is introduced in the setup to compensate for the GVD difference between two colors, so that there will be no group delay between them. The last component in the setup is a half wave plate ($\lambda/2$ plate) for the fundamental wavelength to rotate its field polarization by 90^o, and this wave plate also works as a full wave plate (λ plate) for the second harmonic, in which there will be no polarization change. The experimental results by implementing this setup are shown in Fig. 2.8(c) and (d) in xenon gas. Figure 2.8(c) shows a raw image on the X-ray spectrometer, where we can observe that two additional even harmonics H14 and H16 are produced. Figure 2.8(d) is the vertically integrated spectrum from the raw image. By controlling the relative intensity of the second harmonic and its time delay relative to the fundamental, we can fine tune the relative spectral intensity of even harmonics, comparing to the odd harmonics.

The HHG process we have discussed so far is for linearly polarized XUV field. Many researchers have been trying to generate circularly polarized XUV field. Direct conversion using an XUV waveplate is very challenging and expensive due to the lack

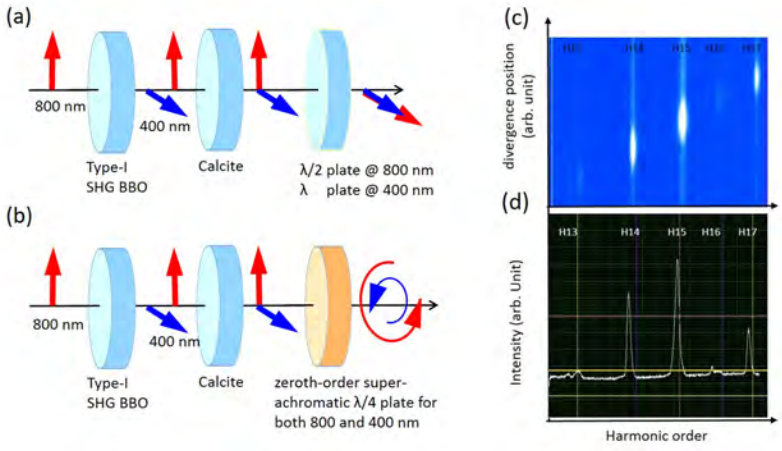

Figure 2.8: ((a) Schematic optical setup for the even harmonic generation. (b) Schematic optical setup for the circular harmonic generation. (c) An example raw image of the even harmonics from xenon HHG shown on the spectrometer. (d) An example spectrum of the even harmonics from xenon HHG, integrated from (c).)

of proper phase retardation material in XUV region. An alternative approach is to generate circularly polarized XUV pulse directly. As shown previously in Fig. 2.6(a), the third step of the three-step model is the recollision or the recombination of the liberated and accelerated electron to its parent ion driven by the laser field. One can imagine that if the driving laser field is nonlinearly polarized, there is no chance for the electron to meet its parent ion. Thus, generating circular HHG is nontrivial, if not impossible. Recently, a clever way to produced circularly polarized HHG was demonstrated in Ref. [59], which utilized two-color circular driving laser fields. By combing two laser pulses with different colors, steering electrons back to their parent ions become possible. In this novel approach, the first two optical components needed is the same as that for the even harmonic generation in order to get collinear and overlapped fundamental and its second harmonic as shown in Fig. 2.8(b). The third component needed is different–a zeroth-order super-achromatic quarter wave plate ($\lambda/4$ plate) for both fundamental and its second harmonic. With this wave-plate, the two color pulse will show counter-rotating electric fields to drive the HHG. We plan to implement this setup to implement XUV circular dichroism for material study [60].

2.2.4 Isolated Attosecond Pulse Generation

As discussed earlier, when a driving NIR pulse has multiple optical cycles, attosecond pulses will be generated. Even with a few-cycle NIR pulse, more than one or two attosecond bursts are expected. Applying optical gating techniques on a driving IR field is needed to get a single isolated pulse, so that effectively only one-half optical cycle of the driving pulse is used for the HHG process. Many approaches have been developed over past decades [61], such as the amplitude gating, the polarization gating, the angular streaking. We have implemented one of the polarization gating methods called the double optical gating (DOG) to get few-pulse APTs. Note that without actively stabilized CEP, one could either get one or two attosecond pulses depending on the CEP of that particular driving IR laser pulse. Our work to get isolated attosecond pulses is still in progress.

2.2.5 Characterization of Attosecond Pulses

We use a pump-probe based photoelectron interferometry called Reconstruction of Attosecond Beating by Interference of Two-Photon Transition (RABBIT) [62] to characterize attosecond pulses. The RABBIT was developed for measuring the average duration of the attosecond pulses in a train, which assumes that the duration of the attosecond train does not change from pulse to pulse. When an atom is ionized by XUV APTs, the discrete XUV harmonics create photoelectron wavepackets in the continuum at different discrete energies, where these wavepackets are almost exact replicas of the XUV pulses. Therefore, we can extract temporal and spectral information of XUV APTs by measuring these photoelectrons. It is shown that when electrons are ionized from atoms in the presence of the harmonics ($n\omega$, the XUV photon) and the fundamental (1ω) NIR field, the absorption, and emission of one NIR photon from the photoelectrons in the continuum can form photoelectron sidebands. The photoelectron sidebands are located at an energy between the two consecutive harmonics (for example, the 15ω and the 17ω) due to two different two-photon ionization interfering pathways such as the 15ω+1ω and 17ω-1ω. The phase

of this interference pattern can be modulated by varying the time delay between the XUV and the NIR pulse. Then the phase difference between the two harmonics can be used to reconstruct the APTs in the time-domain. In our lab, we use a Velocity Map Imaging (VMI) detector to measure photoelectrons from argon to get the RABBIT scan. Detailed descriptions of the VMI setup and our RABBIT measurement can be found in Ref. [15, 63].

2.3 The Attosecond Transient Absorption (ATA) Spectroscopy

In our pump-probe measurement, one of the split NIR pulses is used as a strong-field pumping/perturbing/controlling pulse with intensity, field polarization, and the wavelength controlled by combining waveplates, polarizers, and an OPA setup. The pumping NIR pulse is delayed by two delay stages in line. One stage has ∼2 femtoseconds (∼100 μm/step) delay precision driven by a stepper motor (Melles Griot), and the other stage has ∼6.6 attoseconds (∼1 nm/step) delay precision driven by a digital piezo translator (DPT) (DPT-C-S, Queensgate Instruments). Thus, 40 DPT steps correspond to ∼1 optical cycle (o.c.) of 780 nm wavelength pulse. Note that the backlash of the stepper motor could lead to ∼13 fs shift. The maximal peak intensity of this pumping NIR is few TW/cm^2 at the transient absorption gas cell.

We use a home-made XUV spectrometer in all experiments, which includes a concave ruled reflective grating and a back-illuminated thermoelectric-cooled X-ray CCD camera (PIXIS-XO 400B, Princeton Instruments). Two different gratings can be used, namely, (i) Richardson Gratings 52025BK02-691D , 1200 grooves/mm, 1 m radius of curvature, gold coated, blaze angle of 1.5^o, and (ii) Richardson Gratings 52020BK02-762D, 1200 grooves/mm, 1 m radius of curvature, gold coated, blaze angle of 2.3^o. A 200 nm thick aluminum foil filter (Lebow Co.) is mounted in front of the camera to filter out the NIR. The spectrometer detects transmitted XUV spectra with a resolution of ∼10 meV at 24 eV. This resolution is measured based on a typical helium transient absorption data. As our spectrometer cannot

resolve the narrow NIR-free absorption lines at window resonance for target gases such as helium, the transmitted XUV spectrum, I_{out}^{XUV}, in the absence of NIR field, is essentially the same as the input XUV spectrum, I_{in}^{XUV}. Therefore, we can use it as a reference for evaluating measured OD in our experiments.

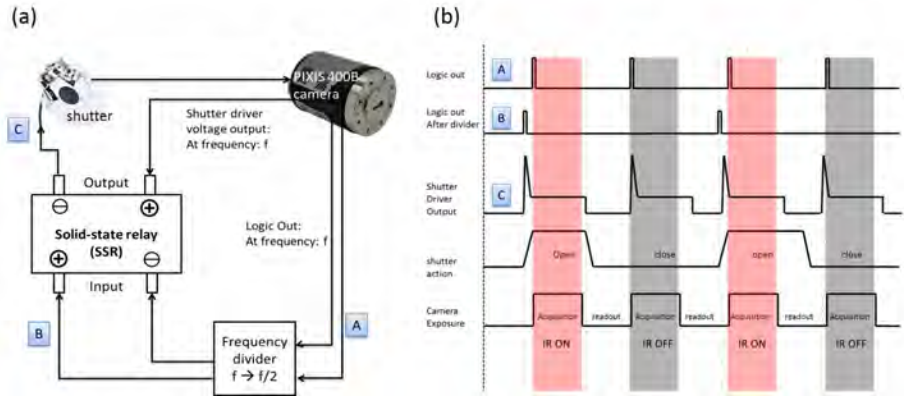

Figure 2.9: (a) A schematic for the shutter setup. (b) A schematic of the timing diagram for the shutter control and the camera frame acquisition.

We also use a shutter (Uniblitz VS25, Vincent Associates) on the NIR pumping beamline to get near-instantaneous background (i.e., NIR free) XUV spectra I_{out}^{XUV} at each camera exposure. In the following, we briefly describe how to implement the frame acquisition with subsequent shutter-on and shutter-off scheme.

First, A logic-out signal at acquisition frequency f (such as 10 Hz, exposure time 0.1 s) from the X-ray camera is sent to a frequency divider and to generate a $f/2$ TTL signal. Then, this $f/2$ signal is fed into a solid-state relay. The output of the solid-state relay is connected to a shutter and a built-in shutter driver in the X-ray camera. Figure 2.9 illustrates the shutter setup and its timing control. A typical experimental OD is obtained by calculating consecutively measured XUV spectrum with the NIR, and without the NIR for 0.1–0.5 s exposure time per CCD frame. We then average 40-400 frames at each delay step. Thus, an individual spectrum represents an average of 4,000-200,000 laser shots at each delay step. In this dissertation, we use the convention that the XUV pulses proceed the IR pulse is called negative time delay.

CHAPTER 3

The Helium Experiments

3.1 Part I: Beyond the Single-atom Response in Absorption Lineshapes: Probing a Dense, Laser-dressed Helium Gas with Attosecond Pulse Trains

(This section is adapted from C.-T. Liao *et al.*, "Beyond the single-atom response in absorption lineshapes: Probing a dense, laser-dressed helium gas with attosecond pulse trains.", *Physical Review Letter* **114.14**, 143002 (2015), as in Ref. [64])

3.1.1 Introduction

The development of attosecond (10^{-18} sec) XUV spectroscopy [65] has opened new possibilities for application of transient absorption in real-time measurement and control of physical, chemical and biological processes at the natural timescale of electron motion [50, 66]. In particular, recent studies of attosecond transient absorption (ATA) in helium atoms have focused on how the presence of a moderately strong IR pulse alters the XUV absorption process at the single-atom level, for instance via the AC Stark-shifts [67], or the appearance of new light-induced states [68]. The ability of the IR field to alter the shape of the absorption profile from symmetric to dispersive or vice versa through a phase shift of the XUV-initiated time-dependent dipole moment has also been demonstrated [69–73].

Most ATA experiments to date have assumed that the measured macroscopic optical density is directly proportional to the single-atom absorption cross section $\sigma(\omega)$ [67, 68, 70, 74, 75]. This implicitly assumes Beer's law for dilute-gas absorption, $I_{out}(\omega) = I_{in}(\omega)\mathrm{e}^{-\rho\sigma(\omega)z}$, where ρ is the atomic density and z is the propagation distance, even though many of these measurements were performed at relatively large optical densities, necessitated by the weak XUV sources. Only one experiment (with theory) has explicitly addressed propagation effects [76], in addition to a number of

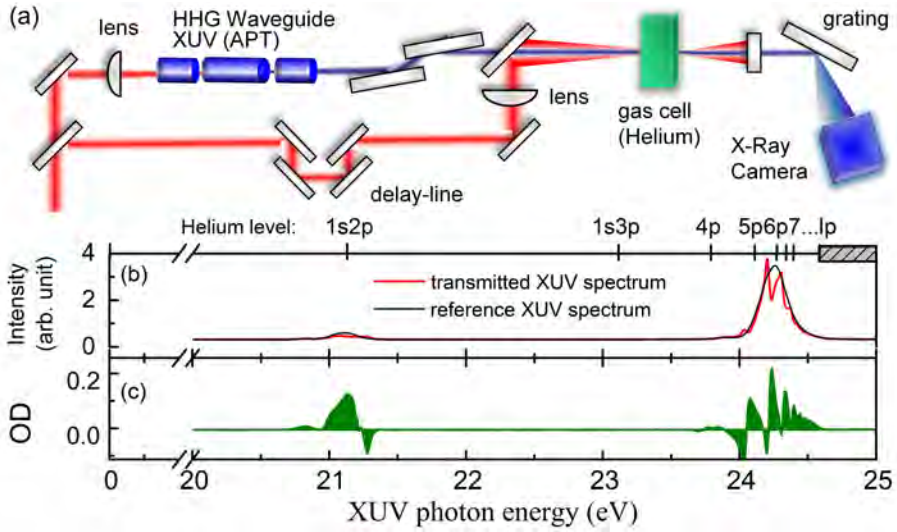

Figure 3.1: (a) The experimental setup for ATA spectroscopy. (b) Typical XUV transmittance spectra with (red) and without (black) the IR field with Helium states labeled. (c) The optical density retrieved from (b).

calculations [71, 77–79]. As attosecond science moves to more complex systems such as liquids, solids, and bio-materials which generally have higher densities [80–82], it becomes imperative to understand macroscopic effects beyond Beer's law, and in particular how they can be disentangled from laser modification effects in ATA.

In this work, we extended ATA spectroscopy to the more general case where collective effects enter into both experimental and theoretical considerations, by investigating the transient absorption of an attosecond pulse train (APT) in an optically thick helium sample interacting with a moderately strong IR pulse. We considered the interplay between two different processes that can reshape the absorption line - the IR-induced phase shift of the time-dependent dipole moment [70–73] and the macroscopic resonant propagation of the XUV pulse [83]. We showed that initially, the two processes act independently so that the main effect of propagation is to broaden the characteristic line shape controlled by the IR perturbation (IRP). At higher pressures or longer propagation lengths, we observe new spectral features near the line center. We establish the origin of these features in terms of the propagation-induced temporal reshaping of the short XUV pulse due to narrow-band resonances

in He gas. The temporal reshaping is a collective effect which has been observed and utilized in a range of applications from nuclear spectroscopy to quantum-well exciton studies and is often referred to as resonant pulse propagation (RPP) [83]. In this work, we explicitly observe its effects in ATA for the first time and show how the interplay between the single-atom IRP and the collective RPP effects manifests itself in the absorption profile.

3.1.2 Experimental setup

Our experiment (Fig.3.1(a)) utilizes Ti:Sapphire laser amplifier to produce 40 fs IR pulses at 1 kHz repetition rate with pulse energy 2 mJ, central wavelength 786 nm, and full width at half maximum (FWHM) bandwidth 26 nm. The XUV APT with ∼440 attosecond bursts and ∼4 fs pulse envelope is obtained by high harmonic generation in a Xenon filled waveguide. The APT is dominated by harmonics 13, 15, and 17. The XUV and IR pulses are combined using a mirror with a hole and focused into a 10 mm long He gas cell with a backing pressure of a few Torr, covered by Aluminum foil. The IR laser drills through the foil, allowing both XUV and IR beams to propagate. A spectrometer detects the transmitted XUV spectrum with a resolution of ∼7 meV at 24 eV.

Typical XUV transmission spectrum (Fig.3.1(b)) measured at 8 torr backing pressure, with (black curve) or without (red curve) an IR pulse of 3 TW/cm^2 peak intensity. The XUV-IR delay is $\tau = +25$ fs, meaning XUV arrives after the IR. We average more than 10,000 laser shots with fluctuating carrier-envelope phase, so the observed absorption lineshapes represent an average over the sub-cycle delay variation. As our spectrometer cannot resolve the narrow field-free absorption lines, the transmitted XUV spectrum I_0 in the absence of IR field is essentially the same as the input XUV spectrum. We therefore use it as a reference for evaluating the optical density, $OD(\omega, \tau) = -\log_{10}(I(\omega, \tau)/I_0)$, where $I(\omega, \tau)$ is the transmitted XUV spectrum in the presence of the IR [74]. The spectral lineshape is strongly modified in presence of IR field, and both absorption ($OD > 0$) and emission ($OD < 0$) features are observed (Fig.3.1(c)). Moreover, the lineshapes are no longer simple

Lorentzian-like peaks, but also include dispersive Fano-like profiles [84].

3.1.3 Simulation method overview

Our theoretical framework for ATA in laser-dressed He is described in [77]. Briefly, we numerically solve the coupled time-dependent Schrödinger equation (TDSE), in the single active electron approximation, and the Maxwell wave equation (MWE). This yields the space- and time-dependence of the full IR- and XUV-electric field at the end of the gas. The optical density is then $OD(\omega) = -\log_{10}[I_{out}(\omega)/I_{in}(\omega)]$, where $I(\omega)$ is the radially integrated yield. We use an APT synthesized from harmonics 13 through 17, with initial relative strengths of 1:6:10 and all initially in phase. The FWHM duration of the APT is ∼5 fs, and the peak intensity is 10^{10} W/cm^2. The IR pulse has a central wavelength of 770 nm, a FWHM duration of 33 fs, and a peak intensity 2 TW/cm^2. For computational reasons, we consider a cell of length 1 mm and choose the range of pressures so that the evolution with pressure is similar to that of the experiment. A decay time of ∼60 fs is imposed on the time-dependent polarization, to match the observed absorption line widths at low density, in the presence of the IR [68].

Fig. 3.2(a) shows the measured OD around the He 1s2p line for different backing pressures , when the XUV-IR delay is approximately zero. Unlike ATA spectra in dilute gas (black curve) that exhibit a Fano-like profile with a broad peak and valley, we observe a complicated lineshape with finer absorption and emission features (colored curves). The lineshape strongly depends on the density of our thick sample, or more precisely, the pressure-length product in the gas cell. We observe broadening of the outer features of the lineshape, with the absorption peak on the left and the emission valley on the right both moving outward from the center as the pressure increases. In addition, we observe new sharp absorption features that appear on line center and move outward.

Fig.3.2(b) shows the OD calculated within the TDSE-MWE framework which in general agrees well with the experimental results.The energy axis of the theory curves has been shifted by about 0.1 eV to account for the small off-set of the

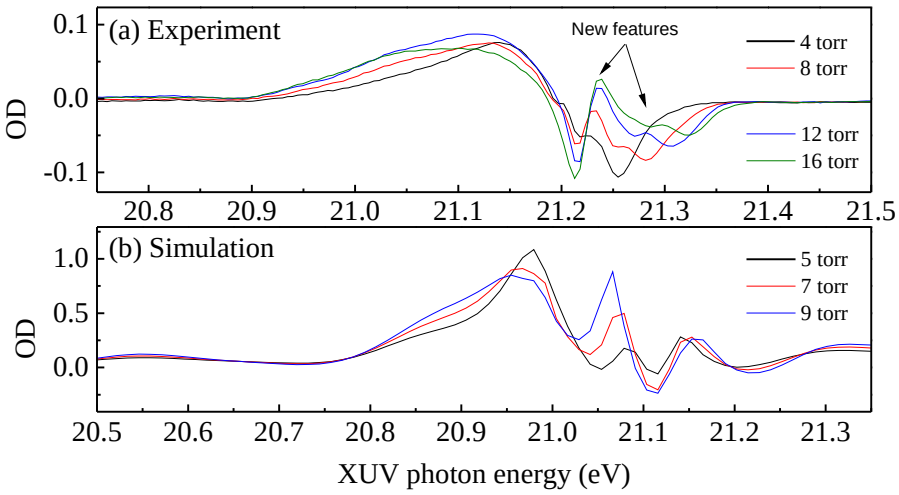

Figure 3.2: Experimental (a) and theoretical (b) OD spectra around the He 1s2p state, in the presence of the IR field, and at different backing pressures. Arrows indicate new sharp spectral features.

1s2p energy predicted by the pseudo-potential used in the TDSE calculations. To mimic the experimental delay resolution and carrier-envelope phase instability, the calculations have been averaged over a half IR cycle of delays around zero.

Fig.3.3(a) and (b) show measured and calculated lineshapes of higher lying 1snp states, where $n = 4, 5, 6, ...$ Unlike the 1s2p state, these np lines show better defined Fano-like profiles, and the changes with pressure are less dramatic. Similar to the 1s2p line, the lineshapes are broadened, and both absorption and emission features are enhanced and move outward from the center of each resonance as the pressure increases. However, in contrast to the 1s2p line, we do not observe new sharp features.

3.1.4 Model calculation and simulation results

In the following, we will show that the spectral reshaping of the IR-controlled absorption profile originates in the RPP-induced temporal reshaping of the XUV pulse. To this end, we have performed a series of simpler TDSE-MWE calculations in which the TDSE is solved for a two-level system interacting with a resonant light field. We use an isolated 400 attosecond pulse centered on 21.1 eV, and we impose a ∼110 fs

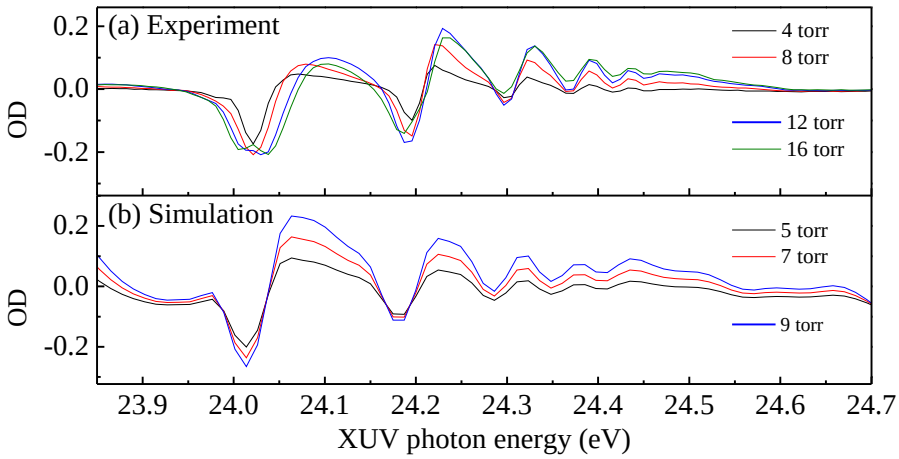

Figure 3.3: Experimental (a) and theoretical (b) OD around the He 1snp states in the presence of IR.

decay time on the time-dependent polarization. The effect of the IR pulse is modeled as a time-dependent phase that accumulates on the upper state amplitude, proportional to the IR intensity, as if the laser-imposed phase was strictly proportional to the Stark shift [71]. The IRP and the attosecond pulse begin at the same time. The IRP magnitude and the atomic density are chosen to match the experimentally observed line shape.

Fig.3.4(a-c) shows the evolution of the OD with propagation distance in a 1 mm medium with a density of 3×10^{16} cm^{-3}, perturbed by a short, 2.7 fs, IR pulse. In the first half of the medium, the main effect of propagation is a linear broadening and increase of the initial dispersive-like line shape. In the second half of the medium, in addition to the broadening, we see the formation of a new sub-structure on line-center (21.1 eV). Further propagation (or higher density, thin blue line in Fig.3.4(b)) leads to additional broadening and the formation of a new substructure via splitting and separating of the first sub-structure into two.

Fig.3.5(a) shows how the XUV pulse is temporally reshaped by RPP and develops a weak tail with longer and longer sub-pulses in it. As first discussed by Crisp [85], the number of these sub-pulses increases and their duration decreases with propagation, as seen from the comparison of the low and high density cases. In the

time domain, this RPP-induced reshaping can be understood as the consequence of the long tail of the electric field generated by the resonantly excited time-dependent dipole moment, the duration of which is determined by the effective lifetime of the upper level. This newly generated, long-lasting, electric field is out of phase with the driving, short-pulse, electric field, which leads to destructive interference (absorption) for a narrow range of frequencies. As the long tail of the electric field propagates through the medium, it in turn will excite new time-dependent dipole moments which will give rise to electric fields out of phase with that of the original tail (eventually giving rise to a new sub-pulse), and the process repeats. We note that this reshaping happens independently of the IR dressing field. The results in Fig.3.5(a) were calculated in the absence of the IR, and are almost identical to the case when the IR is included. On the other hand, in the absence of reshaping, the IRP imposes a phase shift which builds up while the IR pulse is on, and then remains with the time-dependent dipole moment. The newly generated electric field will then no longer be exactly out of phase with the driving electric field. This manifests itself in the absorption spectrum as a more complex line shape in which some frequencies are absorbed and some are emitted, for instance as in Fig.3.4(a), and where the line width is determined by the lifetime [70–72].

Combining our understanding of the RPP and the IRP, we see that the primary effect of the RPP-induced reshaping is a shortening of the effective lifetime during which the IR-perturbed dipole moment oscillates, corresponding to the duration of the first sub-pulse in the XUV time profile [83]. This is because the phase of the electric field changes sign in the subsequent sub-pulse, thereby oscillating out of phase with the field that generated it which leads to renewed absorption and effectively ends the phase influence of the IRP. The RPP-shortened effective lifetime of the IRP causes the broadening of the IR-perturbed line shape. The new, narrow, absorption features are caused by the subsequent, longer, sub-pulse, and they do not (at first) alter the main IRP line shape.

This explanation suggests that the IR-controlled change in the absorption profile remains a characteristic of the IRP as discussed in [70, 72] as long as the effective,

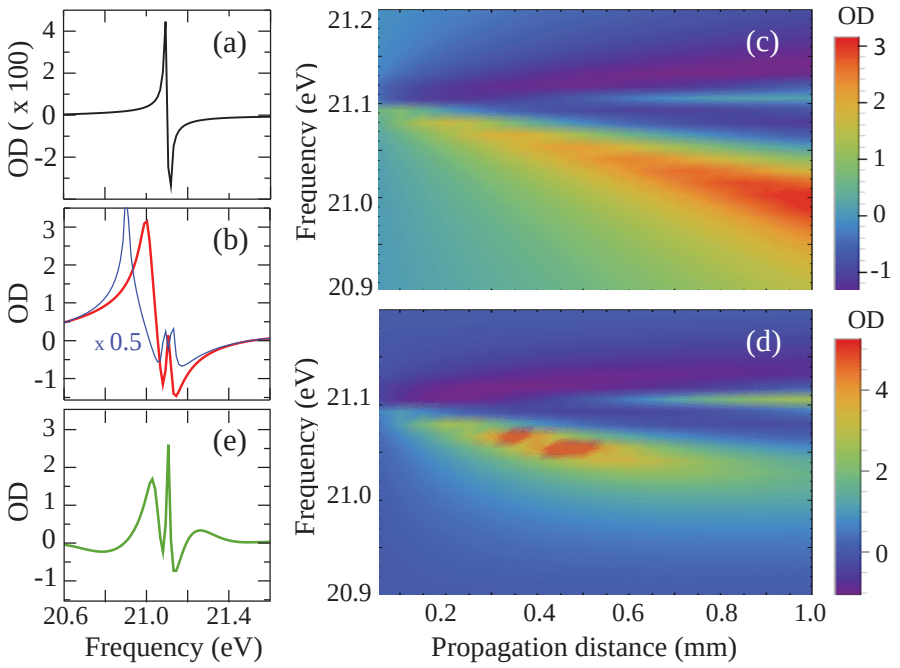

Figure 3.4: Two-level TDSE-MWE calculations of OD. (a) and (b) show the initial (thick black line) and final (thick red line) OD for a 1 mm long medium with density $\rho = 3 \times 10^{16}$ cm^{-3}, perturbed by a 2.7 fs IR pulse. Final OD for $\rho = 6 \times 10^{16}$ cm^{-3} is also shown (thin blue line). (c) OD evolution with propagation distance, OD(z), for $\rho = 3 \times 10^{16}$ cm^{-3} case in (a) and (b). (d) OD(z) for $\rho = 3 \times 10^{16}$ cm^{-3} and a longer IRP (13 fs); the final OD for this is shown in (e).

RPP-controlled, lifetime is much longer than the IR pulse. However, when the two time scales become comparable, this simple picture breaks down and the time-dependent dipole moment will exhibit a more complicated amplitude and phase dependence. This is demonstrated in Fig.3.4(d) which shows OD(z) in the lower-density case where the IR pulse duration $\tau_{IR} = 13$ fs, which is close to the $1/e$ duration of the first sub-pulse, $T_{1/e}$, in the reshaped time-profile in Fig.3.5(a) (thick red line). After ≈ 0.4 mm of propagation (when $\tau_{IR} \approx 2T_{1/e}$), the linear increase of both the spectral width and the maximum and minimum values of the OD breaks down, and the narrow feature on line center strongly increases. This results in a final line shape (Fig.3.4(e)) which is both narrower than what RPP-reshaping would predict, and very different from the initial line shape, with a strong central feature

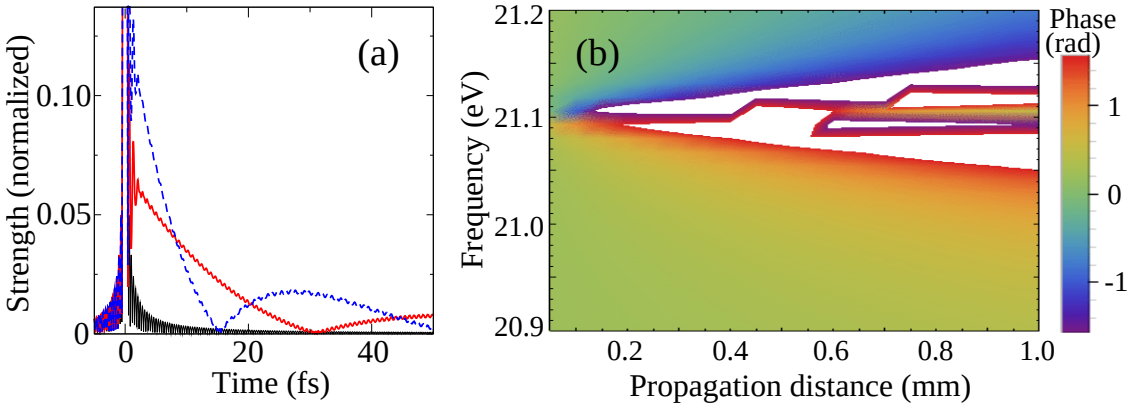

Figure 3.5: Two-level TDSE-MWE results in the absence of IRP: (a) Normalized XUV electric field time structure at the beginning (thin black line) and end of the medium with $\rho = 3 \times 10^{16}$ cm^{-3} (thick red line), and $\rho = 6 \times 10^{16}$ cm^{-3} (dashed blue line). (b) The spectral phase accumulation vs. z. The white area marks where the spectral phase is larger than $\pi/2$ or smaller than $-\pi/2$.

and several extra features in the wings.

We observe similar effects for the 2.7 fs IR pulse for higher pressures, when the first sub-pulse becomes comparable to the IR pulse. In such cases, the relationship between the IRP and the absorption line shape is no longer simple, but depends explicitly on a self-consistent process in which the reshaped pulse and the IRP both play a role. In the experiment, this limit has been reached for the 1s2p absorption line shape at the highest pressures shown in Fig. 2, where the broadening saturates and the strength of the narrow, central, feature dominates.

On the contrary, the line shape around the 1snp resonances in Fig. 3 is predominantly broadened because the single atom response is weaker for these transitions, and the temporal reshaping of the XUV pulse is less severe.

Finally, we briefly present a frequency domain picture of the RPP-induced temporal reshaping. Fig.3.5(b) shows the z-dependence of the XUV spectral phase accumulated due to dispersion. In the absence of the IRP, the spectral bandwidth over which significant phase is accumulated increases linearly. In the frequency domain, a phase change of more than π will lead to a sign-change and thereby the formation of a new sub-pulse in the time domain. The temporal reshaping can thus

equally well be thought of as being driven by dispersion in the frequency domain. In the absence of the IR, this broadening is primarily present in the spectral phase, but when the IR is present it also manifests itself as broadening of the absorption line width itself. A similar effect was observed in the strong-field limit in the absorption profile of a broadband pulse that was intense enough to induce Rabi cycling between the resonant levels [86].

The combined time- and frequency picture offers a guideline for when macroscopic effects cannot be ignored when interpreting an ATA line shape: when $T_{1/e}$ of the first sub-pulse becomes comparable to (approximately twice as long as) τ_{IR}. The former can be estimated from the bandwidth $\Delta\omega$ over which the accumulated spectral phase $\phi(\omega, z) = \chi'(\omega)\omega/cz$ is larger (or smaller) than $\pm\pi/2$, as $T_{1/e} \approx \frac{2}{\pi\Delta\omega}$, where $\chi'(\omega)$ is the (IR- and spectrometer-broadened) susceptibility. Under this criterion, the spectral phase on line center can still accumulate many factors of π. Therefore, this guideline on bandwidth is much less restrictive on the experimental density than considering the first time the spectral phase $\chi'(\omega)\omega/cz$ equals π which usually happens within tens of microns of propagation at typical ATA densities [76].

3.1.5 Summary

In summary, we have studied ATA in laser-dressed He, in the limit where the gas medium is optically dense so that macroscopic effects influence the absorption line shapes. In both experiment and calculations we clearly observe the characteristic spectral signatures of temporal reshaping of the XUV pulse as it propagates through the resonant medium: the broadening of the bound state resonance profile as well as the emergence of new, narrow features at the resonance energy. These results represent a novel manifestation of the general phenomenon of resonant pulse propagation [83], in our case in the weak attosecond pulse regime, in which a moderately strong IR pulse facilitates the spectral measurement of an effect which is otherwise only apparent in the time-domain. The new regime of RPP can be applied for tailoring high frequency light fields [87], thereby controlling light matter interaction on extremely fast timescales. Finally, we use our frequency-domain interpretation

of this phenomenon to propose a guideline for when macroscopic effects cannot be ignored in an ATA experiment: when the time scale of the first sub-pulse in the reshaped XUV field is comparable to the duration of the IR perturbation. This will be useful in a range of transient absorption experiments in which one aims to learn about the dynamics of a quantum system from the shape of the absorption profile, for instance under the influence of an IR pulse [88], but where experimental conditions necessitate using a relatively dense medium.

3.2 Part II: Exploring the Interplay between Resonant Pulse Propagation and Laser-Induced Line Shape Control: A Systematic Study

(This section is adapted from C.-T. Liao *et al.*, "Attosecond transient absorption in dense gases: Exploring the interplay between resonant pulse propagation and laser-induced line-shape control.", *Physical Review A* **93**, 033405 (2016), as in Ref. [89].)

3.2.1 Introduction

Important experimental and theoretical advances have been made in the field of transient absorption spectroscopy in the past few years due to the application of novel attosecond (10^{-18} sec) extreme ultraviolet (XUV) light sources [90]. Since 1990's, conventional femtosecond transient absorption spectroscopy has been routinely applied as a powerful tool to study phenomena ranging from basic photophysical and photochemical processes to the workings of biological complexes responsible for vision [91], light-harvesting [92] *etc.* Attosecond light sources, either in the form of attosecond pulse trains (APT) or isolated attosecond pulses [74, 93], have led to a major improvement in the temporal resolution of transient absorption spectroscopy, opening the pathway for direct observation of electron dynamics on their natural timescales. The attosecond approach offers immense potential for the study of complex electronic processes, *e.g.* correlation driven charge migration, which occur on attosecond to few-femtosecond timescale [94].

Several recent attosecond transient absorption (ATA) experiments have demon-

strated the observation and manipulation of electron wavepacket dynamics in dilute atomic gases, such as krypton [50, 95], argon [66], neon [96], helium [67, 97, 98], dilute molecular gases such as bromine [99], and solid-state thin films such as silica [80], cobalt oxide [100], etc. These efforts have resulted in better understanding of many fundamental physical phenomena including valence electron motion, autoionization, transient electric conduction, light-induced virtual states [101], gain/loss mechanisms [102], and lineshape modification [66, 72, 103, 104].

In the majority of ATA experiments and calculations on gaseous samples, however, the temporal and spectral properties have been studied assuming a single-atom response, i.e., the dilute gas assumption in which absorption follows the Beer-Lambert law. Few attempts have been made to observe [64, 105] or calculate [77, 79, 105–109] ultrafast transient absorption in dense media, where the collective interaction effects and nonlinear response of the electric dipoles or atomic polarizations are important. Recently, we found experimentally and theoretically that when a dense medium is investigated with ATA, the macroscopic XUV pulse propagation effect cannot be ignored, and the complicated coupling between XUV field and atomic polarizations must be taken into account [64]. In particular, we observed clear signatures of resonant pulse propagation (RPP) effects in the XUV absorption spectra [64].

RPP was first discussed in the 1970s [110, 111] and describes a very general phenomenon in which a short pulse propagating through a medium with long-lived resonances will undergo strong temporal reshaping. Detailed analysis of the effects of RPP is available for the propagation of visible and near-infrared (IR) femtosecond and picosecond pulses [112, 113], and more generally RPP has been observed and utilized in a range of applications from nuclear magnetic resonance to quantum-well exciton studies [83]. More recently, it has been discussed in the context of propagation of zero-area, single-photon pulses [114]. The temporal reshaping caused by RPP is illustrated in Fig. 3.6 for an XUV pulse with a duration $\tau_{xuv} = 5$ fs propagating through an 16 Torr helium gas in which it is resonant with a transition with a decay time $\gamma = 60$ fs. The figure illustrates how the short pulse initially

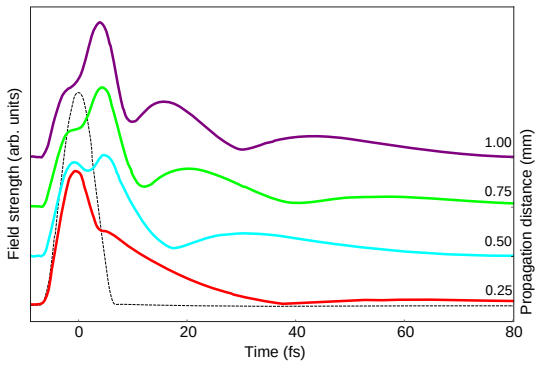

Figure 3.6: Illustration of resonant pulse propagation of a 5 fs XUV pulse propagating through a 16 Torr helium gas in which the XUV light excites a resonance with a 60 fs decay time. We show the XUV electric field strength at different propagation distances up to 1 mm, with the initial pulse shown as the dotted line. The XUV pulse quickly develops a long tail consisting of a series of sub-pulses which shorten with propagation.

builds up a long tail which then subsequently develops into a series of sub-pulses. Each sub-pulse is longer in duration and weaker than the previous sub-pulse, and in each sub-pulse the electric field changes its phase by π relative to the previous sub-pulse (not shown). The RPP effect is driven by the large spectral phase which can be accumulated due to dispersion (each accumulated phase of π in the spectral domain leads to a sign change of the electric field in the time domain) and leads to reduced absorption compared to Beer-Lambert's law [110]. In the limit of very long lifetime ($\gamma >> \tau_{xuv}$), the electric field envelope as a function of propagation distance z, pressure P, and time t will be proportional to the first order Bessel function [112]:

$$\mathcal{E}(z,t) \propto \frac{J_1(\sqrt{a\sigma_0\gamma Pzt})}{\sqrt{t}}, \tag{3.1}$$

where σ_0 is the absorption cross section on line center and a is a proportionality constant. For a given system the magnitude of the reshaping and the duration of the sub-pulses are thus determined by the pressure-length product Pz, and are strongly influenced by the oscillator strength and lifetime of the transition.

This work is intended as a systematic experimental and theoretical investigation of the XUV spectral line shapes associated with ATA in a dense helium gas sample

that has been laser-dressed by a moderately strong infrared (IR) field of varying intensity and polarization, over a range of time-delays and gas pressures. We are in particular interested in exploring how the interplay between the microscopic IR-laser-dressing and the macroscopic RPP reshaping affects the transient absorption of the attosecond XUV pulse. The RPP effect in our experiment leads to the temporal reshaping of the probing XUV, while the IR perturbation facilitates the spectral measurement of this effect because of its role as a time-dependent phase-shift of XUV induced dipole polarization. Apart from exploring a new temporal and spectral regime, our work, unlike earlier RPP studies, employs a two-color IR-pump XUV-probe configuration. Our results elucidate the complex interplay between the XUV and IR pulses, enabled by the nonlinear medium, in both time and frequency domain descriptions. We find that the propagation-induced XUV reshaping influences conclusions and interpretations one can draw from IR-induced spectral line shapes as a function of XUV-IR delay, IR intensity, IR polarization and gas sample density. Reversely, we also find that the IR pulse influences the RPP induced temporal reshaping, especially when the IR pulse is long. We believe that incorporating such macroscopic propagation effects will become more and more important as pump-probe ATA spectroscopy moves towards investigations of complex systems, e.g., dense plasmas, condensed phase systems, and biological samples.

The section is organized as follows: In Subsection 3.2.2 we discuss the ATA spectral line shape in a dense laser-dressed helium gas as it evolves with respect to the relative XUV-IR delay and give a general introduction to the interplay between RPP and the laser-dressing effects. Subsections 3.2.3, 3.2.4 and 3.2.5 present experimental and theoretical studies of the line shape dependence on the IR intensity, the gas pressure, and the relative XUV-IR polarization, respectively. We end the work with a brief conclusion in Subsection 3.2.6.

3.2.2 Spectral lineshape evolution

We start by investigating the evolution of the OD with respect to the relative delay. Fig. 3.7(a) and 3.7(b) show the transmitted (blue curves) and reference (purple

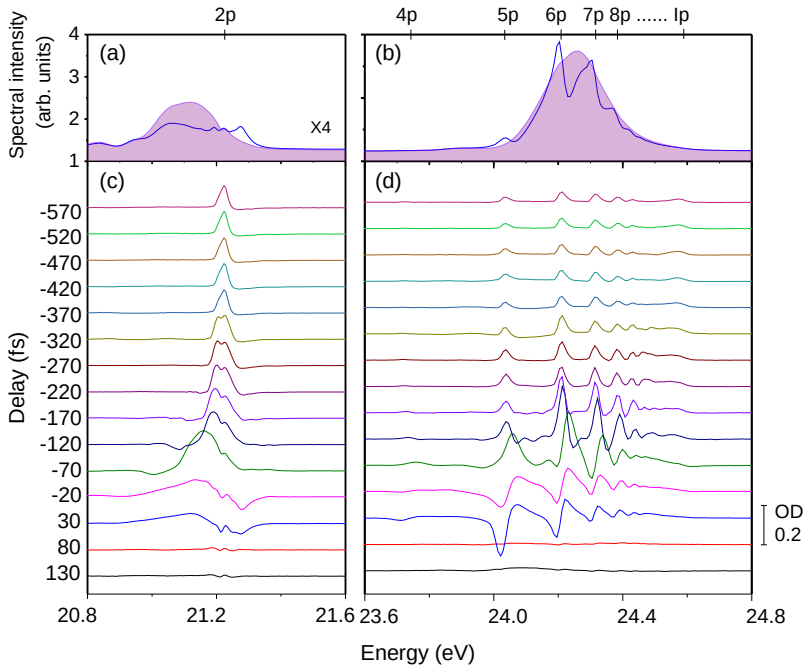

Figure 3.7: Experimentally measured spectral lineshape evolution as a function of delay. (a) and (b) shows transmitted (blue curves) and reference (purple shaded area) XUV spectra around H13 and H15, respectively. (a) is scaled up by a factor of 4 in comparison to (b) for a better view. (c) and (d) show the evolution of the OD as a function of XUV-IR delay. The scale bar on the right represents signal magnitude corresponding to $OD = 0.2$.

shaded area) XUV spectra of H13 and H15 at $\tau \sim 0$. The helium backing pressure is 8 torr and the IR intensity used is $\sim$3 TW/cm^2. The relevant He field-free energy levels, e.g. $1s2p$, $1s4p$, $1s5p$, ..., and up to the ionization potential (I_p), are labeled at the top of the figure.

The transmitted spectra illustrate that at some XUV photon energies, the spectral intensity is larger than the reference spectra. Unlike traditional static absorption spectra, the presence of the external IR field modifies the time-dependent dipole moment which has been initiated by the XUV field, predominantly by the addition of a time-dependent phase due to the AC Stark shift of the excited state [66, 103, 107]. In the spectral domain, this leads to a redistribution of energy between the light field and the atom and generally gives rise to transient absorption profiles that include

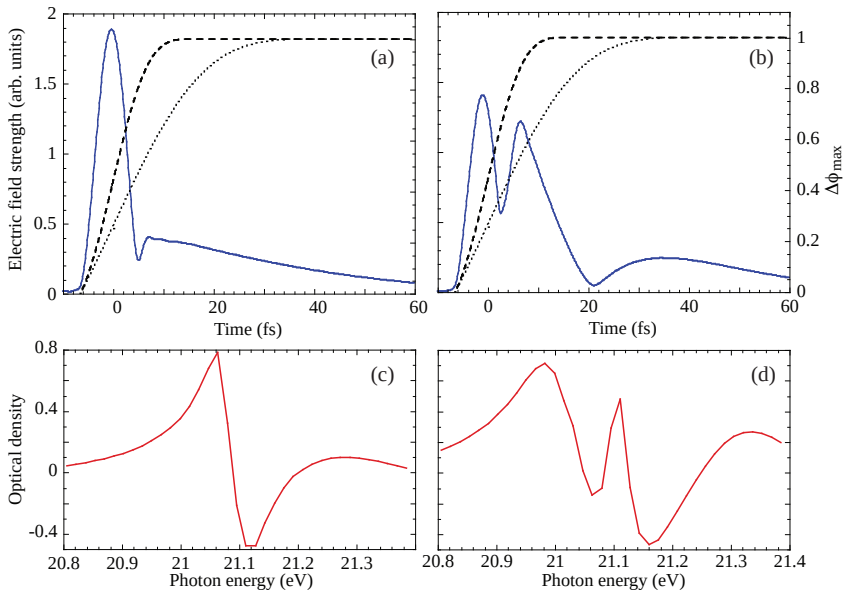

Figure 3.8: (a,b) Calculated XUV time profiles at two different propagation distances $z = 0.25$ mm (a) and $z = 1$ mm (b) in an 8 Torr helium gas, dressed by a 2.25 TW/cm^2 IR pulse, with their corresponding optical density spectra shown above. In (a) one long sub-pulse is visible in addition to the initial pulse centered on $t = 0$, and in (b) two sub-pulses are visible. The figure also shows an approximate time-dependence of the phase shift imposed by two different IR pulses of duration 13 fs (thin dashed lines) and 33 fs (thin dotted line).(c,d) Spectral lineshape (OD) obtained in the presence of IR pulse for the two propagation distances of 0.25 mm (c) and 1mm (d).

both positive and negative values, corresponding to absorption (loss) or emission (gain) at different frequencies. In the simplest possible case in which one starts with a purely Lorentzian absorption line shape around a bound state resonance and then adds an instantaneous phase shift due to a short IR pulse, the resulting absorption line shape can be varied smoothly between a Lorentzian, a dispersive (Fano, [84]), and a window resonance line shape depending on the magnitude of the laser induced phase (LIP) shift. This was discussed extensively in [103] and other papers.

Fig. 3.7(c) and (d) show the OD spectral lineshape evolution as the delay changes. For large positive delays, $\tau > 70$ fs, all of the IR pulse arrives before the XUV pulse and the OD is flat ~ 0 which means that there is no change in the absorption relative to the reference spectrum. Since the IR pulse is too weak to excite

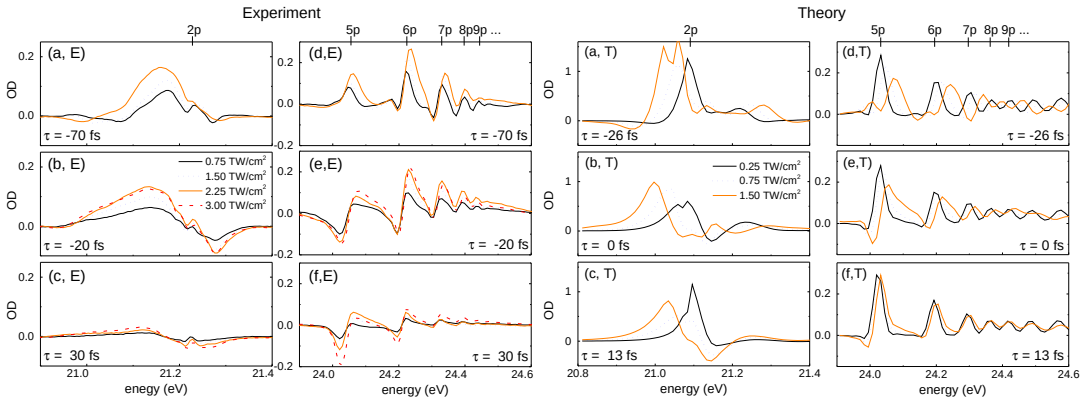

Figure 3.9: (a,E) - (f,E): Experimentally measured IR intensity dependent OD spectra around the $1s2p$ (first column) and $1snp$ (second column) lines at some representative delays. (a,T) - (f,T): Calculated OD spectra at some comparable delays. Note that RPP induced peaks are only visible in the $1s2p$ state.

the helium atoms in the absence of the XUV field, at these delays the only absorption is due to the unperturbed bound states which cannot be resolved by our spectrometer due to their long lifetimes. In contrast, at large negative delay, e.g., $\tau <$ -370 fs, when the XUV comes first, we observe traditional near-Lorentzian (Voigt) line shapes in the OD spectra. The Voigt profile results from the convolution of two broadening mechanisms manifesting as Lorentzian and Gaussian, where the Gaussian part is due to Doppler broadening, pressure broadening, and the profile of the IR pulse. The Voigt lineshapes at large negative delays are due to the perturbed free induction decay of the excited populations in $1s2p$ or higher lying $1snp$ states. Upon the arrival of the XUV pulse, H13 and H15 coherently prepare two atomic polarizations corresponding to the $1s2p$ and $1snp$ states. These atomic polarizations freely evolve till the IR arrives at some time later, and perturbs the typical free induction decay process. Compared to the natural lifetime of the $1snp$ states (∼nanosecond range), the femtosecond IR perturbation acts like an impulsive kick, giving rise to a Voigt lineshape whose width is primarily a characteristic of the IR pulse duration. We find that this constant width Voigt lineshape persists in the OD even for very large negative delays (more than a few ps, not shown) in our experiments.

At delays close to zero, complicated line shapes can be observed in the OD spectra. In the intensity regime shown in the figure, the overall line is shifted to lower energy and the shape is Fano-like, although more complex, with several sub-features close to line-center and additional features in the wings of the profile. The downward Stark shift is caused by the laser-induced interaction with higher-lying excited states (see for instance [8, 107]). The overall dispersive-like shape is due to the laser-induced phase (LIP) discussed above. The features in the wings of the profile result from the relatively long duration of the IR pulse, as the LIP perturbation is imposed not instantaneously but over a finite time. Finally, the narrow features close to the field-free $1s2p$ energy are due to RPP [110, 111] as we discussed in [64]. In the following, we will illustrate the interplay between the RPP XUV temporal reshaping and the effect of the IR pulse in further detail.

This interplay is illustrated in Fig. 3.8 which shows calculated time profiles of the XUV electric field strength and the corresponding optical densities at two different propagation distances in an 8 Torr He gas. The IR pulse is short, with a FWHM pulse duration of 13 fs and a peak intensity of 2.25 TW/cm^2. Since the biggest dipole response is from the $1s2p$ transition which is excited by H13, we show time profiles corresponding to the H13 part of the APT. Since the RPP effect is driven by the spectral phase accumulated via dispersion by the propagating, resonant XUV pulse it is to first order independent of the IR pulse, and similarly to Fig. 1 one can observe the build-up of the long tail in the XUV time profile and the formation of multiple sub-pulses as the pulse propagates [1]. We note that the duration of the first sub-pulse acts as a new effective lifetime for the resonant interaction. The shortening of the first sub-pulse during RPP therefore in general leads to broadening of the absorption profile, resulting in a width proportional to the optical thickness Pz [83].

[1] The depth of the first minimum, between the main pulse and the first sub-pulse is influenced by the IR and for instance depends on the sub-cycle delay. This short-time modulation is due to the excitation of light-induced states in the vicinity of the $1s2p$ state which are within the bandwidth of the XUV pulse and which can be excited while the IR field is on, see for instance [101].

Fig. 3.8 also illustrates the effect of the IR pulse by showing an approximation to the LIP of the time-dependent dipole moment, assuming that the phase accumulates proportionally to the IR intensity. When the IR pulse is short the phase shift is imposed almost instantaneously compared to the lifetime of the dipole moment. For the parameters shown in Fig. 3.8, the total phase shift $\Delta\phi_{max}$ is approximately $\pi/2$, giving rise to a mostly dispersive shape of the absorption profile as shown in the Fig. 3.8(c) and (d). As the XUV pulse propagates, the overall absorption profile broadens due to the reduced effective lifetime as describe above, but its shape does not change substantially since this is controlled by the size of the LIP. However, when the XUV pulse has propagated enough that the second sub-pulse appears in the XUV tail (as in Fig. 3.8(b)) a new narrow feature appears of line-center in the absorption profile (Fig. 3.8(d)). This is because the second sub-pulse is phase-shifted by π relative to to the first sub-pulse and therefore generally will give rise to absorption (as opposed to the emission on line center caused by the LIP).

Additional narrow features would appear in the absorption spectrum, nested around line center, for longer propagation distances as additional sub-pulses would appear in the XUV temporal profile. For our experimental parameters, we generally observe one or two RPP features close to the $1s2p$ resonance. We do not observe strong RPP effects around the higher lying $1snp$ states as these transitions are weaker and the temporal reshaping is therefore very small.

Finally, Fig. 3.8(a) and (b) also illustrate the time-dependent phase shift that would be imposed by a longer IR pulse, such as that used in the experiment and in the calculations shown in the remainder of the work. It is clear that the temporally extended phase shift means that at long propagation distances, the full phase shift has not yet been imposed by the time that the first sub-pulse ends. In Section 3.2.4 we will discuss how this affects both the evolution of the spectral absorption profile and the temporal XUV profile during propagation.

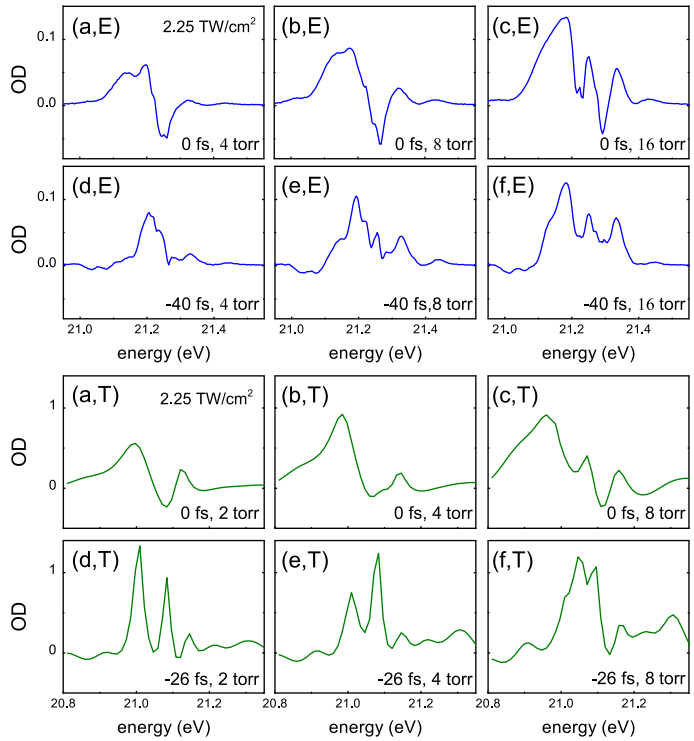

Figure 3.10: (a,E) - (f,E): Experimentally measured OD spectra around the $1s2p$ line for different pressures and delays. (a,T) - (f,T): Calculated OD spectra using comparable pressures and delays.

3.2.3 IR intensity dependent lineshape modification

In this section, we experimentally and theoretically explore the dependence of the absorption line shapes on the perturbing IR intensity. Fig. 3.9 shows the IR intensity-dependent OD spectra at some representative time delays for both experiment and theory. From top to bottom, the three delays represent a small negative delay, a delay close to overlap, and a small positive delay. For the small negative and the small positive delay, there is limited overlap between the IR and the XUV pulses. Note however that positive and negative delays are not symmetric in the effects of the IR as we discussed above, since the XUV absorption is only altered by the part of the IR pulse that arrives after the XUV excitation. The dressing IR peak intensity in the experiment is estimated to range from 0.75 ($\pm$ 0.5) to 3 ($\pm$ 0.5) TW/cm^2, however in the calculations we get the best agreement with the measured

line shape at 3 ($\pm$ 0.5) TW/cm^2 when we use an IR intensity of 1.5 TW/cm^2. For the calculated results, we also show two lower intensities of 0.25 TW/cm^2 and 0.75 TW/cm^2. We note that the experimental intensity values are overestimated as the loss at the entrance aperture of the gas cell is not taken into account. We should also point out that while the He backing pressure is 8 Torr in the experiment, the actual pressure in the 10 mm long He gas cell is smaller. Furthermore, the gas pressure in the interaction region is not uniform and varies with the size of the laser-drilled entry and exit holes on the gas cell. In all the calculations shown in Fig. 3.9 we have used a pressure of 4 Torr in the 1 mm He gas cell. This pressure has been chosen to approximately match the size of the RPP peak in the experiment, see also discussion in connection with Fig. 3.12. Lastly, the absolute values of experimental and theoretical OD differ due to the substantial IR background present on our detector, which artificially reduces the experimental OD values obtained from the weak H13 by a large amount, while having minimal effect on OD obtained from H15.

As can be observed from Fig. 3.9, a stronger IR pulse leads to a broadening and a change in the absorption line shape for all of the delays shown in the figure, in both experiment and theory. This agrees with the discussion of the LIP in the previous section - a larger IR intensity leads to a stronger coupling between excited states and therefore a larger Stark shift and a larger LIP. In the theory results, we can follow the evolution of the line shape with intensity from near-Lorentzian to near-dispersive at some delays (see for instance Fig. 3.9 (c,T) and (e,T)). In the experimental results, we are not able to lower the IR intensity enough to observe near-Lorentzian profiles for the $\tau = -20$ fs and $\tau = +30$ fs cases ((c,E)-(f,E)). This is likely due to a small leakage of the XUV-generating IR beam through the interaction chamber - this leads to a background of IR which is always present around zero delay. We nevertheless do observe increasingly asymmetric profiles as the IR intensity is increased. We note that the RPP peaks in the $1s2p$ line are visible at all intensities and for all delays, in both theory and experiment. This is as expected since the RPP reshaping is driven by the mismatch of the short XUV duration and the long lifetime of the excited states and to first order does not depend on the IR pulse.

On the other hand, as we discussed in [64], the RPP does have an influence on how the IR-perturbation reveals itself in the XUV absorption spectrum. In the following section, we will explore in more detail how the RPP and the LIP interact in our APT transient absorption scenario.

3.2.4 Gas pressure dependent lineshape modification

Figs. 3.10, 3.11, and 3.12 explore the relationship between the RPP-induced and the LIP based reshaping of the OD line shape around the $1s2p$ line. In Fig. 3.10 we show measured and calculated spectra at three different pressures and two delays. The three pressures are chosen such that at delay zero, the RPP peak is not visible at the lowest pressure (a, E&T), barely visible at the intermediate pressure (b, E&T), and prominent at the highest pressure (c,E&T) in both the experimental and theoretical results. At small negative delay (d,E)-(f,E) and (d,T)-(f,T), we see a similar trend, except the lineshapes generally consist of a narrower main peak and one or several sidebands.

Fig. 3.11 shows a detailed experimental exploration of the pressure dependence of the line shape. Fig. 3.11(a) shows the OD line shape at different pressures, at zero delay, and Fig.3.11(b)-(e) show full two dimensional maps of the OD vs photon energy and pressure for four different delays. A number of different observations can be made from these figures that all point to the complex nature of the interplay between the macroscopic RPP effect and the microscopic LIP effect: (i) The threshold pressure at which the RPP peak first appears in the OD spectrum is approximately 5 Torr and is independent of the delay. This is in agreement with the observation from Fig. 3.9 in which we saw that the appearance of the RPP peak was independent of the IR intensity. (ii) The OD line shape is changing with pressure, at most delays starting from a primarily dispersive shape at low pressure to a shape in which the RPP peak on the high energy side is so dominant that there is no longer a minimum - *i.e.* the initially dispersive line shape is no longer recognizable. (iii) At delays close to zero (including -25 fs), the bandwidth of the OD profile does increase with pressure, but slower than the linear increase with P one would expect from RPP

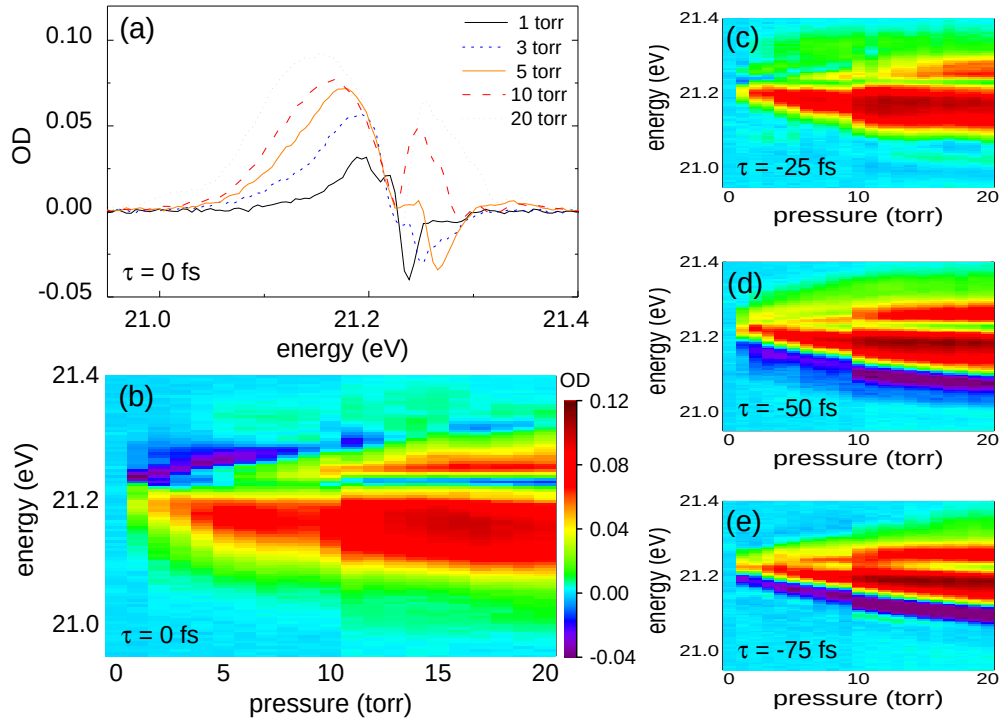

Figure 3.11: Experimentally measured OD as a function of backing pressure for the case of IR intensity of 2.25 TW/cm^2. (a) Shows line-outs of the OD at some representative backing pressures at delay zero (increasing and broadening from smallest to largest pressure), and (b)-(e) shows the full two dimensional map pressure dependence the OD at four representative delays, 0, -25, -50, -75 fs, respectively.

[83].

The evolution of the OD spectrum with pressure is equivalent to the evolution of the OD with propagation distance. This is demonstrated in Fig. 3.12 which shows a theoretical study of the evolution of the OD with propagation distance for two different pressures, 4 Torr (a-b) and 8 Torr (c-d). In the 4 Torr case, the RPP peak is only just visible at the end of the medium, as a slight increase of the OD on line center (see also Fig. 3.10(b,T)). The 8 Torr calculation (c-d) shows that, as one would expect, the line shape that has been reached at $z = 1$ mm in the 4 Torr case, is reached at $z = 0.5$ mm in the 8 Torr case, and then develops further in the remainder of the medium. We can thus directly compare the measured pressure dependences in Fig. 3.11 to the calculated propagation distance dependences in Fig. 3.12.

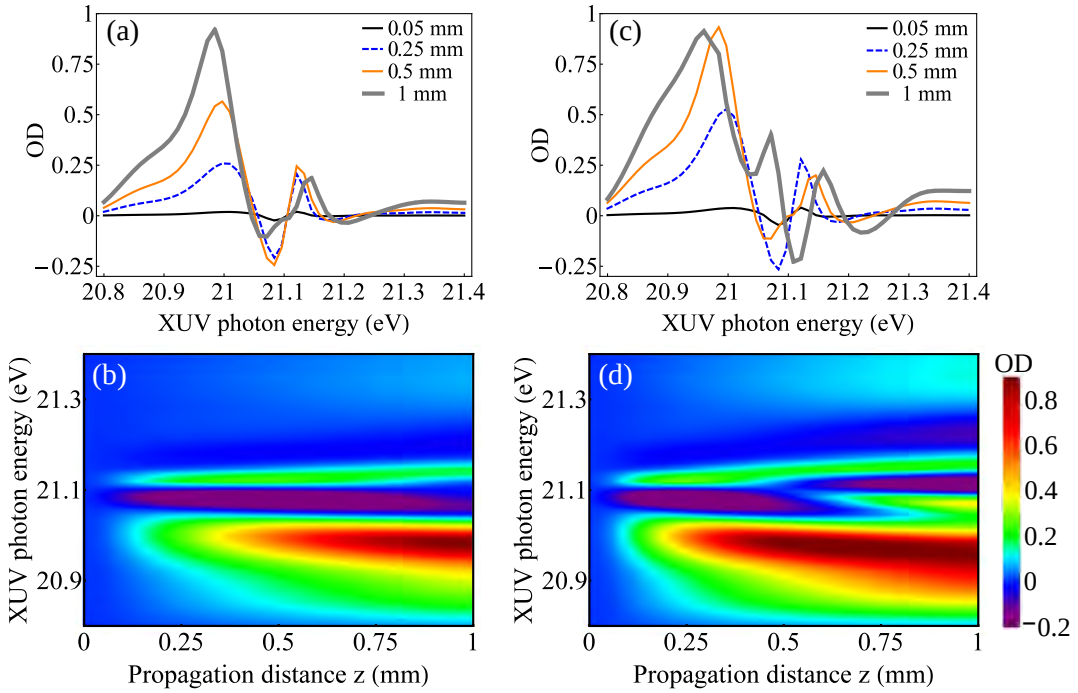

Figure 3.12: Calculated OD as a function of propagation distance for the case of 4 Torr and an IR intensity of 2.25 TW/cm^2. (a) Shows line-outs of the OD at four different propagation distances (increasing and broadening from smallest to largest z), and (b) shows the full z-evolution of the OD. Note that in (b) the color scale is chosen so that both positive and negative values of the ODD are saturated at the peaks. (c) Same as Fig. 3.12(a) except for 8 Torr. (d) Same as Fig. 3.12(b) except for 8 Torr.

The calculated results in Fig. 3.12 agree with the measured results in Fig. 3.11 in terms of points (i)-(iii) made above. We can explain these three observations in the following way, combining our understanding of RPP and the LIP: (i) The threshold pressure represents the pressure at which the XUV pulse develops a second sub-pulse in the tail. This is predominantly controlled by the strength of the ground-to-excited state coupling and the (effective) lifetime of the excited state and therefore to first order independent of the laser parameters. (ii) As the first sub-pulse gets shorter during propagation (and becomes comparable to the IR pulse duration), the propagation of the XUV pulse becomes quite complicated because the time-dependent dipole moment is driven by the combination of an XUV pulse with a

long tail and an IR pulse which imposes a phase which varies in time over the entire effective lifetime of the XUV-induced dipole moment. In addition, when the effective lifetime becomes shorter than the IR pulse duration, the full LIP will not be imposed on the dipole moment during its effective lifetime. These effects causes the line shape to dynamically change during the propagation and is the most direct effect of the RPP-LIP interaction. In the calculations (see for instance Fig. 3.12(c)), we observe that the absorption line shape indeed reflects the reduced LIP as the pulse propagates further, changing from closer-to-dispersive to closer-to-Lorentzian. (iii) The spectral broadening in the calculations also initially quickly increases and then almost saturates at longer propagation distances. This is also an effect of the long IR pulse duration - in [64] we showed that the RPP spectral broadening with propagation distance is much faster when the laser pulse is short.

The time-domain consequences of the RPP-LIP interplay are illustrated in Fig. 3.13 in which we show the initial and final XUV time profiles of the H13 part of the APT at the end of 1mm propagation in He gas at 4 Torr (a) or 8 Torr (b) pressure, when the gas is dressed by either a 33 fs (solid red) or 13 fs (dotted blue) IR pulse. First, we note that even at 4 Torr, the propagation induced reshaping is very substantial, with the area of the first sub-pulse (between approximately 4 and 40 fs) almost comparable to the area of the main pulse (between -4 and 4 fs). A second sub-pulse is barely visible beyond 40 fs. The appearance of the second sub-pulse at this pressure is consistent with the OD shown in Fig. 3.10(b,T) and Fig. 3.12(a,b) in which the RPP peak becomes visible at the end of the 4 Torr medium. Second, the additional modulation that can be observed in the middle of the first sub-pulse in the 33 fs IR case results from the interaction with the long IR pulse, since it is absent when the IR pulse is shorter. The RPP-LIP interaction is even more clearly manifested in the time profiles at the end of the 8 Torr medium (b). In this case the longer IR pulse causes not only an additional modulation of the first sub-pulse but also differs in the timing of the second sub-pulse by about 10 fs, with the minimum before the second sub-pulse changing from about 30 fs to about 20 fs. We find that if we use shorter and shorter IR pulses, the position of this

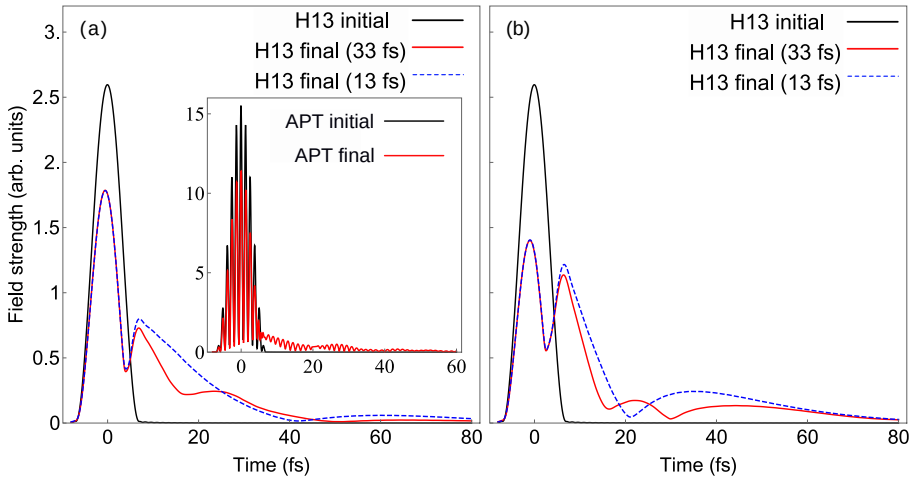

Figure 3.13: Calculated XUV time profiles, at the beginning (black) and end (solid red or dashed blue) of the helium gas at a pressure of 4 Torr (a) or 8 Torr (b), dressed by 2.25 TW/cm^2 IR pulse. The final time profiles for two different IR pulse durations are shown, 33 fs (solid red) and 13 fs (dashed blue). The inset in (a) shows the initial and final time profiles of the full APT for the 4 Torr case.

minimum converges to its IR-free position at about 18 fs. These results indicate the interaction between RPP and the IR-induced control of the time-dependent dipole moment works in both directions - RPP influences the LIP-controlled absorption line shape through the appearance of narrow absorption features, and the LIP influences the RPP-controlled temporal reshaping of the propagating pulse in the limit when the time scale of the LIP and the first sub-pulse are comparable.

The inset in Fig. 3.13(a) shows the time profile of the full APT at the beginning and end of the 4 Torr gas jet. Because H13 is only a small fraction of the APT, the tail of the APT looks much smaller compared to the main pulse, but its shape can be recognized from Fig. 3.13(a). It is interesting to note that the influence of the dipole response from the $1snp$ states, although weaker than the $1s2p$ response, is visible in the tail in the form of the half-cycle modulation of the tail which would not happen in the absence of radiation around H15[2].

[2]We note that in this plot we have not averaged over delays as we have in all other plots. We change the delay by shifting the XUV pulse in time and in the delay average the sub-cycle features are therefore strongly suppressed.

3.2.5 IR Polarization Dependent Lineshape

Finally, we study the influence of the relative polarization of the XUV and IR fields, especially as it relates to the appearance of the RPP peaks in the $1s2p$ absorption profile. All of the results discussed above, both theory and experiment, have been performed using parallel polarizations of the XUV and IR electric fields. We are only aware of one study published so far which studies the influence of the relative XUV and IR polarizations in attosecond transient absorption [115]. Reduzzi and collaborators studied the polarization-dependent transient absorption of an isolated attosecond pulse centered around the bound states in helium, in the single atom limit. They found that perpendicularly polarized fields lead to a reduced coupling between the XUV-excited manifold of $1snp$ states and nearby dark $1sns$ and $1snd$ states compared to parallel polarizations, and attributed this to the symmetries of the excited states with perpendicular (only $m = 1$ states excited) vs parallel (only $m = 0$ states excited) polarizations. This means that for perpendicular polarizations, the IR field can only couple excited $1snp$ states to $1snd$ states.

Fig. 3.14(a) compares the experimental OD around the $1s2p$ line for parallel (black) and perpendicular (red) XUV and IR polarizations. In both cases, the IR intensity is 1.8 ($\pm$ 0.5) TW/cm^2 and the backing pressure is 8 torr. The figure shows that the perpendicular case exhibits a weaker OD overall, but a stronger RPP peak. To mimic this IR-field-polarization dependence theoretically, we have performed a set of model calculations as described in [64]. Briefly, we solve the MWE coupled to a simpler solution of the TDSE for a two-level system interacting with a resonant light field.

The effect of the IR pulse is modeled as a time-dependent phase that accumulates on the upper state amplitude, proportional to the IR intensity, as if the LIP was strictly proportional to the Stark shift. The IR perturbation and the attosecond pulse begin at the same time. A change in the relative XUV and IR polarizations away from parallel is modeled as decrease in the laser-induced coupling (and thereby the LIP), due to the smaller number of states that the $1s2p$ excited state can be IR-

coupled to [115]. In our calculations, the XUV pulse is an isolated 400 attosecond XUV pulse centered on 21.1 eV, the IR pulse has a FWHM duration of 13 fs, and we impose a $\sim$ 110 fs decay time on the time-dependent atomic polarization. In Fig. 3.14(b) we show results for three different coupling strengths γ, where the LIP at $\gamma = 1$ has been chosen such that the OD line shape and the appearance of the RPP peaks are similar to those of the experiment for parallel polarizations [3]. The theory results also show that there is a range of parameters for which a reduced IR perturbation leads to larger RPP peaks. In the calculations, this happens because the IR-controlled line shape corresponding to the two different perturbations is different. In particular, the larger perturbation leads to a line shape which has a deeper minimum on line center at the propagation distance when the RPP peak starts to appear. This means that the RPP peak has to grow from a lower OD value than in the smaller perturbation case, in which the line shape starts out more asymmetric and with a shallower minimum. This difference in the basic shape can still be recognized at the end of the medium as in Fig. 3.14 even though the OD line shape has undergone substantial change during the propagation. This difference in the line shapes can also be seen in the experimental results, where the basic line shape in the perpendicular case is more dispersive (indicating a phase shift of approximately $\pi/2$), whereas the line shape in the parallel case has a more pronounced peak on the high-energy side, indicating a phase shift larger than $\pi/2$ (the limiting, symmetric, case of a window-resonance-like shape would correspond to a phase shift of π). These polarization dependence results thus also indicate that for dense gases, the RPP effect can have a substantial effect on how the IR perturbation manifests itself in the absorption spectrum and should be taken into account if the absorption line shape is to be used to characterize IR-induced dynamics.

[3] We note that the model calculations in general predict OD values much larger than those of the experiment and the full calculations, even when the line shape and the general evolution with propagation distance generally agree. In addition, the experimental peak values of the OD around the $1s2p$ line are artificially reduced by the background of IR leakage

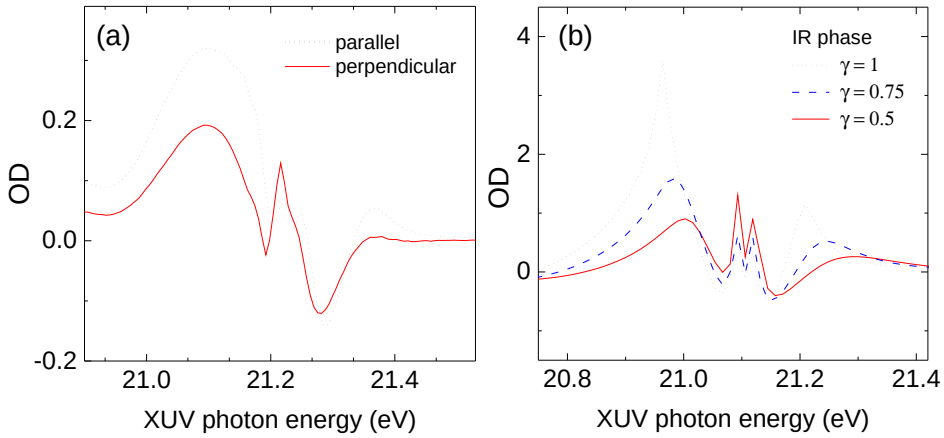

Figure 3.14: (a) Experimentally measured spectral lineshape at delays close to zero with different pump-probe polarizations. The black curve is parallel (0°) geometry and the red one is perpendicular (90°) geometry. (b) Theory results calculated using the 2-level TDSE-MWE model (see text). We show three different strengths of the IR-induced coupling, modeling the change from parallel polarizations ($\gamma = 1$, solid black) to non-parallel polarizations ($\gamma = 0.75$, dashed blue, and $\gamma = 0.5$, solid red).

3.2.6 Summary

In this work, we have presented a joint experimental and theoretical study of transient absorption of an APT by a dense, helium gas. We have systematically explored the evolution and modification of the absorption line shape with IR-XUV delay, IR intensity, gas pressure, and the relative polarization of the XUV and IR pulses. We have focused on elucidating how the interplay between the microscopic IR-laser-dressing and the macroscopic RPP reshaping affects the transient absorption of the attosecond XUV pulse. To this end we have employed both time- and frequency-domain descriptions of the light-matter interaction. We have demonstrated that the absorption line shape is controlled not only by the IR pulse through its delay and intensity as it is in the single atom limit, but is also influenced by collective effects induced during propagation through the resonant medium. For small optical thicknesses, we have shown (as in [64]) that RPP leads to the appearance of narrow absorption features on line center which are absent in the single atom response. For larger optical thicknesses, RPP effects can lead to substantial dynamical reshaping

of the absorption line shape, in particular when the duration of the IR pulse is long compared to the duration of the first sub-pulse in the propagating XUV light. The reshaping can be understood in terms of an effective reduction of the LIP, since a long IR pulse means that only part of the total LIP will be induced over the first XUV sub-pulse. We also showed that the presence of the dressing IR field influences the resonant XUV propagation dynamics. In particular, we showed that for long IR pulses, the presence of the dressing field changes the time structure of the propagating XUV pulse.

The results in this study demonstrate that the full description of the interaction of an attosecond XUV pulse with a dressed, optically thick medium must include a truly dynamical feedback between the dipole moment of the individual atoms and the time structure of the propagating pulse. Our study has illustrated and explained what we believe to be the basics of how the XUV transient absorption spectrum develops as a function of XUV-IR delay, IR intensity, and gas pressure. This understanding of the fundamental but complicated features of transient photo absorption will be crucial in extending this powerful time-resolved spectroscopic tool to more complicated and high-density systems such as plasmas and condensed phase systems.

3.3 Part III: The Quantum Path Interference, Wavelength-dependent Effects, and Beyond

(A portion of this section is adapted from C.-T. Liao *et al.*, "XUV Transient Absorption Spectroscopy: Probing Laser-Perturbed Dipole Polarization in Single Atom, Macroscopic, and Molecular Regimes.", Photonics 2017, 4(1), 17, as in Ref. [7].)

3.3.1 Temporal and spectral properties

As a first example, we discuss the basic phenomena underlying XUV transient photoabsorption in helium atoms exposed to strong NIR fields—a topic that forms the basis of understanding most ATAS measurements. The experimental spectrogram

is shown in Figure 3.15a, where we clearly observe time-dependent transient absorption corresponding to helium levels excited from the ground state by XUV pulse, ranging from 1s2p, 1s3p, 1s4p, 1s5p, to the continuum. The field-free locations of helium energy levels below single electron ionization potential (Ip) are labeled on the right side of the figure for reference. In Figure 3.15b, we show the transient absorption lineshapes corresponding to atomic resonances, which are obtained by taking the lineouts of the spectrogram in Figure 3.15a at a delay of –5 optical cycles . It should be noted that we averaged over two cycles to generate these lineouts. In addition, due to the discreteness of our XUV spectrum, there are very few XUV photons at 3p energy and we observe very weak signal (not shown) from that state. Transient absorption lineshape details are determined by the NIR laser parameters as we discuss below.

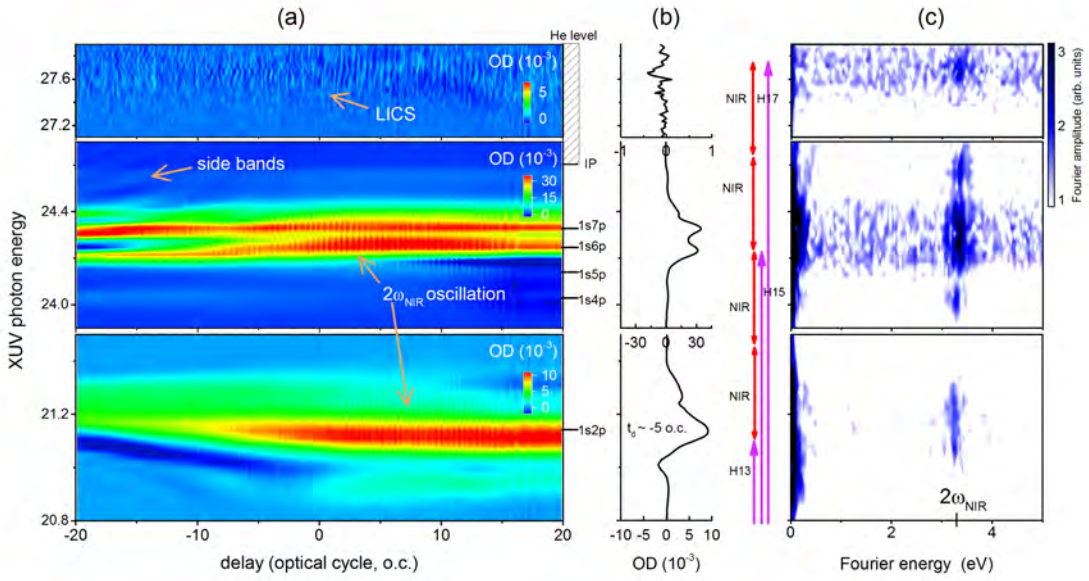

Figure 3.15: (**a**) experimental transient photoabsorption spectrogram obtained in the helium gas, where relevant energy levels are labeled on the side of the figure. The NIR photon energy used here is 1.59 eV (780 nm); (**b**) lineouts showing transient absorption lineshapes near –5 optical cycles (averaged over two cycles). The purple and red arrows indicate XUV and NIR coupling pathways. (**c**) Fourier analysis of the spectrogram from (**a**). The Fourier amplitude is in arbitrary units and on a logarithmic scale.

In the single-atom response assumption (dilute gas limit), we can discuss the XUV initiated dipole polarization in helium Rydberg states as the collection of time-dependent electric dipoles, which can be analyzed using a semi-classical treatment. The XUV initiated ringing and exponentially decaying dipoles, $d(t)$, will show conventional Lorentzian absorption line shapes in the frequency domain in the absence of the NIR field. The static photoabsorption cross section of this dipole can be represented as $\sigma(\omega) \propto \mathrm{Im}[d(\omega)\mathcal{E}^*(\omega)]$ [116], where $d(\omega)$ and $\mathcal{E}(\omega)$ are the Fourier transform of the time-dependent dipole and the total applied electric field, respectively. When an NIR pulse is applied to these dipoles, it effectively kicks (phase shifts) oscillating dipoles. If NIR arrives at large time delays, the NIR perturbed free-induction decay (FID) [117] manifests as broadened Lorentzian line shape with sidebands, as seen from the middle panel in Figure 3.15a. Then, the XUV and the NIR pulses overlapped, strong modifications, resulting in a Fano-like line shape, can be observed. The line shape modification can be explained qualitatively in terms of laser-induced phase (LIP) shift on dipoles, and this phase shift $\phi(t, t_d)$ can be estimated from the pondermotive or Stark shift [118, 119], i.e.,$\phi = \Delta E(t, t_d)t/\hbar$, where $\Delta E(t, t_d)$ is pondermotive energy. The experimentally observed absorbance change due to the NIR can then be obtained as $OD(\omega, t_d) \propto [\sigma_{\mathrm{XUV+NIR}}(\omega, t_d) - \sigma_{\mathrm{XUV}}(\omega)]$.

In our experiment, we used SIGC to generate XUV, which is focused on the target helium gas along with NIR peak intensity 1 ($\pm$0.5) TW/cm^2, and the helium backing pressure in the sample cell is $\sim$267 Pa. From the spectrogram in helium (Figure 3.15a), we can observe the development of structures in 1s2p state due to AC Stark shift [120], which results from NIR induced one photon coupling from a bright state such as a 1s2p state to a nearby dark 1sns or 1snd state. The delay axis of spectrogram is calibrated in optical cycles, such that one cycle corresponds to $\sim$2.6 fs of 780 nm ($\sim$1.59 eV) NIR laser used in this experiment, and we can clearly observe sub-cycle oscillations in the transient absorption spectrogram. These subcycle oscillations, also called $2\omega_{\mathrm{NIR}}$ oscillation, are a common feature in attosecond transient absorption experiments [120, 121], especially when commensurate energy XUV and NIR photons are used. These oscillations can be observed in our data

by performing Fourier transform along time delay axis from the spectrogram to get Figure 3.15c. For 1s2p energy and some high-lying 1snp states, the Fourier analysis shows strong signals at ∼3.2 eV, which is the $2\omega_{\text{NIR}}$ oscillation. This oscillation can be understood as two-photon NIR coupling between the polarizations created by H13 and H15, leading to beating at a frequency corresponding to the energy difference between 1snp and 1s2p states. As indicated in Figure 3.15b, there are two pathways to 1s2p state (by H13 or H15-$2\omega_{\text{NIR}}$), and similarly to 1snp polarization (by H15 or H13 + $2\omega_{\text{NIR}}$).

Note that, from the spectrogram in Figure 3.15, we can also observe very weak signal at around 27.7 eV. In this energy range, there are no known energy levels, or autoionizing states, embedded in helium continuum, so it should show featureless continuum absorption. On the contrary, we observe features in this range that can be attributed to the so-called laser-induced continuum structure (LICS). This effect was first discussed in the 1970s [122, 123], and it has been reviewed in Ref. [124]. The subcycle oscillation in LICS is due to two pathways of photoexcitation, where one is excitation directly from ground state by H17 and the other is the promotion of an electron from 1snp state polarization with two NIR photons. As a result, we can again observe quantum beat signal in Fourier analysis similar to $2\omega_{\text{NIR}}$ oscillation in the case of 1s2p and 1snp polarizations.

3.3.2 Pressure and wavelength dependence

Most experiments in recent years assume single-atom response in their transient absorption experiments. However, the experimental densities in these experiments often approach a limit where the simple Beer-Lambert law is no longer valid and macroscopic effects should be taken into account. We have explored this regime in our recent studies [64, 89], where we show that the collective macroscopic XUV pulse propagation effect, also called the resonant pulse propagation (RPP) effect, should be considered. We also laid out the criteria for consideration of gas target as an optically thick medium. Here, we provide a simple overview of the complex interplay between LIP effect and RPP effect by summarizing it in a schematic of

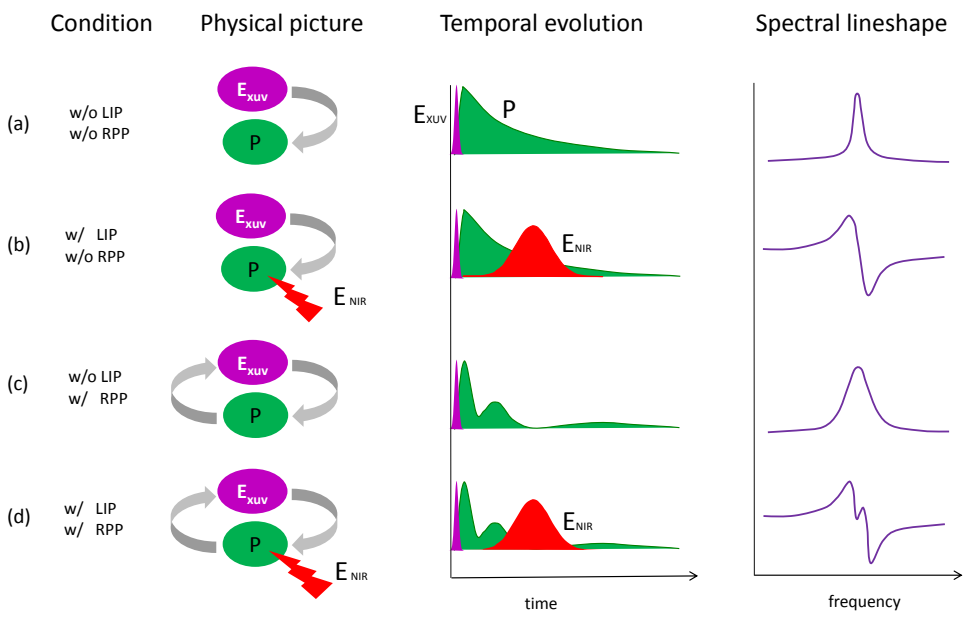

Figure 3.16: A schematic that summarizes various phenomena that determine the temporal and spectral properties of XUV excited dipole polarization in a simplified two-level resonant system. (**a**) The impulsive XUV field (E_{XUV}) prepares dipole polarization (P), which decays exponentially, leading to Lorentzian spectral lineshape. (**b**) When laser-induced phase (LIP) shift is applied by a time-delayed NIR field (E_{NIR}), a Fano-like dispersive lineshape is observed. (**c**) The polarization is temporal reshaped by resonant pulse propagation (RPP) effect in a dense medium. (**d**) The interplay between RPP and LIP effects leads to the appearance of new spectral features in the lineshape.

Figure 3.16. The first column indicates experimental conditions, and the second column is the physical picture of the interaction, followed by its temporal description on the third column, and its corresponding spectral profile in the last column. In single-atom response picture—as explained in Section 3.3.1 and shown in Figure 3.16a—when XUV pulse alone (E_{XUV}) excites the dipole polarization (P) of a resonant medium, the Fourier transform of this oscillating and decaying polarization shows a Lorentzian spectrum in the frequency domain. The introduction of strong, time delayed NIR pulse (E_{NIR}) (Figure 3.16b) imparts an additional phase on the polarization, and this LIP effect results in a Fano spectral line shape. When an XUV propagation alone in a dense medium is considered (Figure 3.16c), the polar-

ization created by the incident XUV is strong enough to radiate XUV light, and this emission could further excite secondary polarization.

In this self-consistent dipole-field interaction picture, the final polarization will be temporally reshaped and it can be described by a Bessel function of the first kind (J_1) [110] as $E_{XUV}(z,t) \propto J_1(\Gamma P z t)/\sqrt{t}$, where Γ is the decay lifetime, P is the gas pressure, and z is the propagation distance. Therefore, the pressure-length product zt determines the reshaping of XUV pulse in a dense resonant medium. The temporal reshaping manifests as broadened spectral lineshape. An important feature of the reshaped XUV pulse profile is that the first sub-pulse will be out-of-phase compared to the original pulse, the second sub-pulse will be out of phase compared to the first sub-pulse, and so on. These temporal phase variations can be brought to light using the presence of delayed NIR pulse, where the NIR pulse samples the π phase jumps between sub-pulses, and the LIP effect serves to broaden the fine spectral structure associated with these phase jumps. The non-linear interplay between RPP and LIP can thus be clearly seen through the appearance of new spectral features in the experimental transient absorption lineshape. It should be noted that, for this to happen, the duration of the first XUV sub-pulse has to be comparable or smaller than the NIR pulse duration, which means that pressure-length product has to be high enough to significantly reshape the XUV pulse through RPP effect.

In order to experimentally demonstrate the interplay between RPP and LIP effects, in Figure 3.17a, we show 1s2p state evolution, at 400 Pa and 1200 Pa backing pressure for 786 nm laser wavelength, at –30 fs time delay, and $\sim$2 TW/cm^2 laser intensity. As gas pressure is increased, we clearly observe the appearances of new spectral features (indicated by vertical dashed line) near the line center of an otherwise simple Fano like profile. We also used an OPA to convert original NIR pulse to 1428 nm NIR pulse with similar pulse duration but weaker peak intensity at $\sim$0.2 TW/cm^2. The bottom curve in Figure 3.17a shows the 1s2p line profile evolution under 1428 nm NIR imposed LIP effect at the same backing pressure (1200 Pa) and time delay (–30 fs). Although this intensity is an order of magnitude weaker,

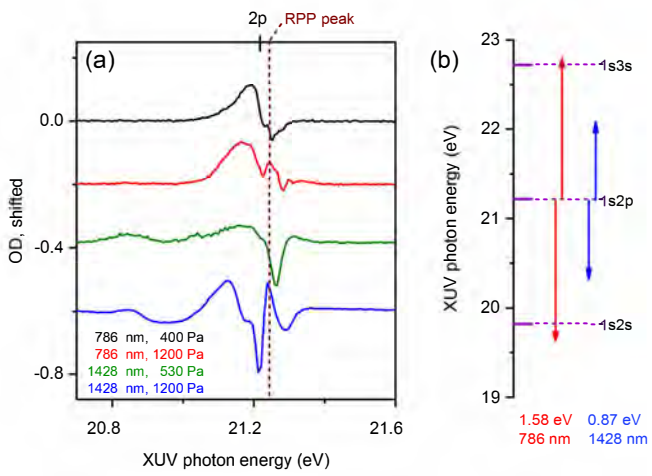

Figure 3.17: (**a**) experimental spectra of helium 1s2p state evolution which show both LIP and RPP effects at 786 nm NIR wavelength at gas pressure of 400 Pa (black) and 1200 Pa (red), and 1428 nm NIR wavelength at gas pressure of 530 Pa (green) and 1200 Pa (blue). Field free states are labeled at the top, and the RPP induced feature is shown by the dashed line. (**b**) NIR one-photon coupling pathways leading to different amounts of LIP effect for the two NIR wavelengths.

the LIP effect depends on the pondermotive energy shift that is proportional to $I\lambda^2$, where I is the peak intensity of the laser and λ is the laser wavelength, so the LIP effect in the case of longer wavelength should only be three times smaller. We observed that the dispersive effect of 1428 nm light is actually similar compared to the 786 nm case, as seen from the overall broadening of the spectral lineshapes in the two cases. The quantitative comparison between these two cases requires calculation of the LIP effect by including one-photon couplings to nearby states. In our case, NIR couplings pathways to nearby dark 1sns states from the bright 1s2p state are shown in Figure 3.17b. Depending on the detuning, the dipole strength of these transitions and the NIR intensity dependent Rabi Frequency, we will observe different AC Stark shift and line profiles in two cases. The calculations for 1s2p states reported in [117] do show that it is possible to have wider lineshape for higher detuning cases. The overall line shape in 1428 nm case also shows an especially strong RPP peak when compared to the 786 nm NIR case. Detailed understanding of exact spectral features is not trivial, and it requires macroscopic calculations

where a time-dependent Schrödinger equation calculation is coupled to the Maxwell wave equation based propagation.

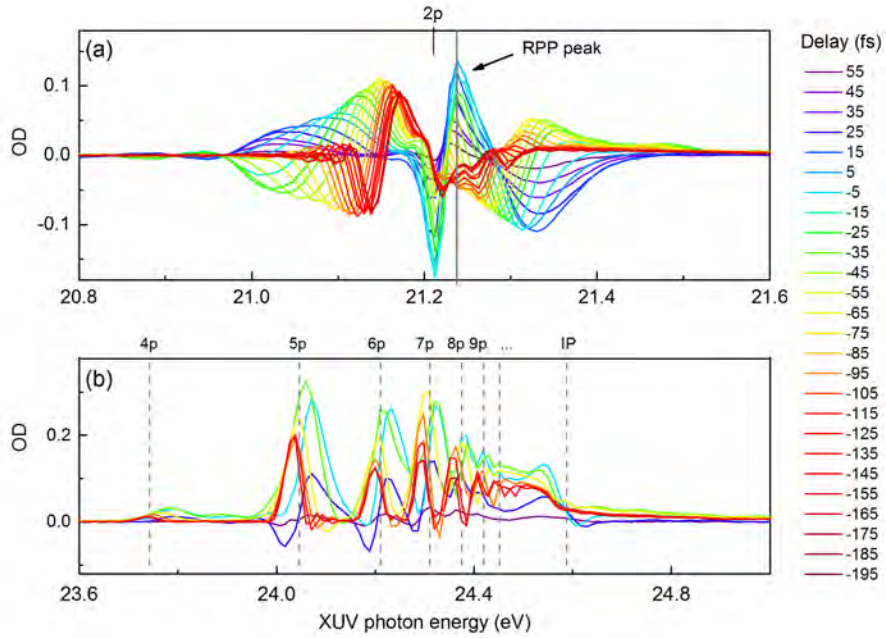

Figure 3.18: Overlaid transient absorption spectra at dense helium 1s2p state (**a**) and 1snp states (**b**), dressed by 1428 nm NIR pulse at ∼0.2 TW/cm^2 and 1600 Pa backing pressure. Vertical gray dashed lines are field-free energy level.

If we continue looking at the long wavelength (1428 nm) case and further increasing helium gas backing pressure to 1600 Pa, we can enhance the main RPP peak so that it becomes comparable or greater in strength than the original Fano profile peaks as seen in Figure 3.18a. Importantly, we can observe that, as the time delay is varied, the RPP strength changes monotonically; however, the dispersive Fano profile around the RPP peak changes its nature quite dramatically and going to positive to negative time delay results in complete reversal of the signal of OD. As for 1snp states in helium, including n = 4, 5, 6, 7,... to ionization potential (IP), the transition strength is much smaller, and hence the RPP effect is not very significant; therefore, most states show Fano-like profiles even with dense gas as shown in Figure 3.18b. Note that vertical gray dash lines are field-free energy level, and the 'real' 1s2p and 1snp state under strong field dressing will be pondermotively shifted

toward higher energy as shown in Ref. [125].

3.3.3 Three-pulse experiment: towards 2D spectroscopy

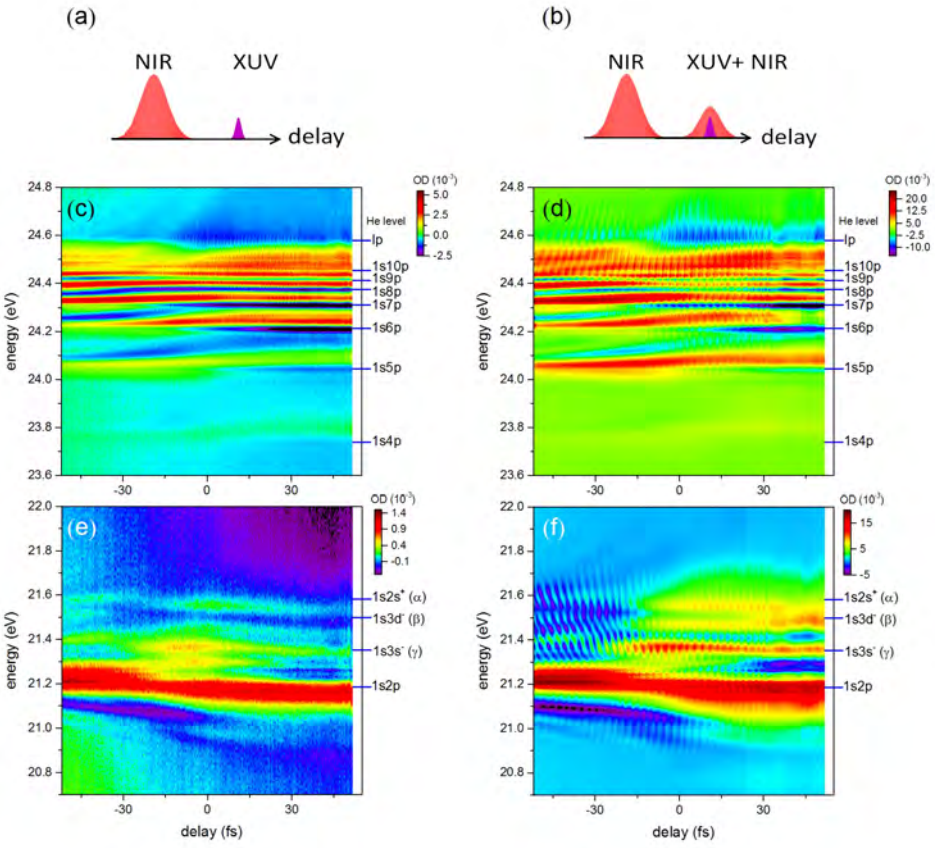

Figure 3.19: (a) The two-pulse pump-probe measurement. (**b**) The three-pulse scheme, which includes an additional NIR dressing pulses at delay zero. (c) ATA spectrogram on helium 1snp state.(d) ATA spectrogram on helium 1snp state with an additional NIR dressing pulse. (e) ATA spectrogram near helium 1s2p state. (f) ATA spectrogram near helium 1s2p state with an additional NIR dressing pulse.

To demonstrate other effects one can study in helium target, we now use the waveguide to generate XUV. In this case, H13 and H15 have slightly broader bandwidth so we can investigate other interesting phenomena such as light-induced state (LIS). The spectrograms from 1s2p and 1snp are shown in Figure 3.19(c) and (e), respectively. From Figure 3.19(e). We can recognize that there are some new ab-

sorption features appeared in this case, including feature α, feature β, and feature γ. These three new abortion lines are two-photon two-color coupled LIS. Feature α is due to the adsorption of H13+1ω_{NIR} to 1s2s dark state (1s2s^{+}) as illustrated in Figure 3.20(a), and feature β and feature γ are due to the adsorption of H15-1ω_{NIR} to 1s3d and 1s3s dark states (1s3d^{-} and 1s3s^{-}), respectively.

In addition to typical ATA scheme of NIR-pump and XUV-probe (including XUV-initiation) as shown in Figure 3.19(a), we can introduce another weak phase-locked NIR pulse overlapped with existing XUV pulse as illustrated in Figure 3.19(b). In this scenario, we can use this additional NIR pulse to initiate other dark states at zero-delay. Therefore, in addition to 1snp states, we can coherently prepare other atomic polarizations such as 1snd or 1sns states such as those in Figure 3.20(a). The measured spectrogram in this two NIR experiment is shown in Figure 3.19(d) and (f). The evolution of these complicated polarizations shows very rich dynamics comparing to single NIR pumping experiments in Figure 3.19(c) and (e). First, the major difference we noticed is that the spectrograms show extra 1ω_{NIR} oscillation due to the NIR-NIR intensity modulation as they interfere with each other. Also, this extra 1ω_{NIR} at different states show different phases as in Figure 3.20(b). For example, 1s3s^{-} LIS (red curve) in Fig. 3.20(b) evolution and 1s3s^{-} LIS evolution are out of phase at negative delay at $\sim$ -40 fs, and then they become in phase at $\sim$ 10 fs. These delay-dependent phases between different states are due to intrinsic dipole phase of the photoexcitation of that particular states, as well as two NIR photon induced interference. Note that although these two NIR pulses are individually phase-locked to XUV, they may have relative phase shift as we measured in [125].

The ATA scheme with two NIR pulses can be further applied in time-resolved four-wave-mixing spectroscopy to study coupling dynamics between odd and even parity of inner-valence excited states [126], or to generate non-commensurate XUV emissions with new photon energy from sum frequency generation or difference frequency generation. The real advantage and application potential of this three-pulse scheme comes from varying both NIR pulses to perform two-dimensional spec-

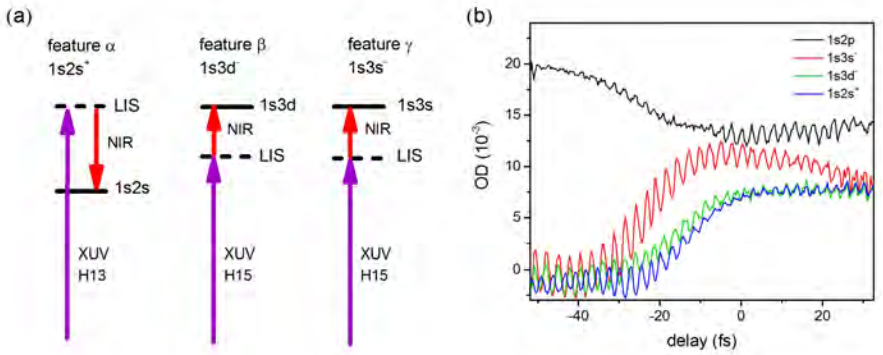

Figure 3.20: (**a**) Schematic two-photon two-color absorption pathways leading to three light-induced "virtual" states near helium 1s2p state as observed in Figure 3.19(**c**)-(**f**), where feature α, β and γ correspond to those labeled in Figure 3.19(**e**)-(**f**). (**b**) Line-outs from Fig.3.19(f) comparing temporal evolutions of dressed 1s2p state and other three dressed light-induced states.

troscopy by implementing Fourier analysis on two delay axis. The application and realization of two-dimensional or even multi-dimensional spectroscopy by attosecond and few-femtosecond pulses could help us map out the quantum mechanical evolution of vibrational and electronic couplings and transfer, especially in larger molecular systems or other ultrafast many-body physical systems where complicated couplings and coherences may occur.

3.3.4 Summary

In summary, we have applied XUV transient absorption to study the laser induced modification of excited states of helium. We have explored a range of gas density, laser wavelength and time-delay parameters in these studies. In the dilute helium experiment with the standard pump–probe setup, we observed the AC Stark shift, the quantum path interference, the laser-induced continuum structure, etc. In the dense helium target, we observe new and complex spectral features due to the interplay between laser-induced phase shift effect and the resonant pulse propagation effect. We discussed the comparison between a long and short wavelength NIR perturbation. In advanced three-pulse pump-dress-probe setup, we investigated os-

cillating phase delays of the spectra for different dressed light-induced states. This three-pulse scheme can be further extended to observe four-wave mixing spectra and to conduct two-dimensional spectroscopy for exploring complex coherence in excited complex systems, especially for larger molecules. Also, the use of extra dressing pulse brings out new effects which would not otherwise have been observable. Further work along these directions will serve to demonstrate the power and applicability of the ATAS, as the XUV research and attosecond science community moves to study complex systems, where correlation and couplings' driven charge and energy transfer mechanisms remain open questions.

3.4 Part IV: Floquet States and Four-wave Mixing

3.4.1 Floquet formalism

When describing strong-field light-induced electronic couplings in atomic systems, the Floquet formalism [127, 128] provides a convenient framework to treat an electron from an atom (as an oscillator) in the oscillating electric field (as a temporal periodic potential). The analogy of Floquet theory is the well known Bloch theory in solid-state physics, in which Bloch wave function is utilized to treat an electron from solid (as an oscillator) in the lattice (as a spatial periodic potential). Briefly, the dynamics of an atom in a periodic external electric field follows time-dependent Schrödinger equation in atomic unit as

$$i\frac{\partial \Psi}{\partial t} = [H_0 + V(t)]\Psi(t), \tag{3.2}$$

where H_0 is the field-free atomic potential and $V(t)$ is a periodic external potential. In the Floquet formalism, the solution can be written as

$$\psi_\alpha(t) = e^{-i\epsilon_\alpha t}\sum e^{-In\omega t}\phi_{\alpha,n}, \tag{3.3}$$

where ϵ_α is the complex quasi-energy, and its imaginary part is $-\Gamma/2$ with Γ the line width or the decay rate of the Floquet state, $\phi_{\alpha,n}$ is the the time-independent wavefunction for the nth Fourier component of the α Floquet state and ω is the

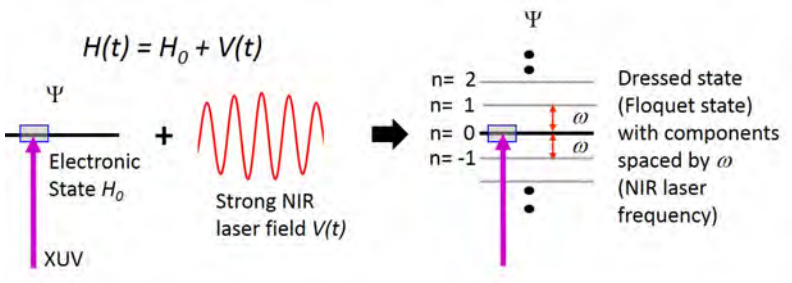

Figure 3.21: The schematic of Floquet formalism, which his formed by combining a time-periodic potential with an electronic state.

frequency of the external periodic electric field. As a result, in the presence of a temporal periodic field such as the laser field, the electronic structure can be conveniently described by Floquet states, where each bound state is associated with many one photon spaced sidebands or Fourier components as shown in the schematic Fig. 3.21. How do we test and utilize Floquet theory in our study? In fact, in many of our time-resolved photoelectron experiments by VMI, we can easily apply Floquet theory to quantitatively understand the quantum-path interference or the quantum beat spectroscopy performed by IR+XUV in helium Rydberg states by N. Shivaram *et al.*, [8, 129, 130].

On the other hand, using photoabsorption spectra, we may observe similar behaviors. To conduct the experiment using ATAS, here we use a SIGS to generate red-detuned XUV in xenon gas. Therefore, the H13 is not in resonant with 1s2p state of helium, and the H15 is in resonant with 1snp n=4,5,6,... state. The infrared (IR) photon energy is controlled by an OPA with pulse duration at the range of30-70 fs with estimated peak intensity ∼0.5–1.5 TW/cm^2. Our experimental ATA spectrograms are shown in Fig. 3.22, where the color scheme is chosen so that the two IR photon sidebands (1snp $\pm$ 2ω) from 1snp states can be observed clearly. The horizontal dashed lines are the guide to the eye, indicating the relative energy shift (moving up or down) of these emission sidebands when tuning IR photon energy. The energy of those sidebands can be well understood by Floquet theory with two IR photon spacing mainly from 1s4p state, as illustrated in Fig. 3.23(a). Unlike the experiments in typical photoelectron spectra, the one IR photon spacing side-

bands are not dipole-allowed photoexcitation due to the forbidden np to (n±1)p transitions.

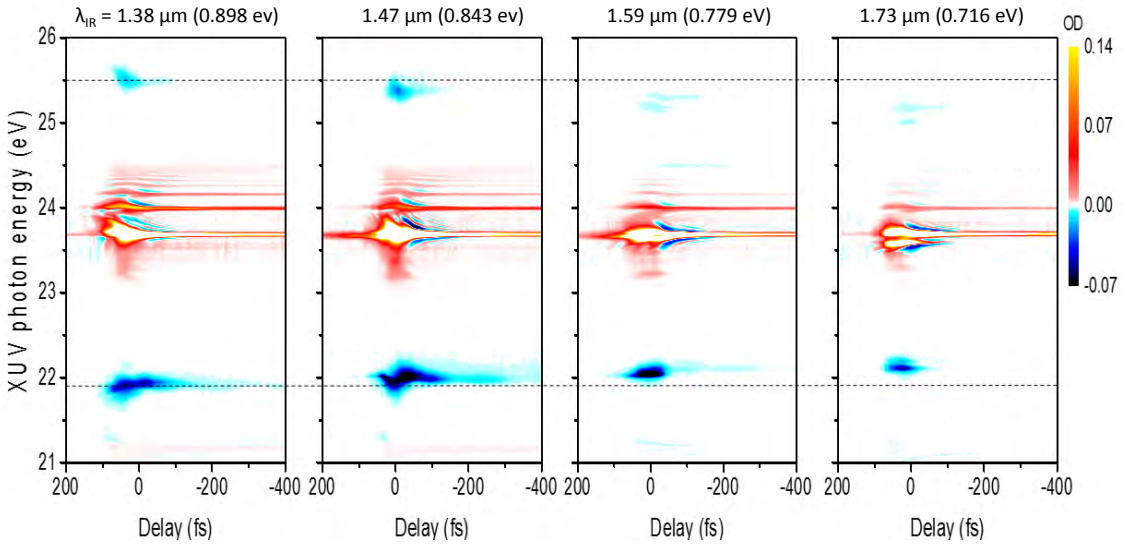

Figure 3.22: ATA spectrograms in helium with tunable IR photon energy. The relevant IR photon energy is labeled on the stop. The horizontal dashed lines are the guide to the eye, indicating the relative energy shift of these emission sidebands when tuning IR energy.

Interestingly, the top emission sidebands come from a dressed Floquet state above the ionization potential (IP) of the field-free helium, which indicates that there is transient population in the continuum state as we observed before in Fig. 3.15(a) with 780 nm (1.589 eV) IR photon. The difference is that here we can unambiguously observe these dressed states because of the non-commensurate IR photon energy comparing to HHG. Besides, due to the use of this non-commensurate IR photon energy, there are no common transition pathways available leading to the quantum path interference. Note that these is the 1s3p at 22.92 eV below 1s4p state, and if we tune the IR photon energy close to this state at 0.82 eV (1.51 μm), we can significantly enhance the sideband emission by populating more electrons to Floquet dressed states.

Note that these sidebands show negative OD, namely, they are actually XUV

emissions from dressed states as depicted in Fig. 3.23(a). An alternative approach to understand this emission process is to adapt the mechanism widely used in nonlinear optics– the four-wave mixing (FWM) process.

3.4.2 The XUV emission by the four-wave mixing (FWM)

The four-wave mixing (FWM) is a parametric nonlinear effect due to the third-order electric susceptibility or the optical Kerr effect. The FWM has widespread applications such as signal switching, phase-sensitive amplification, nonlinear microscopic imaging, single-photon source, and quantum communications [131]. In fact, the OPA we used in this experiment is based on the FWM process in some nonlinear crystals. It usually requires large and broadband optical nonlinearities to control light with light, and this makes the wavelength conversion challenging when working in ultraviolet spectrum especially for vacuum ultraviolet (VUV), XUV range, and beyond. Apart from using expensive and sparse large facilities such as the synchrotron radiation and the free-electron laser, one of the common approaches to generating table-top coherent VUV/XUV is to utilize the HHG source. However, the selectively and tunability of HHG is strongly limited to the wavelength and peak intensity that the driving IR laser provides. On the other hand, the FWM has been demonstrated as a useful technique in IR and visible spectrum. There is also some FWM implementation for deep UV and VUV generation via the FWM or the third harmonic generation from atomic gases [132–135]. However, there are only a few experimental demonstrations on new color generation in XUV range by ATAS in atoms [136, 137].

In the viewpoint of the FWM process, we can easily understand that our emission sidebands from helium shown in Fig. 3.22 are generated by either sum frequency generation (upper two-photon sidebands) or difference frequency generation (bottom two-photon sidebands) as illustrated in Fig. 3.23(b). In this case, we utilize helium as a Kerr nonlinear medium, and we can produce strong FWM signals when the phase mismatch is minimized as in dense helium gas. The sum frequency generation signal or the emission signals from the continuum can also be interpreted as the

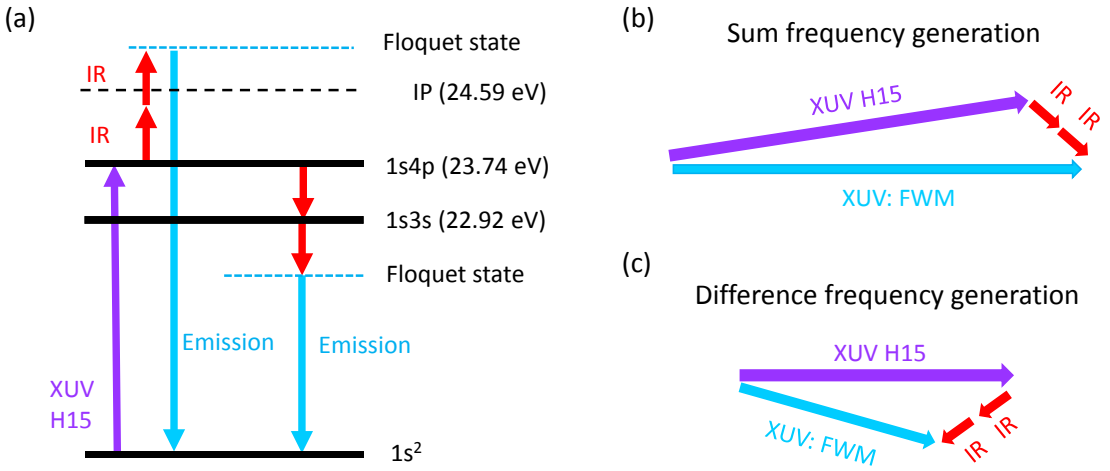

Figure 3.23: (**a**) The schematic energy level of helium 1snp states corresponding to the spectrograms observed in Fig. Fig. 3.22. Blue arrows are the emission from two IR photon Floquet (**a**).

emission from laser-induced autoionizing-like structures [138, 139]. In addition, one could expect to apply similar techniques, termed Stark-chirped rapid adiabatic passage [140], to enhance this continuum state emission by properly controlled detuning as demonstrated by using nanosecond and picosecond pulses in Ref. [132–135].

3.4.3 The IR wavelength dependent strong-field photoabsorption cross section

From previous two sections, we explored some properties in helium Rydberg states dressed by a wavelength tunable IR pulse. Specifically, we adapted a simple LIP dipole model, the Floquet Formalism, and the FWM process.

In fact, the complete picture with tunable IR wavelength is more complicated than what we have studied. In the following, we show some calculated results in collaboration with Prof. Xiao-Min Tong at the University of Tsukuba in Japan to investigate the strong-field photoabsorption cross section at different IR wavelengths and IR peak intensities. Figure 3.24(a) shows TDSE calculated photoabsorption cross sections of helium as a function of IR laser intensity, adapted from Ref. [8]. Figure 3.24(b) and (c) shows the new calculation of the photoabsorption cross section of helium dressed by 1200 nm – 1800 nm IR pulse as a function of IR intensities. In

Fig. 3.24(b), the calculation only includes helium bright states, which are one-photon dipole allowed 1snp Rydberg states below the IP. In Fig. 3.24(c), the calculation includes both bright states and dark states. The dark states are 1s2s, 1s3s, 1s4s, 1s5s, 1s3d, 1s4d, 1s5d, 1s4f, 1s5f states of helium, which are not single-photon transition allowed. By comparing these two figures, we observe that helium will show very rich and complicated cross section when dressed by strong IR field with tunable wavelengths and intensities. Also, we can now understand that the complexity stems from the active dark states involved in the process.

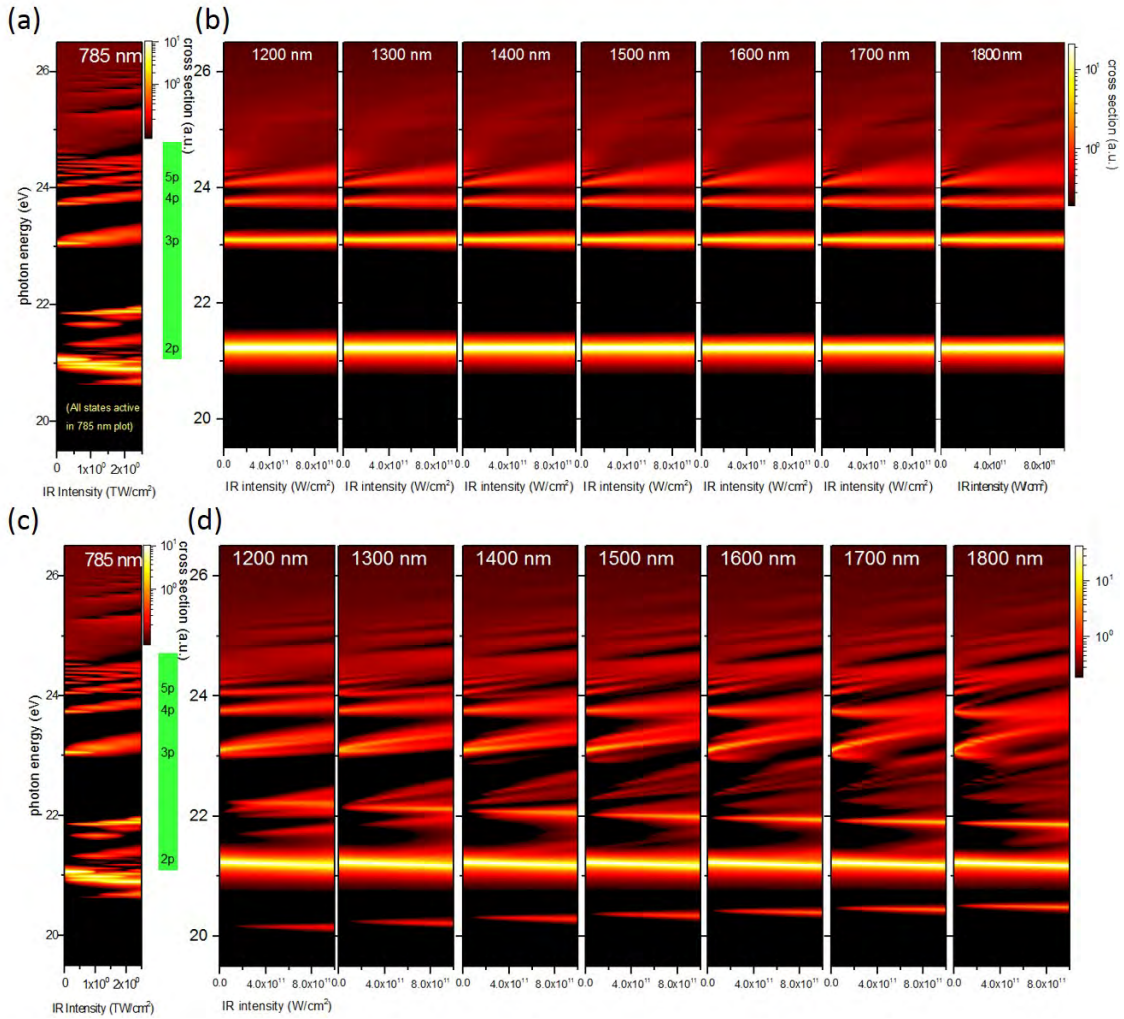

Figure 3.24: The TDSE calculated XUV photoabsorption cross section of helium as a function of IR laser wavelength and intensity. (**a**) The cross section of helium with all states active dressed by 785 nm IR pulse, adapted from [8]. (**b**) The cross section of helium with only bright (1snp) states active, dressed by 1200–1800 nm IR pulse. (**c**) The cross section of helium with all states (1snp, 1sns, 1snd, 1snf) active, dressed by 1200 nm – 1800 nm IR pulse. The green label shows helium 1snp states. The IR wavelenths used are labeled in white at the top of each 2D map. Calculation by X.-M. Tong (private communication, 2017).

CHAPTER 4

The Oxygen Experiment

(The majority of this chapter, except for Sec. 4.9, is adapted from Chen-Ting Liao, Xuan Li, Daniel J. Haxton, Thomas N. Rescigno, Robert R. Lucchese, C. William McCurdy, and Arvinder Sandhu, "Probing autoionizing states of molecular oxygen with XUV transient absorption: Electronic-symmetry-dependent line shapes and laser-induced modifications." *Physical Review A* **95**, 043427(2017), as in Ref. [141].)

4.1 Introduction

The interaction of extreme ultraviolet (XUV) radiation with small molecules results in the formation of highly excited molecular states that evolve on ultrafast timescales and govern the dynamics of many physical and chemical phenomena observed in nature [142, 143]. In particular, single excitations of valence or inner valence electrons to Rydberg molecular orbitals forms neutral states that lie above the ionization threshold (sometimes called "superexcited" states) [144]. These states can lie energetically above several of the excited states of the molecular ion into which they can decay through autoionization [145]. Another feature of these autoionizing states is strong state-mixing and coupled electronic and nuclear motions, which can result in fast dissociation into excited neutral fragments [146]. The motivation for investigation of these states is quite wide ranging, from better understanding of the solar radiation induced photochemistry of planetary atmospheres [147] to the ultraviolet radiation damage in biological systems [148]. Furthermore, these are the states whose dynamics provide a mechanism for dissociative recombination of electrons with molecular ions, which has been the subject of decades of research [149–154]. Due to their importance in complex processes, the direct observation of the electronic and nuclear dynamics of these states has been a topic of intense interest in

molecular physics.

Advances in ultrafast technology such as laser high-harmonic generation (HHG) have enabled femtosecond (10^{-15} s) and attosecond (10^{-18} s) light pulses in the energy range of 10-100's eV [155, 156]. These ultrashort and broadband XUV bursts provide a way to coherently prepare, probe, and control ultrafast dynamics of highly excited molecules [157, 158]. Combined with time-delayed near infrared (NIR) or visible laser pulses, pump-probe spectroscopy schemes can be used to investigate dynamics in atoms and molecules on the natural timescale of electrons.

To characterize excited state dynamics, researchers have developed sophisticated techniques involving the detection of charged photofragments, and the measurement of the photoabsorption signals. In particular, attosecond transient absorption spectroscopy (ATAS) has received considerable attention recently [159, 160], as it is relatively easy to implement and quite suitable for the measurement and manipulation of bound and quasi-bound state dynamics. Recent ATAS experiments focus on properties and evolution of XUV initiated dipole polarization in atoms by using a delayed NIR pulse as a perturbation. In this scenario, many interesting time-dependent phenomena have been observed, including AC Stark shifts [161], light-induced states [162], quantum beats or quantum path interferences [163], strong-field line shape control [70], and resonant-pulse-propagation induced XUV pulse reshaping effects [64, 89].

In contrast to the bulk of previous studies, which have been conducted in atoms, our goal in this paper is to extend the ATAS to the investigation of complex molecular systems. Molecular ATAS is a largely unexplored topic and very few studies have been conducted so far [164, 165]. Here we present a joint experimental-theoretical study of the autoionizing Rydberg states of O_2. An XUV attosecond pulse train was used to coherently prepare the molecular polarization, and a time-delayed NIR pulse to perturb its evolution. Superexcited states created by the XUV pulse have multiple competing decay channels, including autoionization and dissociation into charged or neutral fragments. The autoionization process is one of the most fundamental process driven by electron correlation, which involves interference between

the bound and continuum channels. This discrete-continuum interaction is ubiquitous in atoms, molecules and nano-materials [166], and it is parametrized by the well-known Fano formula describing spectral line shapes [167].

The paper is organized as follows. Sec. 4.2 below introduces the autoionizing Rydberg states of O_2 and compares the photoabsorption cross sections obtained by different methods, including our time-independent Schwinger variational calculations. In Sec. 4.3, we describe our experimental setup and transient absorption line shapes obtained at various time delays. Section 4.4 is focused on the theoretical approach, where we describe our time-independent Schwinger calculation method in subsection 4.4.1, and the *ab initio* MultiConfiguration Time-Dependent Hartree-Fock (MCTDHF) method in subsection 4.7. We then compare full experimental transient absorption spectrograms with MCTDHF calculations in subsection 4.4.3. In Sec. 4.5, we present a simple model that connects Fano q parameters of static absorption profiles with the transient absorption line shapes and compares how laser induced attenuation (LIA) and laser induced phase (LIP) modifies the dipole polarization initiated by the XUV pulse. We summarize our work in Section 4.6, followed by appendices that describe experimental details, MCTDHF approach, and few-level model of dipole polarization and NIR perturbation.

4.2 Autoionizing Rydberg states in O_2

Table 4.1: State assignment, effective quantum number n^*, energy, linewidth and field-free lifetime of some relevant autoionizing states in O_2 from [9, 10]. Fano q parameters are obtained by fitting calculated photoabsorption cross section in Fig. 4.1(b).

State	n^*	**Energy (eV)**	**Linewidth (meV)**	**Lifetime (fs)**	**Fano q**
$6s\sigma_g$	$\sim$5	24.028	3.69	178.37	-0.60
$5d\sigma_g$		23.976	3.60	182.83	0.28
$5s\sigma_g$	$\sim$4	23.733	7.31	90.04	-0.59
$4d\sigma_g$		23.632	7.10	92.70	0.22

In our experiment, autoionizing Rydberg states with electronic configurations

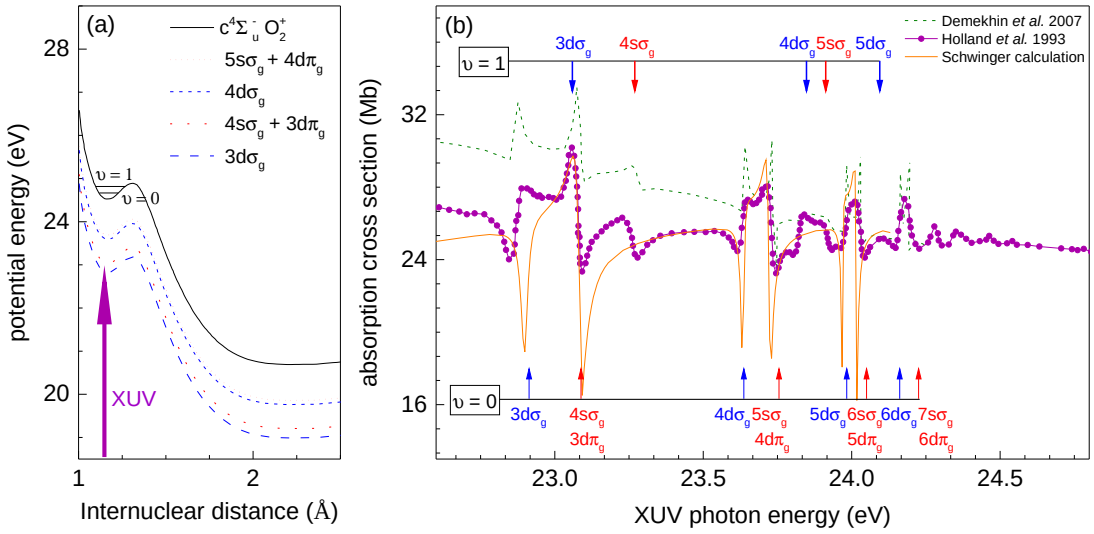

Figure 4.1: (Color online) (a) Schematic potential energy diagram of O_2. Black curve is the excited ionic c-state ($c^4\Sigma_u^-$). Blue dashed and red dottedcurves are Rydberg series of neutral superexcited *nd* and *ns* states, respectively. Each state supports two vibrational levels. (b) (Purple line) Synchrotron measurement of photoabsorption cross section from [9]. Features associated with various electronic states and their vibrational levels (ν=0 at bottom and ν=1 at top) are labeled. (Green dash line) Theoretical photoabsorption cross section from [10]. (Orange solid curve) Multi-channel photoabsorption cross section that we obtained using Schwinger variational calculation.

that we can denote as $2s\sigma_u^{-1}(\ c^4\Sigma_u^-)nl\sigma_g$, for example, are formed through the direct XUV excitation of an inner shell $2s\sigma_u$ electron to the Rydberg series converging to the excited ionic c-state ($c^4\Sigma_u^-$) of O_2^+. Fig. 4.1(a) shows the potential energy curves of some of these states. Those states that are optically connected to the $^3\Sigma_g^-$ ground state of O_2 have the symmetries $^3\Sigma_u^-$ and $^3\Pi_u$. In our observations, those Rydberg series correspond to excitations from the $2s\sigma_u$ orbital of O_2 to $nd\sigma_g$ ($^3\Sigma_u^-$), $ns\sigma_g$ ($^3\Sigma_u^-$), and $nd\pi_g$ ($^3\Pi_u$). The XUV pulse in the experiment can also cause direct excitation to the $^3\Sigma_u^-$ and $^3\Pi_u$ continua by photoionization of the $3\sigma_g$, $1\pi_u$, and $1\pi_g$ valence shells. Those excitations form the $X^2\Pi_g$, $a^4\Pi_u$, $A^2\Pi_u$ $b^4\Sigma_g^-$, $B^2\Sigma_g^-$ states of the ion, lying below the c-state of O_2^+ [168], and also a second $^2\Pi_u$ state at 23.9 eV just below the ground vibrational level of the c-state at 24.564 eV [169].

Therefore, the autoionizing Rydberg states converging to the c-state are each embedded in several ionization continua, and can decay into any of them. These autoionizing Rydberg states can be grouped into pairs of dominant features [ndσ_g, (n+1)sσ_g] shown in Fig. 4.1(a) as blue and red curves, respectively. As we discuss later the (n+1)sσ_g series overlaps with the ndπ_g series, therefore, to be accurate, the pairs of features in Fig. 4.1(a) should be listed as [ndσ_g, (n+1)sσ_g+ndπ_g]. The pairs relevant to our study are [3dσ_g, 4sσ_g+3dπ_g], [4dσ_g, 5sσ_g+4dπ_g], [5dσ_g, 6sσ_g+5dπ_g], [6dσ_g, 7sσ_g+6dπ_g], etc. Furthermore, the ionic c-state supports two vibrational levels [170], ν=0 and ν=1, as shown in Fig. 4.1(a), and the nlσ_g Rydberg states are also known to support at least two vibrational levels.

The pairs of Rydberg features [ndσ_g, (n+1)sσ_g+ndπ_g] can be identified in the static XUV photoabsorption spectra in Fig. 4.1(b), where the purple curve is static absorption spectrum adapted from a synchrotron study by Holland *et al.* [9]. The autoionizing Rydberg series with vibrational state ν=0 are labeled at the bottom of Fig. 4.1(b)(blue and red labels for each pair), while the members of the series with vibrational state ν=1 are labeled at the top. The green curve in Fig. 4.1(b) shows the theoretical cross section computed by Demekhin *et al.* [10] using a single center expansion method that includes static and non-local exchange interactions without coupling between ionization channels leading to different ion states. These authors estimated the ν=1 contributions and broadened their theoretical cross sections by a Gaussian function of 20 meV full width at half maximum (FWHM).

Using the Schwinger variational method in calculations described in Sec. 4.4.1, we computed the XUV photoionization cross section at the equilibrium internuclear distance of O_2 to approximate the vibrational ground state ν=0 contribution. Our results in Fig. 4.1(b)(orange curve) reproduce the main features of synchrotron measurements very well. Our calculated cross section curve is for randomly oriented molecules and includes both perpendicular ($^3\Pi_u$) and parallel ($^3\Sigma_u^-$) contributions from various ionization channels corresponding to continua associated with different ionic states. From the calculated static absorption line shapes (orange curve), we extracted Fano q parameters for a few representative states, which are listed in

Table 4.1. The autoionization lifetimes for these states (based on Ref. [10]) are also listed in Table 4.1.

4.3 Transient Absorption Experiment

To explore the dynamics of O_2 superexcited states, we conducted experimental and theoretical ATAS studies. Our experimental pump-probe setup is shown in Fig. 4.2(a). Briefly, we employ 40 fs NIR pulses at 1 kHz repetition rate with pulse energy 2 mJ and central wavelength 780 nm. One portion of the NIR beam is focused into a xenon filled hollow-core waveguide to generate XUV attosecond pulse trains (APTs) with ∼440 attosecond bursts and ∼4 fs envelope. The APTs is dominated by harmonics 13, 15, and 17, out of which the 15th harmonic resonantly populates superexcited states. The second portion of NIR laser pulse goes through a delay-line and perturbs the XUV initiated molecular polarization with estimated peak intensity ∼1 TW/cm^2. A grating spectrometer is used to measured the XUV spectra transmitted through the O_2 gas sample. Using the Beer-Lambert law we can determine optical density change (OD) due to NIR perturbation as a function of photon energy, $\hbar\omega$, and XUV-NIR time delay, t_d, as

$$OD(\omega, t_d) = -\log[(I_{out}^{\text{XUV+NIR}})/(I_{out}^{\text{XUV}})], \tag{4.1}$$

$I_{out}^{\text{XUV+NIR}}(\omega, t_d)$ and $I_{out}^{\text{XUV}}(\omega, t_d)$ are transmitted XUV spectra with and without the presence of NIR pulse, respectively.

The spectrogram measured using ATAS is shown in Fig. 4.2(b). To highlight the NIR induced absorbance change relative to continuum absorption, Fourier high pass filter is used to remove slow variation of underlying spectral profile, as also used in [164, 171]. The vertical axis of the spectrogram refers to milli- optical density change (mOD). Negative time delay means XUV arrives at the oxygen sample first, i.e. the NIR perturbation is imposed after the XUV initiates molecular polarization. There are many interesting aspects of this spectrogram. The striking feature being that we observe alternating blue and red bands corresponding to negative and positive OD change relative to the O_2^+ continua absorption spectrum, respectively.

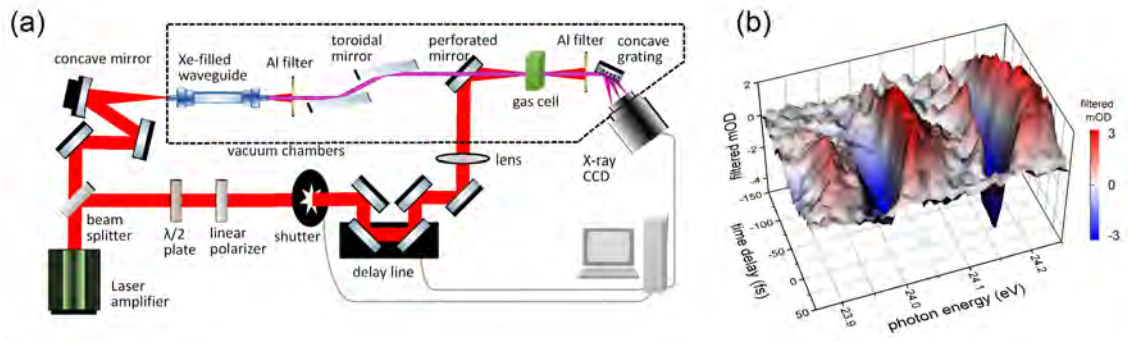

Figure 4.2: (Color online) (a) Experimental set up for XUV transient absorption studies in neutral superexcited states of O_2. (b) Experimentally measured transient absorption spectrogram in O_2.

According to the assignments of the autoionizing Rydberg states in Fig. 4.1(b), we find that all ndσ_g states show negative OD (less absorption compared to the continuum), while the features corresponding to the combination of nsσ_g and ndπ_g show positive OD.

We have plotted transient absorption spectra at some representative time delays in Fig. 4.3(a). The experimental input XUV spectrum is also plotted. Relevant state assignments are labeled on the top of the figure. In addition to ν=0 states, we also list ν=1 states, following assignments in Ref. [10]. In Fig. 4.3(a), for positive time delays, when the NIR pulse arrives earlier, there are no discernible features in the transient absorption spectrum, because the NIR pulse alone is not strong enough to significantly perturb the ground state of neutral O_2. At large negative delays where the XUV arrives earlier than the NIR, we observe finer oscillating structures corresponding to the well-known perturbed free induction decay [172]. When the delay is close to zero, complicated line shapes can be observed. These line shapes are more complex than Fano profiles observed in ATAS of atomic gases. Considering different pairs of features in the series, i.e. [4d, 5sσ_g + 4dπ_g], [5d, 6sσ_g+ 5dπ_g], etc, we find that all ndσ_g features show a dip in the transient absorption line shape at the position of the resonance, while (n+1)sσ_g+ndπ_g show a peak. The difference in signs of OD for these features stems from the difference in Fano q parameters of the static absorption profiles of the corresponding states which are shown in Fig. 4.1(b)

and discussed in more detail below.

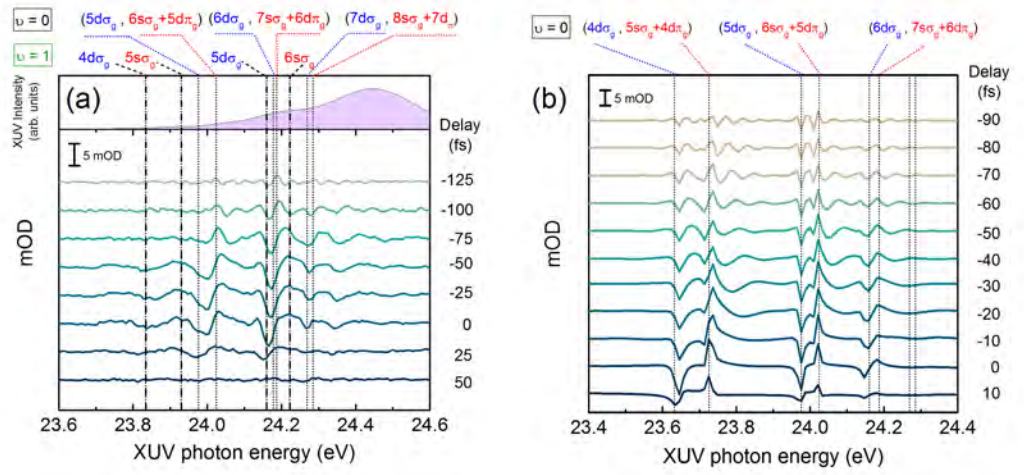

Figure 4.3: (Color online) (a) Experimental transient absorption spectra at certain representative time delays. The scale bar represents 5 mOD change. Experimental XUV spectrum is also shown at the top. Negative time delay implies XUV arrives at the target earlier than NIR pulse. All ndσ_g (nsσ_g+ndπ_g) states show negative (positive) OD at resonance, corresponding to less (more) absorption compared to continua absorption spectrum. (b) The MCTDHF calculations of the transient absorption spectra at few time delays.

4.4 Transient Absorption Theory

4.4.1 Time-independent calculations

Since the static XUV photoabsorption line shapes play a central role in our interpretation of the transient absorption spectra, we calculated the XUV photoionization cross section using the Schwinger variational approach [173, 174]. Briefly, the one-electron molecular orbitals in these calculations were expanded by using an augmented correlation-consistent polarized valence triple zeta aug-cc-pVTZ basis set [175, 176]. A valence complete active space self-consistent field calculation on the ground state of O_2 was used to obtain a set of orbitals that was then used in complete active space configuration interaction (CAS-CI) calculations on both the O_2 ground state and the O_2^+ states. The six channels that were included consisted

of five channels which are open in the energy range of interest in this study, 23.6 eV to 24.4 eV, $X\ ^2\Pi_g$, $a\ ^4\Pi_u$, $A\ ^2\Pi_u$, $b\ ^4\Sigma_g^-$, and $B\ ^2\Sigma_g^-$. The sixth channel, which was closed, is the $c^4\Sigma_u^-$ channel that is responsible for the autoionization resonances studied here. In all calculations, the ionization potentials were shifted slightly to agree with the experimental vertical ionization potentials in Ref. [169].

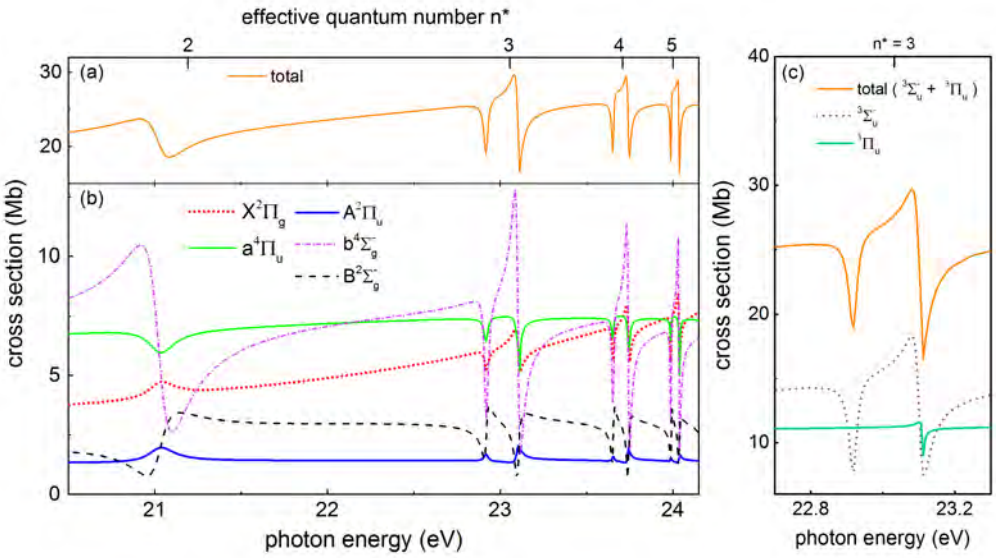

Figure 4.4: (Color online) (a) Total cross section as a function of the photon energy and effective quantum number n*. (b) Various electronic channels contributing the total cross sections and their Fano profiles. (c) Parallel ($^3\Sigma_u^-$) and perpendicular ($^3\Pi_u$) polarization contributions to the total XUV photoionization cross section in the vicinity of the pair of features with n*= 3 in Fig. 4.1 showing the presence of the $3d\sigma_g$(parallel), $4s\sigma_g$ (parallel), and $3d\pi_g$ (perpendicular) states.

In Fig. 4.4(a), we plot the total cross section as a function of photon energy and as a function of the effective quantum number, defined as $n^* = \sqrt{R_y/(\mathrm{IP} - \hbar\omega)}$, where R_y is the Rydberg constant and IP is the ionization potential of the closed $c^4\Sigma_u^-$ channel which has the autoionizing resonances. The partial cross sections computed for ionization leading to the five open channels are shown in Fig. 4.4 (b), which shows the autoionization resonances coming from the closed channel. We neglected two states that are observed in the photoelectron spectrum [169], the dissociative $^2\Pi_u$ state at 23.9 eV that has a broad photoelectron spectra and the weak $^2\Sigma_u^-$ channel at

27.3 eV. In addition, we have neglected a number of other experimentally unobserved states that would have very weak ionization cross sections in this energy region.

Fig. 4.4(b) shows that Fano q parameters depend on the final channel considered. However, a single resonance interacting with many continua can be rewritten as a resonance interacting with the linear combination of the channels. The orthogonal linear combinations of the channels do not interact with the resonance but contribute to a non-zero background to the cross section. Furthermore, by calculating the parallel ($^3\Sigma_u^-$) and perpendicular ($^3\Pi_u$) polarization contributions to the XUV photoionization cross section in Fig. 4.4(c), we clearly see that each of the pairs of features in Fig. 4.1 corresponds to three states that were mentioned in the Sec. 4.2. In each pair, the first feature corresponds to an ndσ_g Rydberg state while the second corresponds to contributions from the (n+1)sσ_g and ndπ_g states. The ndπ_g Rydberg series was proposed before by Wu *et al.* [177], but it has been ignored in many of the subsequent experimental and theoretical studies. Importantly, as seen from Fig. 4.4(c), Fano q parameters are similar for the two overlapping states (n+1)sσ_g and ndπ_g.

4.4.2 Time-dependent calculations

We performed *ab initio* theoretical calculation of transient absorption signals in the same energy range as O_2 superexcited states using a recently developed implementation of the MCTDHF method. This method simultaneously describes stable valence states, core-hole states, and the photoionization continua, which are involved in these transient absorption spectra, and this approach has been previously explored and developed by several groups [178–184]. Briefly, our implementation solves the time-dependent Schrödinger equation in full dimensionality, with all electrons active. It rigorously treats the ionization continua for both single and multiple ionization using complex exterior scaling. As more orbitals are included, the MCTDHF wave function formally converges to the exact many-electron solution, but here the limits of computational practicality were reached with the inclusion of full configuration interaction with nine time-dependent orbitals.

In these calculations, an isolated XUV attosecond pulse is used to excite the polarization which is then perturbed by a more intense NIR pulse. The weaker XUV probe pulse is modeled as an isolated 500 attosecond pulse with a $\sin^2$ envelope centered at 27.21 eV and with an intensity of 1.6×10^{10} W/cm^2. The 40 fs NIR pulse is centered at 800 nm with an intensity of 1.5×10^{12} W/cm^2. The MCTDHF calculation produces the many-electron wave function $|\Psi(t)\rangle$ both during and after the pulses.

To describe the resulting spectrum, we start from a familiar expression for the transient absorption spectrum. If the time-dependent Hamiltonian is written as $\hat{H} = \hat{H}_0 - \hat{d}\,\mathcal{E}(t)$ where $\hat{H}_0$ is the field-free Hamiltonian, $\hat{d}$ is the dipole operator, and $\mathcal{E}(t)$ is the electric field of the applied XUV and NIR laser pulses, the single-molecule absorption spectrum is proportional to the response function [185–187], namely,

$$\tilde{S}(\omega) = 2\mathrm{Im}[\tilde{d}(\omega)\,\tilde{\mathcal{E}}^*(\omega)] \tag{4.2}$$

In this equation, $\tilde{d}(\omega)$ and $\tilde{\mathcal{E}}(\omega)$ are the Fourier transform of the time-dependent induced dipole, $d(t) = \langle\Psi(t)|\hat{d}|\Psi(t)\rangle$, and the total applied electric field, $\mathcal{E}(t)$, respectively. We use response function in this study together with *ab initio* calculations of the electron dynamics to compute the transient absorption signals. Equation (4.2) is also the point of departure for our description of these spectra using the simple models described in Section 4.5. In both cases these spectra are used to compute the experimentally measured OD by employing the Beer-Lambert law as described in Appendix 4.7 where additional details of the MCTDHF calculations are given.

A number of previous calculations and experiments, for example, Refs. [10, 188–192], considered only parallel polarization between oxygen molecule internuclear axis and the XUV field, and thus invoked only two Rydberg series with ns$\sigma_g(^3\Sigma_u^-)$ (l=0, m=0) character and with $nd\sigma_g(^3\Pi_u)$ (l=2, m=0) character. In MCTDHF calculation, as in the Schwinger variational calculation, we have assumed randomly oriented molecules in the presence of a linearly polarized XUV field in the calculation. Here again therefore, in addition to Rydberg series corresponding to excitations form

$2s\sigma_u$ to $ns\sigma_g$ and $nd\sigma_g$ Rydberg orbitals, we rediscovered contributions from the third Rydberg series corresponding to excitations to orbitals $nd\pi_g$ (l=2, m=1) character, converging to the same limit and forming O_2 states of overall $^3\Pi_u$ symmetry.

Fig. 4.3(b) shows MCTHDF calculation of the transient absorption spectra at few representative time delays. It agrees well with experimental spectra in Fig. 4.3(a), and all $nd\sigma_g$ states show a dip in the transient absorption line shapes, while $(n+1)s\sigma_g$+$nd\pi_g$ states show a peak. Experimental line shapes exhibit more features than MCTDHF results due to the presence of transient absorption signals from an additional vibrational level (ν=1) for each state, and this possibility is not considered in the MCTDHF calculation.

4.4.3 Comparison of experimental and MCTDHF spectrograms

Next, we compare full experimental and calculated spectrograms as shown in Fig. 4.5(a) and (c), respectively. The MCTDHF calculation generally agrees with the experimental data very well, where they both show alternative positive (red) and negative (blue) absorbance structures at $(n+1)s\sigma_g$ (including $nd\pi_g$) and $nd\sigma_g$ states, respectively. Moreover, the upward curve of absorption structure indicates that there are AC Stark shifts of the quasibound states induced by moderate strong NIR laser field. The observed Stark shift $\sim$ 20 meV near zero delay corresponds well with the NIR laser peak intensity used. Also, hyperbolic fringes apparent at large negative time delays can be understood by the perturbed free induction decays, as also observed in ATAS studies in atomic gases. As mentioned earlier, experimental data contains contributions from ν=1 vibrational levels, therefore the experimental spectrogram has more features than the theoretical counterpart.

By taking line-outs from the spectrograms at the energy location of various Rydberg states, we can obtain information about the evolution of these states. In Fig. 4.5(b), we take line-outs at the energies corresponding to the 4d(ν=0), 5s(ν=0), 4d(ν=1), 5s(ν=1), 5d(ν=0), 6s(ν=0), 6d(ν=0), 5d(ν=1), 7s(ν=0), 6s(ν=1), 7d(ν=0), 8s(ν=0) states, in order of increasing energy, at the position of maximum positive or negative OD change. Note that the line-outs labeled $(n+1)s\sigma_g$ include

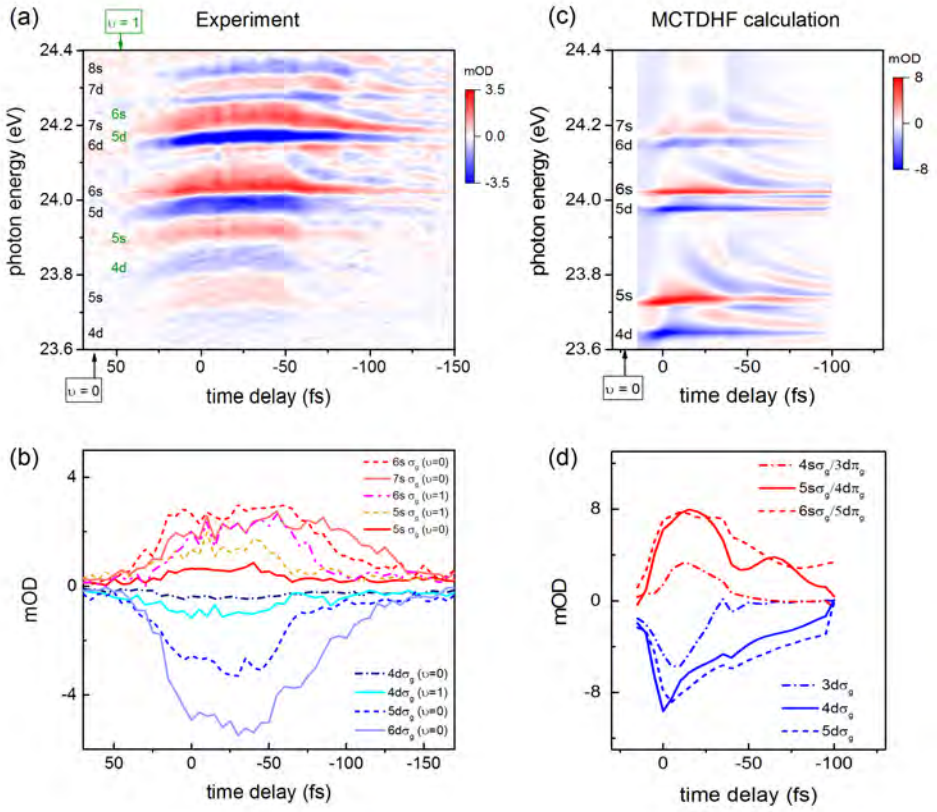

Figure 4.5: (Color online) (a) Measured transient absorption spectrogram labeled with various electronic states corresponding to ν=0 (black) and ν=1 (green) vibrational levels, and (b) its corresponding horizontal line-outs at some representative energy levels. (c) MCTDHF calculated transient absorption spectrogram, and (d) its corresponding horizontal line-outs.

contribution from ndπ_g. It is clear that regardless of the sign of the OD change the lifetime of polarization increases with the quantum number of the Rydberg series members. It is known that the natural autoionization lifetimes scale with effective quantum number as $(n^*)^3$ [193], and for each n, the (n+1)sσ_g, ndπ_g, and ndσ_g states have similar n^* values (see Fig. 4.4), and have similar decay timescales.

It should be noted that the decay timescales observed here are faster than the autoionization lifetimes due to NIR pulse induced broadening of resonances [194]. Fitting a convolution of Gaussian and exponential decay to the evolution of 5d, 6s (ν=0) signals, we obtain a decay timescale ~60 fs, corresponding to a net line width

of ∼11 meV. Subtracting the field-free natural line width of 3.6 meV (Table 4.1), we estimate the effective NIR induced broadening of these resonances to be ∼7 meV. The decay timescales for other ν=0 resonances are difficult to estimate as the transient absorption signals are either very weak or they overlap with vibrationally excited, nu=1 members of the Rydberg series. It is also hard to discern if decay timescales for ν=1 states are different from the ν=0 states. This is significant as the dissociation lifetime of ν=1 states are much shorter (∼67 fs) than ν=0 dissociation lifetime ($> ps$), and thus can be comparable to autoionization lifetime [195] over the range of the effective quantum numbers considered here. One could argue in this case that as the molecule breaks up into excited atomic fragments, the decay of atomic polarization follows similar trend as the original molecular polarization.

Fig. 4.5(d) shows MCTDHF calculation line-outs for certain ns(ν=0) and nd(ν=0) states, and the trends in their lifetimes qualitatively agree with experimental observations and expectations that the larger effective quantum number states have a longer autoionization lifetimes. However, our MCTDHF calculations are not able to accurately reproduce the absolute lifetimes of these states, particularly those with higher principal quantum number. It should be noted that unlike some recent studies on excited states of H_2 [196], our experiment-theory comparison shows that for Rydberg autoionizing states in O_2 neither nuclear vibration nor molecular rotation has a significant effect on the delay-dependent line shapes obtained in transient absorption spectra.

4.5 Few-level Models for Transient Absorption Spectra

Transient absorption line shapes carry information on about the XUV induced dipole polarization and its modification by an NIR pulse. For autoionizing states, we can use a few-level model to understand the origin of the correlation observed here between changes in the OD seen in transient absorption and Fano q parameters of the line shapes in the corresponding static XUV absorption spectrum. The central idea is to begin with a model for the polarization $d(t)$ induced by the XUV pulse

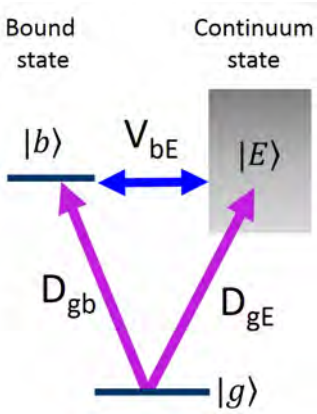

Figure 4.6: (Color online) Three level model system showing a ground state $|g\rangle$, an excited bound state $|b\rangle$, and a continuum state $|E\rangle$, along with dipole couplings D_{gb}, D_{gE}, and interaction term V_{bE}.

that is capable of reproducing the Fano line shapes of the XUV spectrum, and then allow the NIR pulse to modify it by either laser-induced attenuation or laser-induced phase shift. We then use the modified $d(t)$ characterized by the time delay t_d, namely, $d_{t_d}(t)$, to calculate the change of the response function of Eq. (4.2), i.e. $\tilde{S}(\omega, t_d) - \tilde{S}(\omega)$, and therefore the transient absorption spectrum.

In the model system, an XUV interaction directly couples the ground state, $|g\rangle$, to both an excited metastable quasibounded (autoionizing) state, $|b\rangle$, and the background continuum at nearby energies, $|E\rangle$. A schematic of the energy levels in our few-level model system is shown in Fig. 4.6. A similar treatment of autoionizing states using few-level model has been described in detail by Chu and Lin [187], and we generally follow their approach. For the diagram in Fig. 4.6, the time-dependent wave function of the system is a superposition of these states

$$\begin{aligned} \Psi(t) &= e^{-iE_g t} C_g(t)|g\rangle \\ &+ e^{-i(E_g+\omega_{\mathrm{XUV}})t}\left[C_b(t)|b\rangle + \int dE C_E(t)|E\rangle\right]. \end{aligned} \tag{4.3}$$

The time-dependent coefficients $C_g(t)$, $C_b(t)$, and $C_E(t)$ can be computed by solving the corresponding time-dependent Schrödinger equation in which the time-dependent Hamiltonian is

$$\hat{H}(t) = \hat{H}_0 - \hat{d}\left[\mathcal{E}_{\mathrm{XUV}}(t) + \mathcal{E}_{\mathrm{NIR}}(t; t_d)\right], \tag{4.4}$$

where $\hat{H}_0$ is the unperturbed molecular Hamiltonian and $\hat{d}$ is the dipole operator. The XUV field, $\mathcal{E}_{\text{XUV}}(t)$ is centered at $t = 0$, and the delayed NIR field is centered at $t = t_d$, so that

$$\mathcal{E}_{\text{NIR}}(t; t_d) = \mathcal{E}^0_{\text{NIR}} e^{-(t-t_d)^2/\tau^2_{\text{NIR}}} e^{i\omega_L(t-t_d)} + c.c., \tag{4.5}$$

where $\mathcal{E}^0_{\text{NIR}}$ is the NIR peak field amplitude, and $\hbar\omega_L$ is the NIR photon energy.

We first consider the case with XUV pulse alone to verify that this simple treatment with two discrete levels and a background continuum can describe the Fano profiles of autoionizing states. The ultrashort XUV field creates a polarization, $d(t)$, at the beginning of the XUV pulse,

$$d(t) = \langle \Psi(t) | \hat{d} | \Psi(t) \rangle. \tag{4.6}$$

We can solve for $|\Psi(t)\rangle$ and construct an analytic expression for $d(t)$ under the assumptions explained in Appendix 4.8. We generalize the delta function XUV pulse used in [187] to have a Gaussian shape instead, with envelope function $F(t)$ and electric field amplitude F_{XUV}.

$$\begin{aligned} \mathcal{E}_{\text{XUV}}(t) &= F(t) \exp\left(i\omega_{\text{XUV}} t\right) + c.c. \\ F(t) &\equiv F_{\text{XUV}}\ e^{-(t/\tau_{\text{XUV}})^2} / \sqrt{\pi \tau^2_{\text{XUV}}} \end{aligned} \tag{4.7}$$

The analytical expression for $d(t)$ due to this XUV pulse is given in the appendix in Eq.(4.26). In our model calculations, the XUV pulse width τ_{XUV} is 5 femtosecond. In the limit that the XUV pulse is infinitely narrow ($\tau_{\text{XUV}} \to 0$) this pulse becomes a delta function pulse as used in [187].

In that limit this model produces precisely the Fano line shape of an absorption feature corresponding to the bound state, $|b\rangle$ embedded in the continuum as shown in Eq.(4.22). Thus, our point of departure for the simple models for how the line shapes of the pure XUV spectrum are modified by transient absorption is the assumption that the NIR pulse arriving at time delay t_d modifies the form of $d(t)$ initiated by the XUV pulse. In these models, the decay lifetimes and Fano q parameters are chosen so that the simulated frequency-domain static line shapes in Fig. 4.7(a) for (5d,6s) states agree with our static photoabsorption cross section data in Fig. 4.1(b).

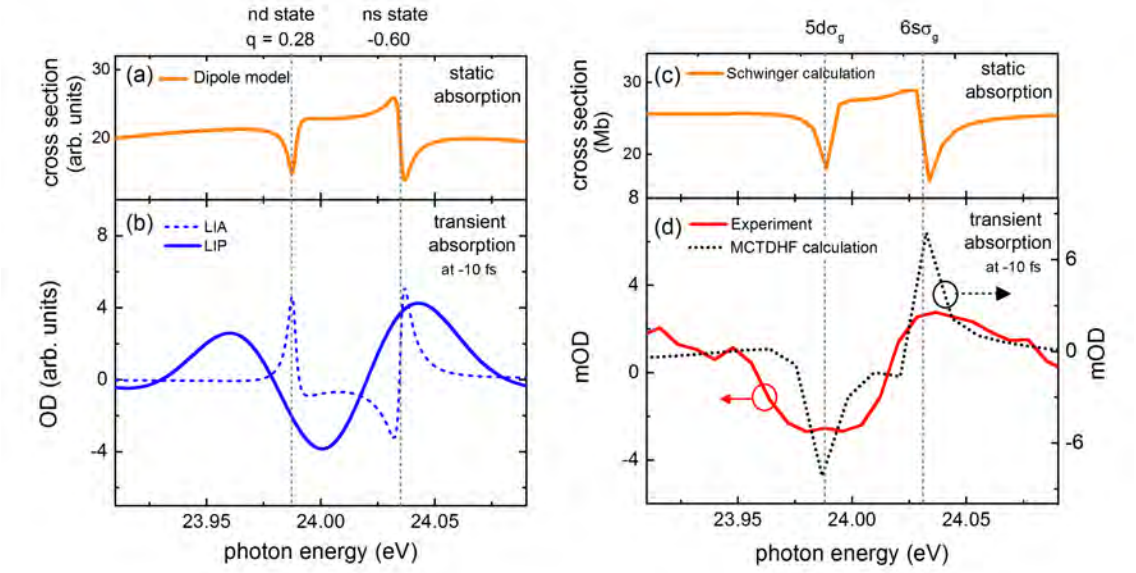

Figure 4.7: (Color online) Modeling of transient absorption line shapes resulting from the NIR perturbation. (a) Simulated static absorption profile that mimics the 5d and 6s state line shapes and the corresponding Fano q parameters. (b) Transient absorption spectra obtained when NIR perturbation is modeled as laser induced phase (LIP) and laser induced attenuation (LIA). (c) Calculated static absorption spectrum for 5d and 6s states based on Schwinger variational approach from Fig 4.1(b) for comparison. (d) Experimentally measured transient absorption spectrum (solid red line) , and MCTDHF calculated transient absorption spectrum (dashed black line) from Fig 4.3(b) for comparison.

To model the NIR perturbation of XUV induced polarizations in the atomic case, two approaches are widely used: the laser-induced attenuation (LIA) model and laser-induced phase (LIP) model. The key assumption of the LIA model is that the intense NIR pulse extinguishes the polarization initiated by the XUV pulse by truncating the oscillating electric dipole. Its physical meaning is that the quasibound state population is depleted by the NIR pulse through transfer to other states and continua. In the sudden version of this approximation, the polarization can be expressed as

$$d_{t_d}(t) = \begin{cases} d(t) & , t < t_d \\ 0 & , t \geq t_d \end{cases} \qquad \text{LIA model.} \tag{4.8}$$

A slower truncation can also be applied by using a smoother function for transition between two regimes. The LIA approach is central to a number of models for ATAS studies in many atomic gases [187, 197–199].

On the other hand, the LIP model assumes that NIR field leads to an energy modification, $\Delta E(t, t_d)$, of the excited state, and hence the polarization will gain additional phase such that

$$d_{t_d}(t; t_d) = d(t)e^{i\phi(t,t_d)} \quad \text{LIP model}, \tag{4.9}$$

where the additional phase is $\phi(t, t_d) = \Delta E(t, t_d)t/\hbar$, and it depends on the delay time t_d of the NIR pulse. The LIP model has been used to explain results of ATAS in many atomic cases [70, 71, 161, 172].

Two methods can be used to calculate the energy and hence phase shift $\phi(t; t_d)$. Refs. [70, 71] calculate it based on the Stark energy shift, which is time-averaged and approximated as a pondermotive energy shift. Alternately, second-order perturbation theory can be used to calculate the energy shift in the presence of coupling to nearby states [161]. Here we took the former approach for the phase shift calculation, and parameterized the pondermotive energy shift in atomic units as

$$E_{\text{pon}}(t; t_d) = [\mathcal{E}^0_{\text{NIR}} e^{-(t-t_d)^2/\tau^2_{\text{NIR}}}]^2/(4\omega_L^2). \tag{4.10}$$

Thus, the NIR modified dipole polarization becomes

$$d_{t_d}(t; t_d) = d(t)e^{iE_{\text{pon}}(t;t_d)\,t}. \tag{4.11}$$

Using either the LIP or LIA model, we Fourier transformed the modified polarization and calculated the response function using Eq.(4.2), thereby obtaining the OD as a function of energy and delay using Eq.(4.13). Further details of our model calculations are given in Appendix 4.8.

In the LIA model, we use smooth truncation of the XUV initiated polarization, which results in the absorption spectrum shown as dashed blue line of Fig. 4.7(b) (at delay -10 fs). In this model, the absorption at resonance energy increases or decreases depending on whether the absolute value of the Fano q parameter of the

static line shape is either less than or greater than unity, similar to the behavior for a sudden truncation case exhibited explicitly in Eq. (4.32). The Fano q parameters of the pairs of autoionizing features in static absorption spectrum (Fig. 4.1(b)) both have $|q| < 1$, but with differing signs, and thus the LIA model, even with gradual attenuation, fails to reproduce the directions of absorption changes observed in the transient absorption spectrum.

Using Fano q parameters from the static absorption profile in Fig. 4.7(a) and our experimental NIR pulse parameters, we also applied the LIP model with pondermotive energy shift as a NIR perturbation effect, and results are shown in solid blue line in Fig. 4.7(b). The application of a laser induced phase evidently produces an effect in which the absorption increases or decreases depending on the *sign* of q when $|q| < 1$. For comparison of our model with full theory and the experiment, we show static absorption line shapes obtained using Schwinger calculation in Fig. 4.7(c). Figure 4.7(d) shows the transient absorption line shapes obtained experimentally (solid red line) and from MCTDHF calculation (solid black line) at delay of -10 fs. Both our experimental and MCTDHF calculated line shapes agree well with the LIP model. It is important to note that the detailed measurements of complex line shapes associated with molecular polarization of pairs of nd and ns states provide the required detail to distinguish between the validity of different models. To our knowledge, this is the first study where such comparison has been made. Based on our results, it seems that in this case the LIP assumptions better reflect the physics of ATAS experiment than those of the LIA model, even with smooth attenuation functions.

4.6 Conclusion

In summary, we used the ATAS to investigate XUV initiated oxygen molecular polarization of superexcited states, perturbed by a NIR pulse, and the alternate negative and positive absorption spectra for ndσ_g and (n+1)sσ_g autoionizing states are observed. The numerical results obtained using *ab initio* MCTDHF calculations agree

with the experimental findings. In addition, from our MCTDHF and Schwinger variational calculations, we identify and include the contribution of a weaker ndπ_g state that overlaps with (n+1)sσ_g state. From the transient absorption spectrograms, we observe that decay lifetime of the dipole polarization for ndσ_g and (n+1)sσ_g states is similar and it increases with the effective quantum number n*. However, the decay timescale is faster than natural autoionization timescale due to NIR pulse induced broadening of resonances. The decay lifetime is also found to be insensitive to the vibrational state of the molecule, within the sensitivity of our measurements. To better interpret our findings, two models of NIR perturbation of the XUV initiated molecular polarization are tested against experimental and MCTDHF calculated transient absorption line profiles, and we find that laser induced phase shift model explains our results, while laser induced attenuation does not. On these grounds, we conclude that the negative/positive transient absorption signals for nd/ns states can be explained in terms of two very different manifestations of electronic interference in molecular excitation (opposite signs of initial Fano q parameters) influenced by the same NIR induced Stark shift in transient absorption experiments. We envision that additional ATAS investigations of low quantum number Rydberg states that do not follow core-ion approximation [191], with few-cycle NIR pulses, will enable us to study the non-adiabatic effects associated with fast autoionization and dissociation in O_2. The relationship between the static properties and transient absorption line shapes explored here leads us to propose that finer features of ATAS spectra in molecules could be used to characterize the undetermined electronic properties of dynamically evolving systems and test the theoretical models of the strong-field modification of the correlated electron dynamics, including recently proposed interference stabilization of autoionizing states [200].

4.7 Appendix I: MCTDHF Based Theoretical Calculations

To calculate the transient absorption spectra, we applied the MCTDHF method, which simultaneously describes stable valence states, core-hole states, and the

photoionization continuua. MCTDHF implementation solves the time-dependent Schrödingier equation in full dimensionality, and because it is based on a combination of the discrete variable representation (DVR) and exterior complex scaling (ECS) of the electronic coordinates, it rigorously treats the ionization continua for both single and multiple ionization. As more orbitals are included, the MCTDHF wave function formally converges to the exact many-electron solution. The MCTDHF electronic wave function is described by an expansion in terms of time-dependent Slater determinants, $|\Psi(t)\rangle = \sum_a A_a(t)|\vec{n}_a(t)\rangle$, in which each determinant is the anti-symmetrized product of N spin orbitals, $|\vec{n}_\alpha(t)\rangle = \mathscr{A}\left(|\phi_{a1}(t)\rangle \cdots |\phi_{aN}(t)\rangle\right)$. These spin-restricted orbitals $|\phi_a(t)\rangle$ are in turn expanded in a set of time dependent discrete DVR basis functions, and full configuration interaction is employed within the electronic space. We reach the MCTDHF working equations by applying the Dirac-Frenkel variational principle to the time-dependent Schrödinger equation for the trial function. Details of the resulting working equations and their solution can be found in Ref. [201].

The results presented here were calculated using nine orbitals, which can be labeled as $\sigma_g,\ \sigma_g,\ \sigma_u,\ \sigma_u\ ,\pi_{u,\pm1},\ \sigma_g,\ \pi_{g,\pm1}$ at the beginning of the propagation. These calculations have a spin adapted triplet configuration space of dimension 36. We used a fixed nuclei Hamiltonian where the internuclear distance is 2.282 bohr. Prolate spheroidal coordinates, (η, ξ, ϕ), were used in these calculations, and we employ a DVR grid of 10 points for η and a ξ grid with twelve grid points per finite element. Nine finite elements were used in ξ, the first of length 2.0 a_0 providing a dense grid to represent the 1s orbital and orbital cusp region, with seven subsequent five elements of length 8.0 a_0. Exterior complex scaling is applied to the remaining four elements extending an additional 32 a_0 with a complex scaling angle of 0.40 radians. The results show no sensitivity to the ECS angle, indicating that all ionized flux is being completely absorbed by the ECS procedure.

The MCTDHF calculation describes the relative energies and line shapes in these cross section, but does not reproduce the absolute excitation energies of these autoionizing states. Thus, the calculated results were shifted to lower energies by

5.18 eV such that the limit of the calculated Rydberg series, corresponds to the $c^4\Sigma_u^-$ state of O_2^+, agrees with the literature value. Because the present calculations used a fixed nuclei treatment, the MCTDHF computed cross section does not exhibit vibrational structure. We observe that the relative energies of the $(2\sigma_u)^{-1}(ns\sigma_g)$ and $(2\sigma_u)^{-1}(nd\sigma_g)$ series from our fixed-nuclei MCTDHF calculations agree well with the locations of first vibrational states (ν=0) of those two series as in [9, 10].

The MCTDHF computed cross section is for randomly oriented molecules in the presence of a linearly polarized XUV field. This total cross section is computed using the appropriate relation for single photon absorption, $\sigma_{\text{total}} = \frac{1}{3}\sigma_{\parallel} + \frac{2}{3}\sigma_{\perp}$, where $\sigma_{\parallel}$ and $\sigma_{\perp}$ are calculated separately for oriented molecules either parallel or perpendicular to the polarization directions of the fields. The calculations from Demekhin *et al.* [10], considered only parallel polarization, and thus there were only two Rydberg series, $(2\sigma_u)^{-1}(ns\sigma_g)$ and $(2\sigma_u)^{-1}(nd\sigma_g)$, converging to the $c^4\Sigma_u^-$ limit. However, using perpendicular polarization, the MCTDHF computed $\sigma_{\perp}$ exhibits a third Rydberg series converging to the same limit, namely, the series we have identified as $(2\sigma_u)^{-1}(nd\pi_g)$ here.

To compute quantities directly comparable to the experimental observation of the quantity in Eq.(4.1), we begin with Beer-Lambert law, $-\log[I_{\text{out}}/I_{\text{in}}] = \sigma\, N\, L$ where I_{in} and I_{out} are the incoming and outgoing field intensities, respectively, and σ is the photoabsorption cross section. For these comparisons, we estimated the molecular density as $N = 1 \times 10^{16}\text{cm}^{-3}$ and $L = 1$ cm for the path length. The photoabsorption cross section is related to the response functions, $\tilde{S}(\omega)$, computed using the MCTDHF method. Therefore, we can construct the appropriate OD corresponding to Eq.(4.1) as

$$\begin{aligned}
\text{OD} &= -\log\left[\frac{I_{\text{out}}^{\text{XUV+NIR}}(t_d)}{I_{\text{out}}^{\text{XUV}}}\right] \\
&= -\left\{\log\left[\frac{I_{\text{out}}^{\text{XUV+NIR}}(t_d)}{I_{\text{in}}^{\text{XUV+NIR}}}\right] - \log\left[\frac{I_{\text{out}}^{\text{XUV}}}{I_{\text{in}}^{\text{XUV}}}\right]\right\} \\
&= 4\pi\alpha\omega\left[\frac{\tilde{S}_{\text{XUV+NIR}}(\omega;t_d)}{|\tilde{\mathcal{E}}_{\text{in}}^{\text{XUV+NIR}}(\omega)|^2} - \frac{\tilde{S}_{\text{XUV}}(\omega)}{|\tilde{\mathcal{E}}_{\text{in}}^{\text{XUV}}(\omega)|^2}\right]NL
\end{aligned} \tag{4.12}$$

At frequencies in the XUV, the contribution of the NIR pulse is negligible, so

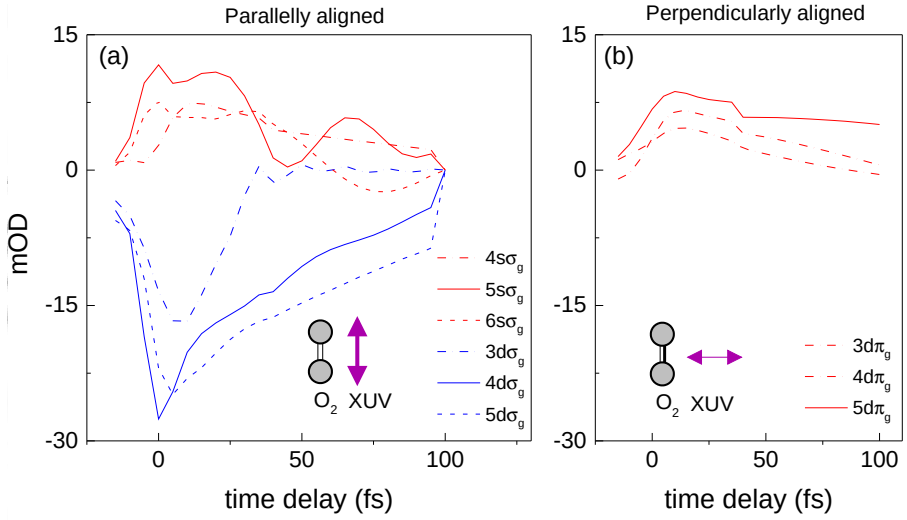

Figure 4.8: (Color online) Transient absorption line-outs calculated using MCTDHF method for molecules (a) aligned parallel to XUV field polarization, and (b) perpendicularly to XUV field polarization, plotted at the energies corresponding to several resonances. Note that the NIR field polarization is always parallel to the XUV field polarization.

that $\tilde{\mathcal{E}}_{\rm in}^{\rm XUV+NIR}(\omega) \approx \tilde{\mathcal{E}}_{\rm in}^{\rm XUV}(\omega)$. With that assumption, Eq.(4.12) becomes the following working expression for the measured quantity in terms of the calculated frequency- and delay-dependent response functions,

$$\mathrm{OD} \approx 4\pi\alpha\omega \frac{\left[\tilde{S}_{\rm XUV+NIR}(\omega;t_d) - \tilde{S}_{\rm XUV}(\omega)\right]}{|\tilde{\mathcal{E}}_{\rm in}^{\rm XUV}(\omega)|^2} NL. \tag{4.13}$$

When the molecular axis of O_2 is parallel to both XUV and NIR field polarization directions as in Fig. 4.8 (a), the ndσ_g states exhibit negative OD, while nsσ_g states show positive OD. However, as shown in Fig. 4.8 (b), where the molecular axis is perpendicular to the polarization directions of both XUV and NIR fields, the ndπ_g states contribute positive OD. In order to compute the time-delay dependent OD for randomly oriented molecules, we make the approximation (exact for one-photon absorption), $\mathrm{OD}_{\rm total} = \frac{1}{3}\mathrm{OD}_{\parallel} + \frac{2}{3}\mathrm{OD}_{\perp}$, and the result is shown in Fig. 4.3 (b) and Fig. 4.5 (d). Specifically, in Fig. 4.5 (d) we show OD at six energies which correspond to three resonances for the $(2\sigma_u)^{-1}$ndσ_g series, and three resonances for the $(2\sigma_u)^{-1}$(ndπ_g)+$(2\sigma_u)^{-1}$(nsσ_g) series.

4.8 Appendix II: Few-level Model for Transient Absorption

4.8.1 XUV initiated polarization

We first substitute Eq.(4.3) and the Hamiltonian in Eq.(4.4) into the Schrödinger equation, and then project onto that equation with $\langle g|$, $\langle b|$, and $\langle E|$. We then assume that the only nonzero dipole matrix elements are $D_{gb} = \langle g|\hat{d}|b\rangle$ and $D_{gE} = \langle g|\hat{d}|E\rangle$, and recalling that the XUV field is $\mathcal{E}_{\text{XUV}}(t) = F(t)e^{i\omega_{\text{XUV}}t} + c.c.$, make the rotating wave approximation. We also assume that the molecular Hamiltonian, H_0, couples only $|b\rangle$ to $|E\rangle$, so that its only nonzero matrix elements are $E_g = \langle g|H_0|g\rangle$, $E_b = \langle b|H_0|b\rangle$, $\langle E|H_0|E'\rangle = \delta(E-E')$, and $V_{bE} = \langle b|H_0|E\rangle$. Then, using the orthogonality of $|g\rangle$, $|b\rangle$, and $|E\rangle$, we find that the time-dependent coefficients $C_g(t)$, $C_b(t)$, and $C_E(t)$ satisfy the coupled differential equations,

$$
\begin{aligned}
i\dot{C}_g &= -\left[\int dE\ D_{gE}C_E F(t) + D_{gb}C_b F(t)\right], && (4.14)\\
i\dot{C}_b &= [E_b - (E_g + \omega_{\text{XUV}})]C_b \\
&+ \int dE\ V_{bE}C_E - D^*_{gb}C_g F(t)^*, && (4.15)\\
i\dot{C}_E &= [E - (E_g + \omega_{\text{XUV}})]C_E \\
&+ V_{Eb}C_b - D_{Eg}C_g F(t)^*. && (4.16)
\end{aligned}
$$

We also adopt the adiabatic elimination of the continuum by assuming that the coefficients of the continuum states change much more slowly than those of the discrete states, i.e., $\dot{C}_E \approx 0$, as was done in Ref. [187]. The equation for the time-dependent coefficients for the continuum states, $C_E(t)$, can thus be simplified to give

$$C_E = -\frac{V_{Eb}C_b - D_{Eg}C_g F(t)^*}{E - (E_g + \omega_{\text{XUV}})}. \tag{4.17}$$

The coefficient $C_E(t)$ appears in the coupled equations under the integration $\int dE$ over continuum states, so this equation is actually a representation of a Green's function, namely,

$$C_E = \lim_{\epsilon\to 0^+} \frac{V_{Eb}C_b - D_{Eg}C_g F(t)^*}{(E_g + \omega_{\text{XUV}}) - E + i\epsilon}. \tag{4.18}$$

We then retain only the resonant contribution to integral over E in the Eq.(4.14) and the next equation, i.e., the contribution is proportional to $-i\pi\delta(E_g+\omega_{\rm XUV}-E)$. Making use of the definitions of Fano q parameter, we arrive at simplified equations for $C_g(t)$ and $C_b(t)$ for the discrete states,

$$i\dot{C}_g = -i\pi|D_{gE}|^2|F(t)|^2C_g - D_{gb}C_bF(t)(1-i/q) \tag{4.19}$$

$$i\dot{C}_b = [\Delta_b - i\Gamma/2]C_b - D^*_{gb}C_gF(t)^*(1-i/q), \tag{4.20}$$

with D_{gE} evaluated at $E=E_g+\omega_{\rm XUV}$ and $\Delta_b = E_b-(E_g+\omega_{\rm XUV})$. Here, q and Γ are the conventionally defined Fano q parameters that describe the line shape and the width,

$$q = \frac{D_{gb}}{\pi D_{gE}V_{Eb}} \quad , \tag{4.21}$$

$$\Gamma = 2\pi|V_{Eb}|^2 \quad . \tag{4.22}$$

Going back to the original expression for the $\Psi(t)$ in Eq.(4.3), we can express the leading contribution to the time-dependent dipole as

$$\begin{aligned} d(t) \equiv& \langle\Psi(t)|\hat{d}|\Psi(t)\rangle \\ =& \exp(-i\omega_{\rm XUV}t)C_g^*\left[D_{gb}C_b + \int dE\ D_{gE}C_E\right] + \text{c.c.} \\ =& \exp(-i\omega_{\rm XUV}t)\left[C_g^*D_{gb}C_b(1-i/q)\right. \\ & \left. +i\pi|C_g|^2|D_{gE}|^2F(t)^*\right] + \text{c.c.} \end{aligned} \tag{4.23}$$

So we need only $C_g(t)$ and $C_b(t)$ to evaluate this expression. We now make the approximation that the ground state is not appreciably depopulated, $C_g(t)\approx 1$, note also that on resonance $\Delta_b=0$, and solve the equation for C_b using the substitution $C_b = \exp(-\Gamma t/2)\,\bar{C}_b$ in the case of the Gaussian XUV pulse in Eq.(4.7) to obtain

$$C_b(t) = i\,e^{-\Gamma t/2}D^*_{gb}(1-i/q)F_{\rm XUV}G(t), \tag{4.24}$$

where we define

$$G(t) \equiv \frac{1}{2}\,e^{\Gamma^2\tau^2_{\rm XUV}/16}\left[1+\text{erf}\left(\Gamma\tau_{\rm XUV}/4 + t/\tau_{\rm XUV}\right)\right], \tag{4.25}$$

and erf is the error function. Assembling $d(t)$ we then find

$$\begin{aligned} d(t) = \quad & e^{-i\omega_{\rm XUV}t}\Big[i|D_{gb}|^2(1-i/q)^2 F_{\rm XUV}\, G(t)\, e^{-\Gamma t/2} \\ & + i\pi |D_{gE}|^2 F_{\rm XUV}\, e^{-t^2/\tau_{\rm XUV}^2} \left(\pi\tau_{\rm XUV}^2\right)^{-1/2} \Big] + \text{c.c.}. \end{aligned} \tag{4.26}$$

This is the expression for the polarization that we use to model transient absorption, by modifying it with either laser-induced attenuation or laser-induced phase shift as described in Sec. 4.5, and then Fourier transforming it according to

$$\tilde{d}(\omega) = \frac{1}{\sqrt{2\pi}} \int_{-\infty}^{\infty} dt\, e^{i\omega t} d(t) \tag{4.27}$$

to construct the response function in Eq.(4.2) that gives the transient absorption spectrum.

To make the connection with Fano line shapes in the pure XUV absorption spectrum we evaluate Eq.(4.26) in the limit of a delta function XUV pulse, $\tau_{\rm XUV} \to 0$, so that

$$d(t) = \begin{cases} 0 & , t < 0 \\ e^{-i\,\omega_{\rm XUV} t} \Big[i\,|D_{gb}|^2\,(1-i/q)^2 F_{\rm XUV} e^{-\frac{\Gamma}{2}t} & \\ \qquad + i\pi\,|D_{gE}|^2\,F_{\rm XUV}\delta(t)\Big] & , t \geq 0 \end{cases}, \tag{4.28}$$

and the Fourier transform of the polarization becomes

$$\tilde{d}(\omega) = \frac{1}{\sqrt{2\pi}} F_{\rm XUV} \left[i\pi |D_{gE}|^2 - \frac{(1-i/q)^2 |D_{gb}|^2}{\omega - \omega_{\rm XUV} + i\,\Gamma/2} \right]. \tag{4.29}$$

With this approximation to $\tilde{d}(\omega)$, and the Fourier transform of the corresponding XUV field, $\tilde{\mathcal{E}}_{\rm XUV}(\omega) = F_{\rm XUV}/\sqrt{2\pi}$, the absorption cross section now becomes

$$\begin{aligned} \sigma(\omega) &= 8\pi\alpha\omega\, \text{Im}\left[\tilde{d}(\omega)/\mathcal{E}(\omega)\right] \\ &= 8\pi^2\alpha\,\omega |D_{gE}|^2 \frac{(\omega - \omega_{\rm XUV} + q\,\Gamma/2)^2}{(\omega-\omega_{\rm XUV})^2 + (\Gamma/2)^2}, \end{aligned} \tag{4.30}$$

which has the well known form of the absorption cross section in the vicinity of an autoionizing feature with a Fano resonance line shape. In this limit of a delta function XUV pulse, it is possible to analytically evaluate the Fourier transform of

the modified d(t) in the case of sudden attenuation in the LIA model in Eq.(4.8) and see explicitly how it depends on the Fano q parameters of the unperturbed line shape. The change in the response function due to this sudden truncation of the polarization is

$$\Delta\tilde{S}(\omega;t_d) \equiv \tilde{S}(\omega;t_d) - \tilde{S}_{\rm XUV}(\omega), \tag{4.31}$$

and the final expression for $\Delta\tilde{S}(\omega;t_d)$ in this simple model, evaluated at the resonance energy $\omega = \omega_{\rm XUV}$ can then be shown to be

$$\Delta\tilde{S}(\omega=\omega_{\rm XUV};t_d) = |F_0|^2|D_{gE}|^2(1-q^2)e^{-\Gamma t_d/2}. \tag{4.32}$$

As we can see from Eq. 4.32 in this extreme version of the LIA model, the dependence on Fano q parameter of the change in the response function is negative or positive depending on whether q is greater or less than unity because of the factor of $1-q^2$ in Eq.(4.32).

4.8.2 NIR perturbation: The LIA and LIP models

We can extend the above approach to set up two superimposed polarizations corresponding to a pair of features of ndσ_g and nsσ_g+ndπ_g, as the weighted sum of two polarizations $C_{nd}\ d^{nd}(t;q_{nd},\Gamma_{nd}) + C_{ns}\ d^{ns}(t;q_{ns},\Gamma_{ns})$. The polarization labeled d^{ns} includes nsσ_g+ndπ_g contributions, and the weighting coefficients C_{nd} and C_{ns} are chosen to reproduce static absorption spectrum as in our Schwinger calculation.

We then calculate the response function as defined in Eq.(4.2) in spectral domain. The parameters, such as Fano q, the field-free decay life times Γ, and the amplitudes of dipole matrix elements D_{gb} and D_{bE}, are chosen so that the response function closely matches the static absorption line shapes shown in Fig. 4.1(b). The delay-dependent NIR perturbations are then modeled as LIA or LIP. In the LIA method, XUV initiated polarizations are attenuated slowly by an error function profile centered at some delay t_d to simulate the effect of excited state population removal by Gaussian shaped NIR pulse. The parameters used for the LIP calculations that determine the pondermotive energy function were $\mathcal{E}^0_{\rm NIR} = 5.3\times10^{-3}$ a.u.,

corresponding to an intensity of 1 TW/cm^2, and the NIR photon energy $\omega_L = 0.058$ a.u. (1.58 eV).

4.9 How Do We Probe Many-electron Correlations?

Here we extend our very recent experiments in O_2 [141] to study low-lying autoionizing Rydberg states in O_2. In our experiment, the H13 of XUV excites $2s\sigma_u$ orbital to the superexcited states embedded in ionization continua which we denote as $2s\sigma_u^{-1}(c^4\Sigma_u^-)$ $3s\sigma_g$ autoionizing Rydberg state converged onto excited ionic c-state. It this known that this state support two vibrational progressions ν'=0,1. In addition, H13 will also excite $3s\sigma_g$ orbital to autoionizing Rydberg states converged onto excited ionic B-state denoted as $3s\sigma_g^{-1}(B^2\Sigma_g^-)$ $np\sigma_g$. Here the principle quantum n=6,7,8,...; and each n supports vibrational progressions ν'=0$\sim$4. All these states are labeled Fig. 4.9(a) and (b), where (a) is our H13 spectra in logarithmic scale, and (b) is measured static XUV photoabsorption cross section by synchrotron adapted from Ref. [9].

Figure 4.9(c) shows measured transient absorption spectrogram in O_2. At two $3s\sigma_g(\nu'$=0,1) states, we can observe increased OD signals, which implies that the XUV photoabsorption is enhanced on these two autoionizing states. The $3s\sigma_g(\nu'$=1) state has much weaker signal comparing to $3s\sigma_g(\nu'$=0) state, and this can be attributed to very weak XUV intensity as in Fig. 4.9(a) at $\sim$21 eV to prepare the molecular polarization at that super-excited state. At $\sim$ 20.8 eV, $3s\sigma_g(\nu'$=0) autoionizing Rydberg states state also show pondermotive shift toward higher energy and parabolic-like structure as in those bounded Rydberg states in helium. To understand the enhancement of the absorption on these two states, we can apply the same approach we recently developed in Ref. [141].

Briefly, we first extracted Fano q parameters of these two states from static photoabsorption line shapes and calculated spectral line width ($\sim$0.15 meV) from Ref. [10], then, we get estimated Fano q parameter (q=$\sim$-0.6) by curve fitting. Next, we applied the LIP model on these two dipoles, and then calculated the

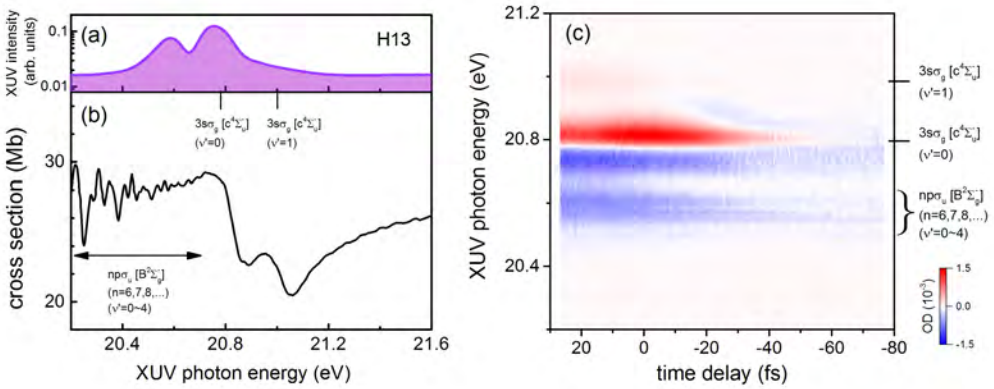

Figure 4.9: (**a**) The H13 of XUV spectrum used in O_2 experiment in logarithmic scale. (**b**) Measured total photoabsorption cross section adapted from Ref. [9]. Two major autoionizing Rydberg states under investigation are $3s\sigma_g(\nu'=0,1)$ converged to excited ionic c-state ($c^4\Sigma_u^-$). The black arrow indicates the range of other $np\sigma_u$ autoionizing Rydberg states converged to excited ionic B-state ($B^2\Sigma_g^-$), where n=6,7,8,...and each n can support $\nu'=0\sim4$. (**c**) Our experimental measured transient absorption spectrogram in O_2, where negative delay means that the XUV arrives at the target first.

change in this frequency-domain dipoles to get OD spectra, namely, $\sigma_{\text{XUV+NIR}}(\omega, t_d) \propto d_{\text{XUV+NIR}}(\omega, t_d) = d_{\text{XUV}}(\omega)e^{\phi(\omega,t_d)}$. Here $\phi(\omega, t_d)$ is the NIR induced frequency-domain quantum phase shift, i.e., $\phi(\omega, t_d) = \mathcal{F}[\phi(t, t_d)]$, where $\mathcal{F}$ represents Fourier transform. Since Fano q parameters of these two states are very similar to other higher lying autoionizing Rydberg states of $ns\sigma_g$ series we investigated very recently [141], we do expect to see the OD signal increase on these lower lying $3s\sigma_g$ states, just as those higher lying $ns\sigma_g$ states, where n=5,6,7,...

However, we note that quantitative dipole modeling based on the LIP model is challenging on this $3s\sigma_g$ states because of the presence of many other nearby autoionizing Rydberg states we assigned as $np\sigma_g$ states converged to the other continuum at an energy range of 20.3 to 20.8 eV. There are more than three np states here, and each np state supports at least five vibrational manifolds. As a result, these additional 15 states complicate the simple LIP based modeling which works better when quasi-isolated states are accessible. The combined net effect of these 15 states will show decreased OD signal as shown in 4.9(c) around 20.6 eV. We ten-

tatively attribute this absorption decrease to the original sign of 'effective' Fano q parameters in this energy range, which is due to the contribution of at least these 15 states in total. Higher spectral resolution is needed in this energy range to further investigate the origin of absorption decrease from these states.

CHAPTER 5

The Argon Experiment

5.1 Autoionizing States in Ar

When a inner electron from Ar atom is excited from 3s to np orbital, the $3s^{-1}np$ autoionizing states can be formed. Historically, these states are well characterized due to their prominent Fano spectral profiles [84, 202], which reads

$$\sigma = \sigma_a \frac{(q+\epsilon)^2}{(1+\epsilon^2)} + \sigma_b, \tag{5.1}$$

where $\epsilon = 2(E - E_r)/\Gamma$ is the reduced energy, E is the photon energy, E_r is the resonant energy, and Γ is the line width. Also, σ_a and σ_b are two portions of the cross section that correspond to transitions of the continuum that do and do not interact with the discrete autoionizing state, respectively. We can further define the correlation coefficient $\rho^2 = \sigma_a/(\sigma_a + \sigma_b)$, which is also termed the overlap integral. Many profile parameters in Ar autoionizing states have been extracted experimentally and theoretically such as Fano q parameter, natural line width Γ, correlation coefficient ρ^2 , effective quantum n^*. For example, $3s^{-1}4p$ state has E_r = 26.61 eV, q = -0.22 $\sim$ -0.31, Γ = 68–80 meV, n^* = 1.84–2.28, ρ^2 = 0.86–0.87 [203–207]. Figure 5.1 shows an measured photoabsorption cross section taken from Ref. [11]. This autoionization process reads

$$Ar(3s^2 3p^6)[^1S_0] \rightarrow Ar^{**}(3s^1 3p^6 4p)[^1P_0] \rightarrow Ar^{*+}(3s^2 3p^5)[^1S_0] + e^-(3p^{-1}\epsilon s/\epsilon d). \tag{5.2}$$

Apart from the common Fano parameterization, there is an alternative way to characterize these autoionizing states based on scattering theory as first formulated

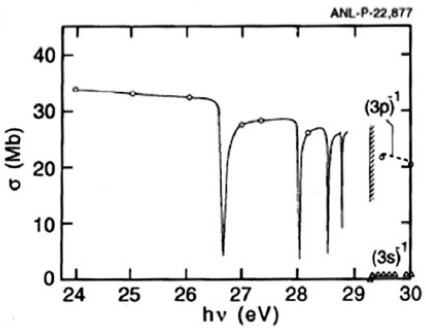

Figure 5.1: Argon partial cross-sections normalized to the absolute total cross sections in the window resonances of the range 24–30 eV, taken from J. Berkowitz. "Atomic and molecular photoabsorption: absolute total cross sections". Academic Press (2002) [11].

by Shore [208–210]. The connection, extension, and the universality for Fano profile have been discussed recently [211], including the extension of real q parameter to the complex number to account for the decoherence [212, 213] or external field effects [214].

Attoseccond techniques have also found useful applications in the study of autoionization states. For instance, the RABBIT based photoelectron spectra [216] has been used to extract phase information and the transient absorption spectra [66, 159] has been utilzed to study its decaying dynamics. In our study, we expand on these studies by investigating the effects of laser field polarization and intensity–the control of the autoionizing line shape in Ar by an external laser field.

5.2 The Control of Laser Induced Couplings

Figure 5.2 shows analogies and comparisons between different types of interferometers. Generally, interferometers are investigative tools used to superimpose waves in a manner that gives rise to interference patterns, from which information can be extracted. Figure 5.2(a) is a schematic of a typical optical Mach-Zehnder interferometer that is commonly used to extract information of a system under investigation, where BS stands for beam-splitter, M for mirror, $\psi(z)$ is a phase shifter along laser propagation direction z, which represents the system under investigation. The

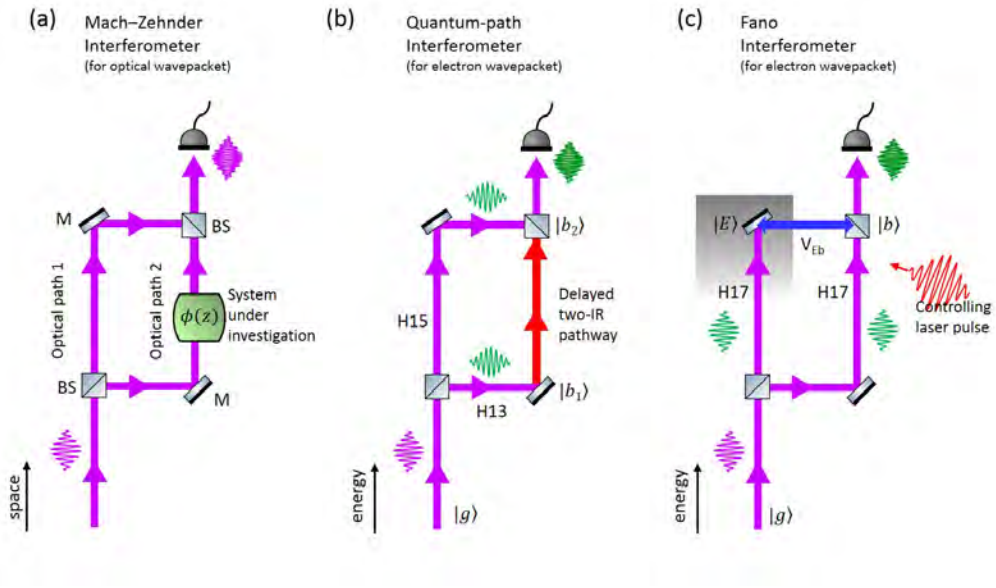

Figure 5.2: (**a**) A common optical Mach-Zehnder interferometer. (**b**) A quantum-path interferometer for electron wavepackets as demonstrated in Fig. 3.15. (**c**) A Fano interferometer for interfering a discrete and a continuum state, modified by an external laser.

purple wavy pulse represents an optical pulse (wavepacket) used in this system. Figure 5.2(b) shows a quantum-path interferometer in helium Rydberg 1s2p ($|b_1\rangle$) state and 1snp states ($|b_2\rangle$) for electron wavepackets (green wavy pulse), prepared by an XUV photon (green wavy pulse) and an XUV photon with two additional IR photons, respectively. This quantum-path interferometry in helium can be observed by measuring XUV photoabsorption spectrum as in Fig. 3.15, or by measuring ionized photoelectron spectrum as in Ref. [215].

Figure 5.2(c) shows a special type of the quantum-path interferometer called "Fano interferometer." Instead of producing two common transition pathways by two-photon assisted photoexcitation, a Fano interferometer couples two quantum transition channels by electron-electron Coulomb coupling, i.e., the configuration interaction. The autoionization process in Ar can be thought of an example of this Fano interferometer. In our ATA experiment of Ar, we use an external NIR laser to modify the coupling channels of the autoionizing states to their neighboring discrete and continuum states.

There are many possible one-photon excitation pathways that need to be considered in this system [216]. Figure 5.3(a) shows a schematic energy level diagram of the first few Rydberg states for s and p electron excitation channels in the $^1P^0$, $^1S^e$, $^1S^e$ symmetries [217].

XUV H17 (purple arrows) is used to excite 3s core electron of Ar to 4p autoionizing state, and NIR (red arrows) is used to control one-photon transitions. Blue arrows represent intrinsic electronic couplings between quasi-bound states and the continua. In addition to one NIR photon transition, there are also two groups of two-photon transition pathways available in this system as schematically illustrated in Fig. 5.3(b). The first group is the direct two-photon transition (R1 and R2 transitions), which is sometimes called RABBIT transition as it is used in RABBIT scan during a photoelectron measurement. The second group is the self-dressing transition (D1 and D2 transitions), including D1, absorbing one photon and then emitting one photon, and D2, emitting one photon and then absorbing one photon. In fact, we can think of this two-photon self-dressing effect as the full quantum mechanical equivalence of the ac Stark effect, which is a semi-classical picture that treats the NIR dressing field as the classical electromagnetic wave.

As we can see from this diagram that by manipulating a subsequent NIR pulse, in terms of its peak intensity, field polarization, and XUV-NIR time-delay, we could potentially control couplings in this system.

5.3 Laser Polarization Controlled Spectral Profiles

In our experiments, we use a 790 nm NIR laser pulse as an impulsive control field to modify the ATA line shapes in Ar. Figure 5.4(a)-(d) illustrate the changes in the ATA line shapes as the relative angle between the NIR and XUV fields varies from being perpendicular to being parallel to each other. An XUV H17 spectrum is shown on top of its associated ATA line shape with its NIR peak intensity labeled . From Figure. 5.4(a), we can observe a prominent asymmetrical profile when the NIR and XUV fields are parallel. It is also interesting to note that the red-detuned side of the

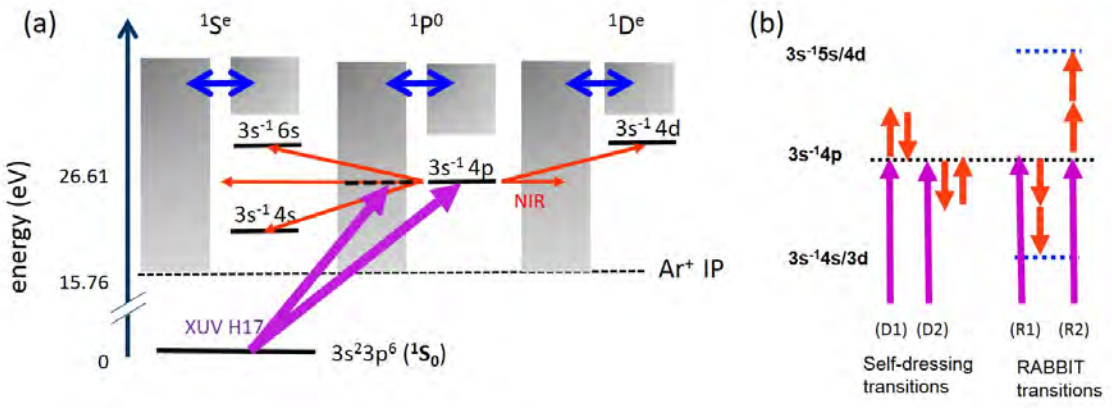

Figure 5.3: (**a**) Schematic energy level diagram that is relevant to the Ar experiment. XUV (purple arrows) is used to excite an 3s electron of argon to 4p autoionizing state, and NIR (red arrows) is used to control the transitions. Blue arrows represent intrinsic electronic couplings (configuration interactions) between bound states and the continua. (**b**) Two groups (four types) of dominant processes in our experiment, including one-photon and two-photon transition pathways starting from 4p state.

XUV spectrum (lower energy side comparing to 4p resonance energy) shows negative OD. The profiles become increasingly symmetrical as the angles between NIR and XUV fields increases. In the extreme case where the two fields are perpendicular to each other, a relatively more symmetric profile is produced (Fig. 5.4(d)). Note that negative OD implies XUV absorption decreases in the presence of NIR controlling field. As the NIR peak intensity increases, the difference between the minimum and maximum energy in the spectrum increases, which leads to greater asymmetricity in the spectral profile. Up to highest intensity as Figure. 5.4(d), an additional stronger absorption feature appears at the center of the 4p resonance.

Next, we fixed the IR intensity at 5×10^{10} TW/cm^2 and varied the delay as shown in Figure. 5.5(a)-(c). There are some changes at different delays, but the general features are the same, where parallel condition gives strong asymmetry on the profiles, while the perpendicular condition does not. The manner which the spectral profiles change is similar to the previous case, whereby the symmetricity decreases as the angle between the XUV and NIR fields increases. Likewise, a negative time delay means XUV reaches the sample gas before the NIR does.

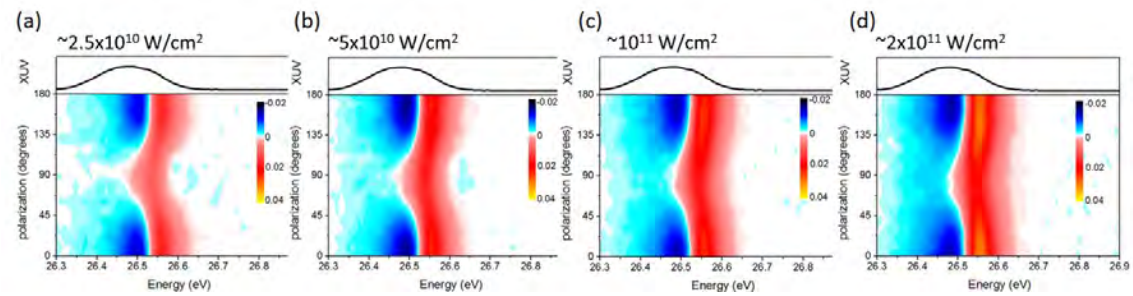

Figure 5.4: Top panels: XUV H17 spectra. Bottom panels: ATA spectra of Ar near delay zero ($t_d \sim 0$) as a function of relative (linear) polarization angle between XUV and NIR. (**a**)-(**d**) show the spectra at different NIR peak intensities labeled on the top.

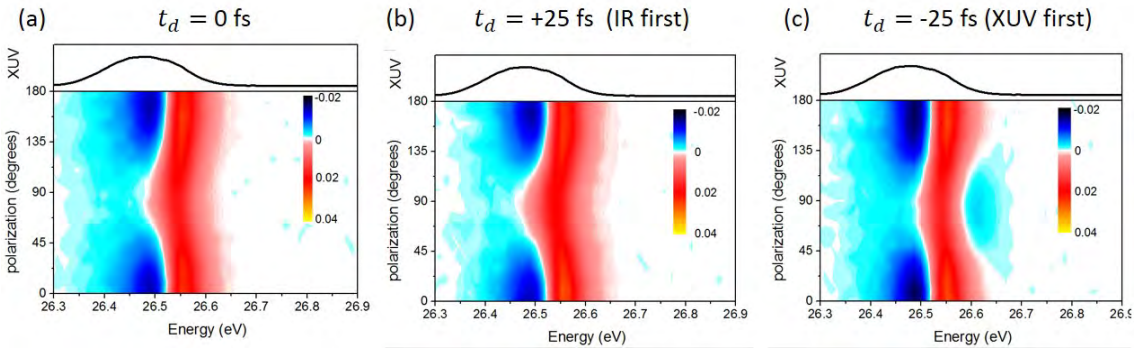

Figure 5.5: ATA spectra at NIR peak intensity 5×10^{10} TW/cm^2 as a function of XUV-NIR time delay. Delays for each plot are labeled on the top.

We now show a few representative line-outs from the above two figures and they are shown in Fig. 5.6(a)-(d) for various NIR intensities and delays. For all delays ($t_d = 0 \pm 25$ fs) and NIR intensities, we observe the same behavior that parallel polarization cases show Fano-like (or Beutler-Fano-like) spectral profiles, while perpendicular polarization cases show Lorentzian-like (or Breit-Wigner-like) spectral profiles. The Fano-like profiles indicate strong two quantum-path interference (ground-to-bound and ground-to-continuum channels), and the continuum state's Coulomb coupling (configuration interaction) to the bound state is important in this case. Therefore, it appears that the presence of parallel controlling NIR field either enhances one of the transition channels, or as one could argue that it suppresses the other channel. It is not possible to experimentally determine which is actually the

case.

Rigorously speaking, these spectral profiles are Fano-like, instead of real Fano line shapes. It is correct that Fano q is an important parameter that characterizes the autoionizing resonances such as Ar 4p state. However, in the case of laser-perturbed or laser-controlled autoionizing resonances, the resultant absorption line shape is not a real Fano profile in general. Only if specific assumptions are made, along the lines of what are described in Ref. [70], where they considered a 'constant' pondermotive shift, applied 'only' to the bound state, can one argue that the new absorption line shape in the presence of laser field has a Fano character with a modified q value. In a real experiment with non-negligible NIR pulse duration, the ponderomotive phase shift is time-dependent, applied to both bound and continuum contributions, and we obtain a non-Fano absorption line shape that includes oscillations on either side of the resonance (ringing wings) due to a perturbed FID.

In contrast, in the cases of a perpendicular polarization, we get noticeable Lorentzian-like profiles, which indicate stronger absorption on the resonance due to the enhancement of ground-to-bound transition (or the suppression of ground-to-continuum transition). In the extreme case, if there is no contribution from the continua, the line shapes will revert to conventional Lorentzian profiles. Different spectral profiles imply different couplings between autoionizing states and the continua as theoretically discussed by Lambropoulos *et al.* [218].

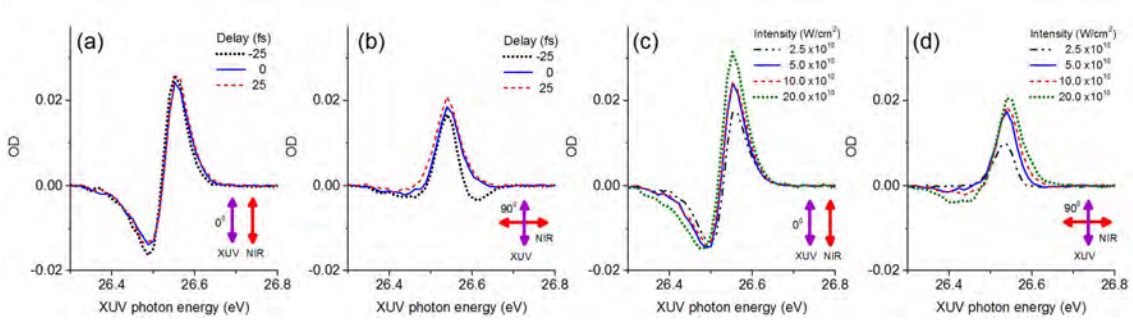

Figure 5.6: (**a**)-(**b**) Delay-dependent line-outs at 5×10^{10} TW/cm^2 from Fig. 5.4; (**a**)-(**d**) NIR intensity-dependent line-outs at $t_d = 0$ from Fig. 5.5. Note that all parallel polarization cases show Beutler-Fano spectral profiles, and all perpendicular polarization cases show spectral Breit-Wigner profiles.

We can also extend the similar controlling scheme to an elliptically polarized NIR field. The NIR ellipticity is controlled by rotating a broadband quarter-wave plate after a fixed half-wave plate and a fixed linear polarizer in the NIR delay-line before a holed mirror. Note that depending on the geometry of our periscope for NIR beam delivery, we have to take the polarization-preserving or non-polarization-preserving periscopes into account [219] to get correct the NIR field polarization.

Figure. 5.7 shows ellipticity-dependent ATA spectra at delay zero with two different NIR peak intensities. The definition of ellipticity is illustrated in Fig. 5.7(e), where 0^0 means that the NIR and XUV pulses are both linearly polarized and parallel, while $\pm 45^0$ means that the NIR pulse is circularly polarized. Here the handedness (right-hand or left-hand circular polarization) of the NIR field makes no difference in our experiments because that there are no magnetic quantum levels involved and an Ar atom is not chiral. Figure 5.7(a)-(d) show that the spectral profiles are more asymmetrical Fano-like for linearly polarized controlling field, regardless of the peak intensity used. Conversely, the symmetrical Lorentzian-like spectral line shapes can be observed when a circularly polarized NIR field is applied.

As a result, we can summarize that as the NIR field deviates from a parallel geometry, either in a perpendicular or a circular geometry, the bound state transition will dominate the XUV excitation process. Thus, the role of the continuum state coupling to both ground and the bound state is reduced.

5.4 Coupling Channels: A Theoretical Calculation

To fully unveil the NIR controlled spectral profiles in XUV photoabsorption, we have to model and calculate the couplings by NIR photons (up to third-order perturbation, or up to two-photon coupling regime) to neighboring states of Ar $3s^{-1}4p$. First, we briefly describe an analytical expression for atomic dipolar response in the presence of an electromagnetic field in the electric dipole approximation (EPA). The derivation of this general expression depends on finding the Fourier transform of the expectation value of the total electronic momentum ($\tilde{P}_{\nu}^{(n)}(\omega)$) in velocity gauge,

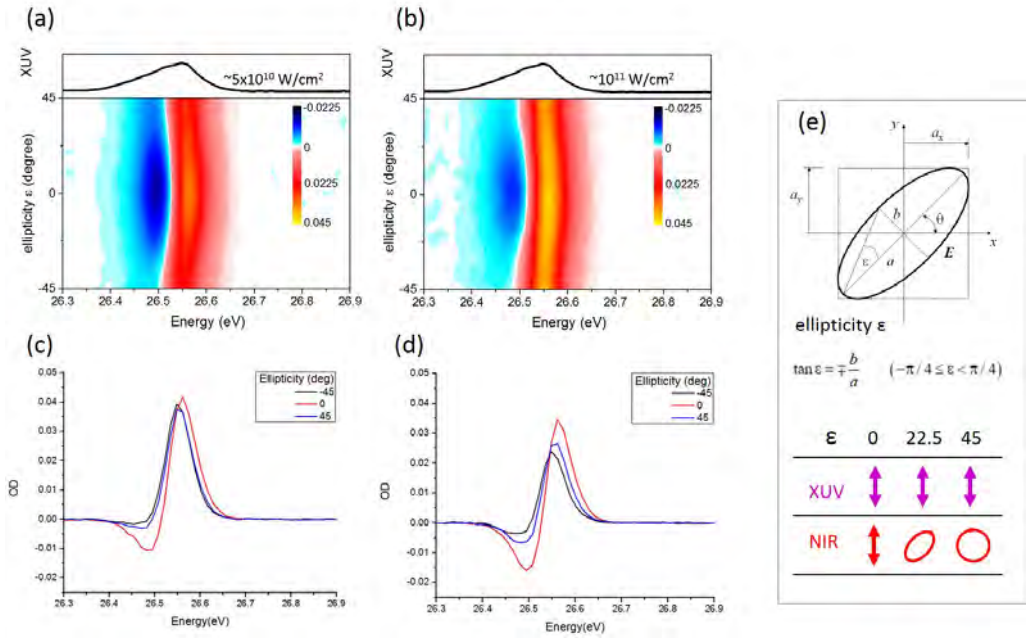

Figure 5.7: The ATA spectra at delay zero with intensity (**a**) 5×10^{10} TW/cm^2 and (**b**) 10×10^{10} TW/cm^2 as a function of NIR ellipticity. Some representative profiles at delay zero with different ellipticity at intensity (**c**) 5×10^{10} TW/cm^2 and (**d**) 10×10^{10} TW/cm^2. (**e**) The definition of the ellipticity, with some schematic examples of the IR field, where the x-y plane is orthogonal to the laser pulse propagation direction.

where n is at n-th order expansion, ω is the photon energy, and ν is the final state. The imaginary component of $\tilde{P}_\nu^{(n)}(\omega)$ is proportional to the transient absorption cross section, namely, $\sigma(\omega) \propto Im[\tilde{P}_\nu^{(n)}(\omega)]$.

Due to the odd parity of the dipole operator, an even number of dipole transitions are required for $\tilde{P}_\nu^{(n)}(\omega)$ to be non-zero, unless the process involves one XUV photon and one NIR photon. Therefore, as a first approximation, we restrict our attention to processes involving a single XUV photon and two IR photons. Since it is reasonable to assume that the dominant processes are those that occur in the vicinity of a resonance, processes which begin with the absorption/emission of an NIR photon are neglected. Our model assumes that the ground state is by far the most dominantly populated state, and thus diagrams beginning with the emission of an XUV photon are not considered. This leaves us with four possible types of transitions (D1, D2, R1, R2) to consider, as shown in Figure. 5.3(b). The RABBIT transitions R1 and

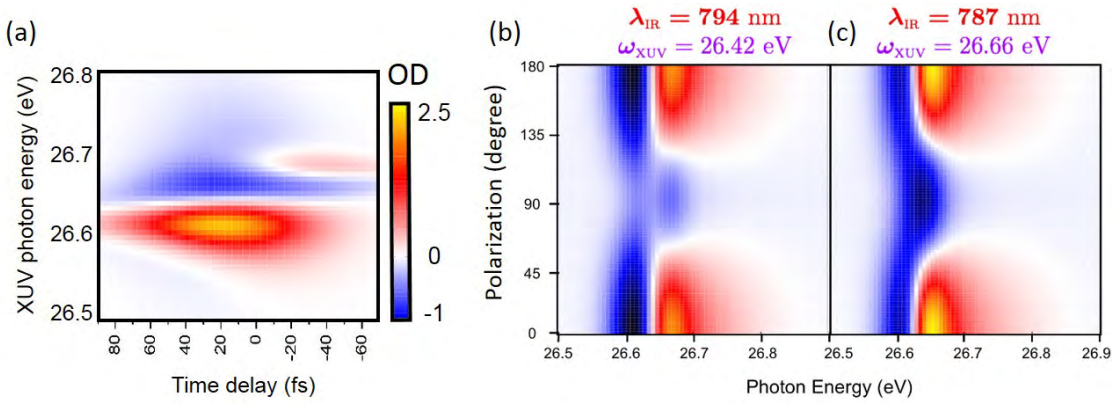

Figure 5.8: (**a**) Calculated ATA spectrogram including four types of two NIR photon coupling channels. (**b**)-(**c**) Calculated ATA spectra as a function of relative (linear) polarization angle between XUV and NIR at delay zero with two slightly different XUV central energy and two controlling NIR central wavelength. Calculation by L. Argenti and C. Cariker (private communication, 2017).

R2 involve either the absorption or emission of both NIR photons, resulting in the population of a neighboring resonance. If the relative intensity of the neighboring XUV resonance is small, these processes are expected to contribute weakly. The self-dressing transitions D1 and D2, each involve the absorption and emission of one NIR photon.

Next, we evaluate transitions involving three photons (XUV and two NIR) by truncating the perturbative expansion at 3rd order ($\tilde{P}_\nu^{(n=3)}(\omega)$). The matrix elements for the transitions to and from the intermediate states are related via the Wigner-Eckart theorem by a geometrical coefficient multiplied by the reduced matrix element with associated Clebsch-Gordan coefficients.

Combining our analytical formalism with calculated matrix elements, we plot the theoretical ATA spectrogram in Fig. 5.8(a) with OD change in arbitrary units. The spectral profiles in that figure is expectedly asymmetrical since the XUV is parallel to the NIR field. Also, at larger negative delays when the XUV precedes, we observe the development of ringing wings due to the perturbed FID. In the following, we further vary the relative field polarization angle between XUV and NIR to get Figure 5.8(b) and (c), with slightly different XUV center energy and

NIR central energy. These two ATA spectra agree with our experimental findings that parallel field polarization shows asymmetric Fano-like profiles, while perpendicular field polarization shows more symmetric Lorentzian-like spectral line shapes.

(Note: Theoretical derivation and calculation discussed in this section come from our collaboration with Prof. L. Argenti and C. Cariker at the University of Central Florida.)

5.5 Summary

In summary, we employed an external NIR laser to control argon $3s^{-1}4p$ autoionizing state. By manipulating the NIR field polarization from linear, either parallel or perpendicular to the XUV field, to circular polarization, we observe significantly modified spectral profiles. Specifically, when the NIR and XUV polarization are parallel, the change of absorption profiles exhibits Beutler-Fano-like shapes, while the perpendicularly linear or circular polarized NIR field will change the line shapes to more symmetric Lorentzian-like (Breit-Wigner-like) profiles. We also calculate theoretical ATA spectrograms with different NIR field polarization to confirm our observations. Our study demonstrates an external field controlled Fano interferometer on the photoexcitation pathways of autoionizing electrons.

CHAPTER 6

The Nitrogen Experiment

6.1 Introduction

As the most abundant species on earth's atmosphere, the electronic and vibrational structure of the neutral and cationic molecular nitrogen N_2 is widely studied. It also plays an important role in planetary science as it is the major constituents of the upper atmosphere of Jupiter, Saturn, Titan, etc. In the XUV spectral range, the solar and stellar radiation excites N_2 to neutral superexcited states above first ionization potential via single photon excitation from the ground state. The dynamics of N_2 excited and super-excited states continues attracting many recent studies, who have been focusing on the process of photoionization, dissociation, and predissociation, see for instance, in Ref. [220–223], by measuring photoelectron or photoion spectra.

An alternative method of charge detection is to measure the photoabsorption such as the ATAS. Over the past few years, there are growing applications and efforts to apply the ATAS to study molecules such as H_2 and O_2 [141, 224]. However, the interpretation of the experimental results from such complex molecular systems have proved to be challenging [225–227]. Very recently, there are some experimental studies on N_2 excited states using the ATAS [228, 229]. In those studies, lower energy XUV photons at 10–20 eV, usually called vacuum ultraviolet (VUV), are applied to investigate valence Rydberg series of b-state and b'-state, as well as autoionizing Rydberg states, converged onto N_2^+ ionic X-state ($X^2\Sigma_g^+$), A-state ($A^2\Pi_u$), and B-state ($B^2\Sigma_u^+$). Many superpositions of excited vibrational wavepackets are coherently prepared due to the broadband XUV or VUV continuum excitation, and the quantum beat over the XUV-NIR time delays was observed [230]. This technique is known as quantum beat spectroscopy. Due to the coupling by one or many NIR photons between different states, the quantum beat spectroscopy shows a common

feature observed in many atomic experiments that uses the ATAS.

In our ATAS experiments presented in this chapter, we extended the XUV photon energy to above 20 eV and studied the transient response of autoionizing Rydberg series converged onto excited ionic C-state ($C^2\Sigma_u^+$) of N_2^+. We begun with identifying the relevant states under investigation, and then we employed the ATAS to observe the relaxation dynamics of molecular polarization that consists of many vibrational wavepackets from two Rydberg manifolds under the perturbation of the NIR field. We also applied a simple dipole model to get an intuitive physical understanding of the observed ATAS spectrograms.

This chapter is organized as follows: after the introduction in Section 6.1, we begin by discussing various and rich energy states of N_2 in the spectral range of our interest in Section 6.2. We compared experimental measurements from literature and extracted relevant properties of the autoionizing states accessible via the ATAS. In Section 6.3, we briefly introduce our ATAS setup before discussing our experimental observations of N_2 molecular polarizations under NIR perturbation. In Section 6.4, we propose a simple dipole model to explain what we observed in the experiment, while noting its limitations which led to differences between predictions of the model and the experiment. We end the chapter with a summary in Section 6.5.

6.2 Energy States Accessible by Photoabsorption

There are many states that exist in the relatively narrow energy range 22–25 eV (50–56 nm) of N_2, which include excited ionic states, neutral Rydberg states, and other possible non-Rydberg doubly excited states (NRDES) [231]. Therefore, it is very important to understand which of the above energy states are accessible by static or transient photoabsorption measurements. It is known that there are at least six excited ionic states that have been identified [13]. The dominant ionic states are C-state ($C^2\Sigma_u^+$) and 2-state ($2^2\Pi_g$), where the former is much stronger. In Fig. 6.1(a), we show a high resolution photoelectron spectrum (green dashed-dotted curve) and a

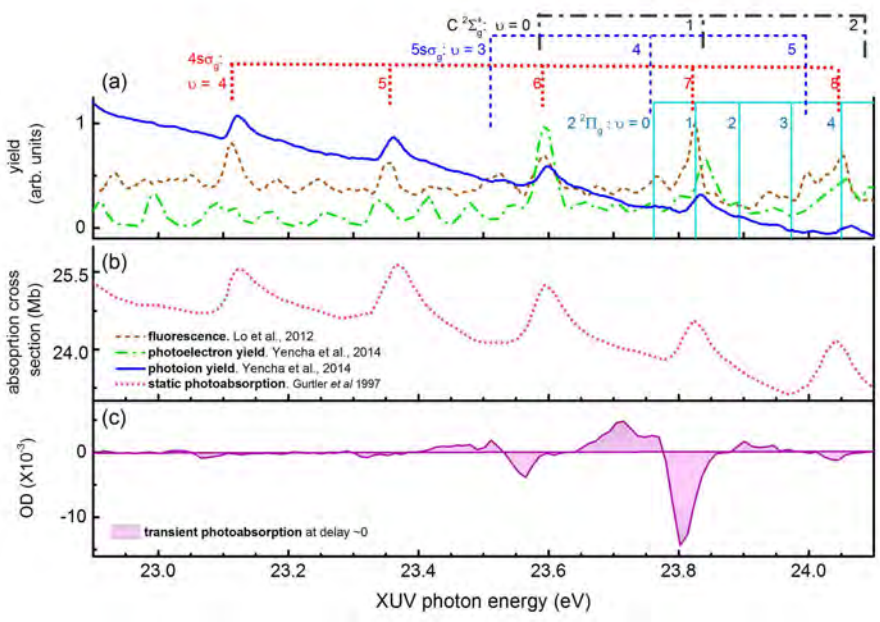

Figure 6.1: (Color online) Various spectral measurement at 23-24 eV of N_2. (a) The fluorescence excitation spectrum (brown dashed curve) adapted from Lo *et al.* 2012 [12], the photoion spectrum (blue solid curve) and the photoelectron spectrum (green dashed-dotted curve) adapted from Yencha *et al.* 2014 [13], of N_2 in the energy of 23-24 eV. (b) The static photoabsorption spectrum (pink dotted curve) adapted from Gürtler *et al.* 1997 [14]. (c) Our measured transient absorption spectrum (purple solid-filled curve) at delay zero.

photoion spectrum (blue solid curve), adapted from recent measurements by Yencha *et al.* [13], where the most relevant excited ionic states, including their vibrational progressions, are labeled at the top. In addition, we also show a high-resolution fluorescence excitation spectrum (brown dashed curve), adapted from Lo *et al.* [12], overlayed on Fig. 6.1(a). Note that the energy axis of this fluorescence spectrum is shifted by 7 meV to align with the energy state assignments given by Yoshii *et al.* [232]. The fluorescence emission stems from neutral excited atomic nitrogen fragments which are produced through direct dissociation and predissociation from many-electron excited neutral Rydberg states. Similar fluorescence spectrum was also measured in Ref. [233] with detailed Rydberg states assignments.

In contrast to the photoelectron or the photoion spectra, the static photoab-

sorption spectrum is only sensitive to neutral states as in the fluorescence spectrum. Figure 6.1(b) shows a XUV photoabsorption spectrum that was measured with a synchrotron (pink dotted curve), adapted from Gürtler *et al.* [14]. Although all ionic states could have Rydberg series converged to them, only one strong Rydberg series, called Codling's Rydberg series, converged to C-state has been observed and assigned in the literature [234].

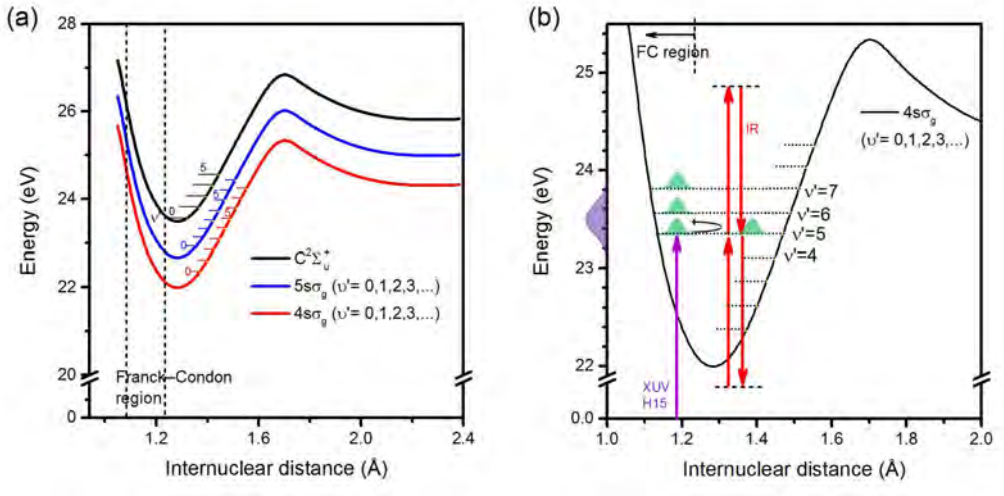

Figure 6.2: (Color online) (a) A selection of potential energy curves of N_2 with Codling's Rydberg series $1\pi_u^{-1}3\sigma_g^{-1}1\pi_g^1\ ns\sigma_g$ (n=4,5)($\nu' = 0,1,2,3,...$), converged onto excited ionic C-state ($C^2\Sigma_u^+$). (b) A schematic experimental process in our transient absorption experiment.

Figure 6.2(a) shows a selection of potential energy curves of N_2 with two relevant $ns\sigma_g$ Rydberg series and the C-state. The Codling's double-holed doubly-excited Rydberg series has electronic configuration $1\pi_u^{-1}3\sigma_g^{-1}1\pi_g^1\ ns\sigma_g$ ($C^2\Sigma_u^+$) with n = 4, 5, or with effective quantum n^* = 3, 4, where ν' is vibrational progression and $\nu' = 0, 1, 2, 3, ...$ Due to the limited spectral resolution in Gürtler's measurement, only $4s\sigma_g$ series can be identified in their measurements. From the spectral line shape of their static absorption, we have estimated that these Rydberg states have approximated lifetime up to 25 fs from the spectral width of 26 meV. Combining the fluorescence spectrum (brown dashed curve) and the photoion spectrum (blue solid curve) in Fig. 6.1(a), and the static photoabsorption spectrum (pink dotted curve)

in Fig. 6.1(b), one may tentatively conclude that the dominant Rydberg series is the $4s\sigma_g$ series, while the $5s\sigma_g$ series can be neglected.

However, based on the high-resolution fluoresence excitation spectrum by Ukai *et al.* [233], and our transient absorption spectra, shown in Fig. 6.1(c) at delay zero, we believe that the weaker contribution of the $5s\sigma_g$ states should also be included. We will discuss this further in our transient absorption experiment in Section 6.3 and modeling in Section 6.4. In fact, in addition to n = 4 and n = 5 series, the Ukai *et al.*'s measurement shows that other larger n, up to n = 10, could exist. Nevertheless, all existing XUV photoabsorption spectra in the literature, such as Ref. [14, 235], only measured and identified n = 4 and n = 5 series.

Besides, it was predicted that the $ns\sigma_g$ series has a small amount of mixing from $2\sigma_u^{-1}1\pi_g^1$ with the excited ionic B-state ($B^2\Sigma_u^+$) core configuration [236, 237]. Also, it is known that the electrons in this $ns\sigma_g$ series will autoionize to excited ionic A-state (∼90 %) and B-state of (∼10 %), respectively [238].

Apart from the excited ionic states and neutral Rydberg states, some studies suggest the existence of non-Rydberg doubly excited states (NRDES) in this energy range. These NRDES are short-lived repulsive states and will dissociate within femtosecond range. There are four possible assignments of NRDES in our spectral range of interest, namely, $1\pi_u^{-1}3\sigma_g^{-1}1\pi_g^2$, $(2\sigma_g/2\sigma_u)^{-1}1\pi_g$, $3\sigma_g^{-2}1\pi_g np\sigma$, and $1\pi_u^{-1}3\sigma_g^{-1}1\pi_g(np\sigma/np\pi)$ as described in Ref. [233, 239–241]. These NRDES, centered at ∼23.5 eV with a broadband feature extending more than 1 eV, were measured using static photoelectron spectra and fluorescent spectra [231, 242].

In the case of atoms and small diatomic molecules such as N_2 and O_2, the photonion spectra showed very similar spectral features, such as the Fano q parameter, as the photoabsorption spectra. The Fano q parameter, also termed as the Fano shape index [84, 202, 218], can be defined as $q = D_{gb}/(D_{gE}V_{bE})$. The D_{gb} is the electric dipole moment from ground state to a discrete quasi-bound state such as the $ns\sigma_g(\nu'=7)$ autoionizing state, the D_{gE} is the electric dipole moment from ground state to a continuum state, and the V_{bE} is the Coulomb electronic coupling, which is the configuration interaction term between a bound and a continuum state. The

physical origin of the Fano q parameter can be interpreted as the interference of these two photoexcitation pathways. From the static photoabsorption spectrum of N_2 in Fig. 6.1(b), we extracted the Fano q parameters from the $4s\sigma_g(\nu' = 4\text{–}9)$ states, and found that they lie between $\sim$ 1.5–2.5. Although the $5s\sigma_g$ static absorption spectrum is not directly accessible from the static absorption spectrum, we expect that their Fano q parameters are similar to those of $4s\sigma_g$'s. We have experimentally confirmed this to be true for the case of the autoionizing Rydberg series of molecular oxygen [141].

6.3 Transient Absorption Spectrograms

Our experimental apparatus of ATAS is shown in Fig. 6.3, which has been discussed in detail elsewhere [7]. In short, a Ti:Sapphire amplifier is used to generate $\sim$40 fs NIR pulses at 1 kHz repetition rate with 2 mJ pulse energy. The central wavelength of the NIR pulse is at 780 nm, and the laser has no active carrier-envelope phase stabilization. The NIR pulse is split into two paths in which one pulse is time-delayed with peak intensity at $\sim$ 1 TW/cm^2, while the other pulse is used to generate XUV by high harmonic generation (HHG) in a xenon-filled semi-infinite gas cell (SIGC). A 200 nm thick aluminum film filter is used after the SIGC to block the residual NIR. The HHG process generates an XUV attosecond pulse train (APT), which has dominant harmonics H13, H15, H17, and H19. In our experiments, we utilized the H15 to excite autoionizing Rydberg series of N_2. The XUV APT is combined with the other NIR pulse by a holed mirror, and it has the same linear polarization as the NIR pulse. The target N_2 gas is contained in a 10 mm long gas cell with a backing pressure of 3-4 torr, which is designed as such to enable the signal to be strong and immune to the macroscopic propagation effect [64, 89]. A homemade spectrometer is used to measure the XUV spectra, which triggers a shutter on the NIR beamline to get subsequent background (NIR free) XUV spectra $I_{out}^{XUV}(\omega)$, and the spectra with the presence of NIR $I_{out}^{XUV+NIR}(t_d, \omega)$ at a XUV-NIR time delay t_d. We adopt the convention that negative delay implies that XUV arrives at the target before

the NIR pulse does. We then calculate the averaged optical density change (OD) due to the presence of NIR at each delay as $OD(\omega, t_d) = -log_{10}(I_{out}^{XUV+NIR}/I_{out}^{XUV})$.

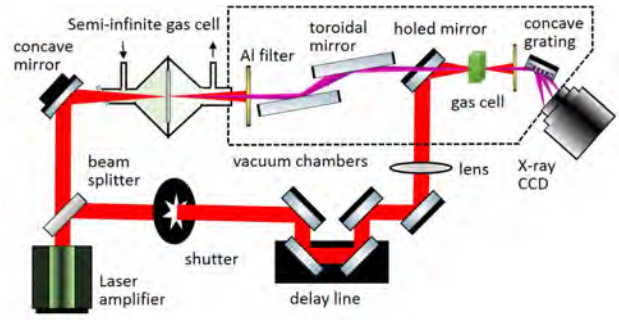

Figure 6.3: (Color online) The experimental setup for XUV attosecond transient absorption spectroscopy used in N_2 experiment.

Figure 6.2(b) shows a schematic experimental process in our transient absorption experiment. The XUV H15 first coherently prepares N_2 molecular polarization of doubly-excited autoionizing states with numerous vibrational states. These polarization, shown in green wave packets in Fig. 6.2(b), evolve freely in the molecular potential well until the arrival of the time-delayed NIR pulse. There is no optical transition pathway nearby to couple these polarization to other electric dipole allowed states because of the NIR photon energy used here. Therefore, the only possible NIR induced effect is the two-photon self-dressing effect, which induces delay-dependent ac Stark shift in the semiclassical picture. This is the scenario termed perturbed free induction decay (PFID).

Figure 6.4 shows measured transient absorption spectrograms with three different detuned H15 spectra shown on the side. First of all, in Fig. 6.4(a), we can clearly observe the temporal evolution of the $5s\sigma_g$ ($\nu' = 1\sim5$) states shown in the figure as horizontal bands in green with negative OD. The negative OD indicates that the XUV photoabsorption is reduced in the presence of the NIR field. We can also observe parabolic structures at negative delays, e.g., at delay t_d = -30 – -40 fs at ~23.8 eV of Fig. 6.4(a), which is the manifestation of the PFID in the spectrogram. When the central energy of the XUV spectra is tuned as shown in Fig. 6.4(b) and (c), the PFID at lower vibrational levels become more visible. The transient absorption

signal from the $4s\sigma_g$ series is more subtle, and it does not show clear a PFID. However, as we will see later in the line-outs of the spectrogram that some finer spectral features could be attributed to this series.

In between two major vibrational levels such as $5s\sigma_g$ $\nu' = 3$ and $\nu' = 4$ states at 23.65 eV in Fig. 6.4(a), we observed strong and enhanced transient absorption signal with positive OD, which indicates the increase of the XUV absorption in the presence of the NIR field. This behavior cannot be simply attributed to the PFID, since there is no strong $ns\sigma_g$ state accessible at those energies. We only observe this strong absorption enhancement when the XUV and the NIR pulses are overlapped, which implies that these are short-lived changes manifested by the NIR pulse, and they are different from the most of the NIR perturbed autoionizing Rydberg states that shows strong PFID features. Similar effects can be found at other energies in between two vibrational states such as $5s\sigma_g$ $\nu' = 2$ and $\nu' = 3$ around 23.40 eV in Fig. 6.4(c). As we will discuss in the end of Sec. 6.4, these broadband features could be due to the enhanced XUV absorption from other non-Rydberg states.

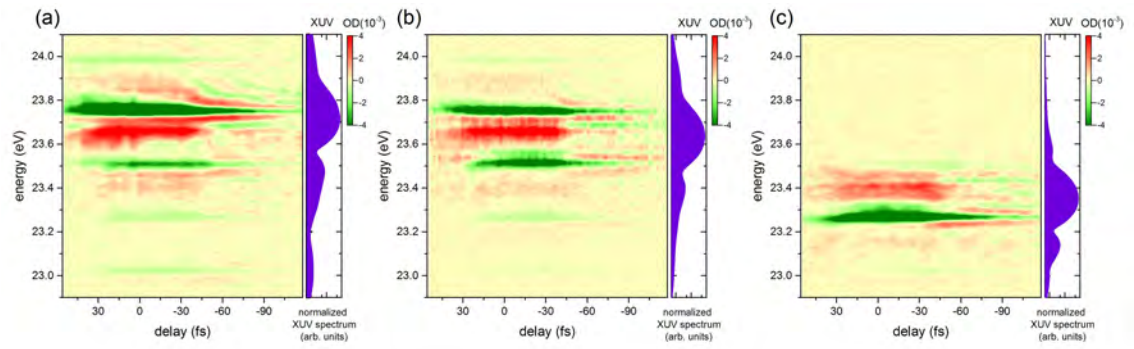

Figure 6.4: (Color online) Measured transient absorption spectrograms on N_2 double-holed and doubly-excited autoionizing Rydberg states. The detuned and transmitted XUV spectra in the absence of the NIR field are shown on the side for reference. The normalized XUV spectra are on a logarithmic scale in arbitrary units.

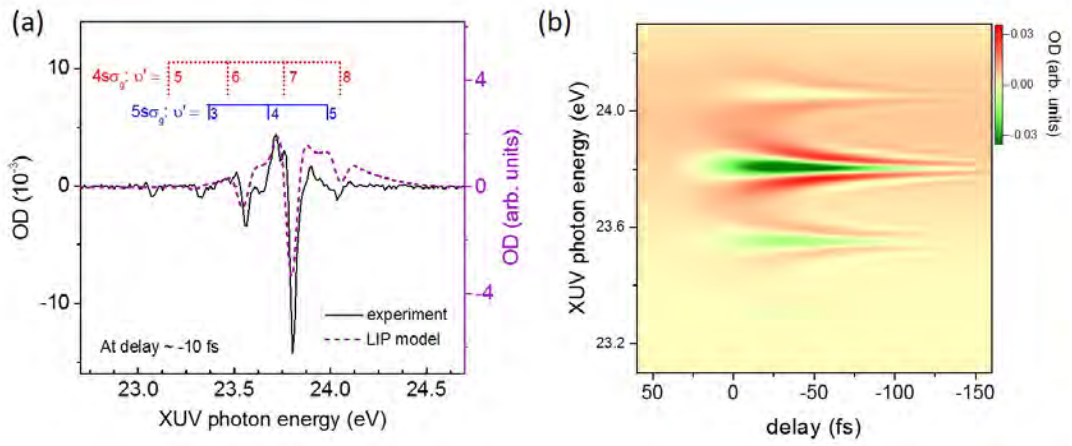

Figure 6.5: (Color online) (a) A comparison of the transient absorption spectra at delay -10 fs from the experiment (solid black curve) and the model (dashed purple curve). (b) The simulated transient absorption spectrogram from the dipole model.

6.4 A Simplified Model and Beyond

Here we employed a simple semiclassical few-level model to simulate the ATAS spectrograms of N_2 Rydberg series in order to better understand our experimental observations. This method is similar to the one used in [141]. Briefly, we assumed that each autoionizing Rydberg state at a given vibrational level can be described as a V-type three-level system as shown in Fig. 6.5(a). These three levels include a ground state, a quasi-bounded metastable state, and a continuum state in the vicinity of the resonance. The D_{gb} and D_{gE} terms are two dipole matrix elements, which couple a ground state to a quasi-bound state or the ground state to a continuum, respectively. The V_{bE} term is the electronic configuration interaction between the quasi-bound and the continuum state by Coulomb interactions. We assumed that the ground state is not appreciably depopulated due to the weak XUV excitation. The expression for the dipole polarization at a given metastable autoionizing state j can be described as

$$\begin{aligned} d^j(t) = \quad & e^{-i\omega_{\mathrm{XUV}}t}\Big[i|D^j_{gb}|^2(1-i/q^j)^2 F_{\mathrm{XUV}}\, G^j(t)\, e^{-\Gamma^j t/2} \\ & + i\pi|D^j_{gE}|^2 F_{\mathrm{XUV}}\, e^{-t^2/\tau^2_{\mathrm{XUV}}} \left(\pi\tau^2_{\mathrm{XUV}}\right)^{-1/2} \Big] + \text{c.c.}, \end{aligned} \tag{6.1}$$

where F_{XUV} is the XUV field amplitude, $\Gamma^j = 2\pi|V_{Eb}^j|^2$ is the absorption line width of the j-th dipole, and τ_{XUV} is the XUV pulse duration. The function to account for the accumulation of the XUV initiated polarization is

$$G^j(t) = \frac{1}{2} e^{(\Gamma^j)^2 \tau_{\mathrm{XUV}}^2/16}[1 + \mathrm{erf}(\Gamma^j \tau_{\mathrm{XUV}}/4 + t/\tau_{\mathrm{XUV}})], \tag{6.2}$$

where erf is the error function that originated from the integration of a Gaussian function.

We simulated the $ns\sigma_g$ states by constructing seven of these dipoles. The central energies of the dipoles are taken from Ref. [232], with a 40 fs lifetime, and the Fano parameter q=2 for all seven states. This construction represents the superimposed $4s\sigma_g(\nu' = 5\text{–}8)$ and $5s\sigma_g$ ($\nu' = 3\text{–}5$) states. The total dipole polarization is $D_{\mathrm{total}}^{\mathrm{XUV}}(t) = \sum_{j=1}^{k} d^j(t)$, where k=7. Note that the lifetime and the Fano q parameters are estimated based on the fitting of the static absorption spectrum in Fig. 6.1.

We also assumed that the role of the NIR pulse is to introduce additional time-depended phase shift $\phi(t, t_d)$ on the dipoles. This laser-induced phase shift can be calculated based on a simple ac Stark phase shift or by a second-order perturbation theory as recently reviewed in [117]. Essentially, this model implies that an autoionizing state will be self-dressed by absorbing and subsequently emitting an NIR photon, without the presence of strongly coupled nearby resonant states by one or two NIR photon transitions. This model is equivalent to the perturbation theory up to the third order, in which we only consider a three-photon process, including an XUV photon and two NIR photons. We recently found that this approach is also suitable for describing the transient absorption spectra in the autoionizing states of O_2 [141]. The NIR laser imposed phase shift can be estimated by calculating Stark energy shift, which is a time-averaged and approximated as a pondermotive energy shift $E_{\mathrm{pon}}(t; t_d)$.

Therefore, the NIR modified total dipole polarization becomes

$$D_{\mathrm{total}}^{\mathrm{NIR+XUV}}(t; t_d) = \sum_{j=1}^{k} d^j(t) e^{i\phi(t,t_d)t} = \sum_{j=1}^{k} d^j(t) e^{\frac{i}{\hbar} E_{\mathrm{pon}}(t;t_d)\, t} \tag{6.3}$$

where we assumed that the pondermotive energy acts evenly on all dipoles. We then calculated the optical density change (OD) due to the presence of NIR field as

$$OD(\omega; t_d) \propto \tilde{D}^{\mathrm{NIR+XUV}}_{\mathrm{total}}(\omega; t_d) - \tilde{D}^{\mathrm{XUV}}_{\mathrm{total}}(\omega), \tag{6.4}$$

where $\tilde{D}^{\mathrm{NIR+XUV}}_{\mathrm{total}}(\omega; t_d)$ and $\tilde{D}^{\mathrm{XUV}}_{\mathrm{total}}(\omega)$ are the Fourier transform of time-dependent total dipole polarization with and without the presence of the NIR field, respectively.

We first do a comparison between a measured transient absorption spectrum (solid black curve) and a simulated one (dashed purple curve) both at -10 fs delay as shown in Fig. 6.5(a). Seven relevant $ns\sigma_g$ Rydberg states are also labeled at the top for reference. We observed that our simulated spectrum qualitatively agrees with the experimentally measured one. However, if we instead use only four $4s\sigma_g$ Rydberg states to construct the total dipole polarization, the resultant spectrum does not match well with the measured spectrum. It implies that in order to capture major spectral features, one has to include the contributions from both $4s\sigma_g$ and $5s\sigma_g$ states, although the latter did not show strong static absorption signals in earlier synchrotron based measurement published in Ref. [14].

The simulated transient absorption spectrogram is shown in Fig. 6.5(b). The spectrogram reproduces many of the characteristics observed in our experimental spectrogram, such as parabolic fringes due to the PFID. However, the increased XUV absorption at the energy range bwtween two subsequent vibrational states can not be produced in this simple model. This implies that other possible states in N_2 influenced by the IR pulse should be taken into account. One of the possible candidates is the NRDES. As we introduced in Sec. 6.2, the NRDES are short-lived neutral dissociative states. These states are expected to have lifetimes lasting from a few femtoseconds to tens of femtoseconds for $^1\Sigma_u^+$ and $^1\Pi_u$ symmetries, respectively [240]. The NRDES states are not included in our current simple dipole model presented here, since they cannot simply be described by a dipole which couples the ground to an excited state and a continuum. In fact, the correct electronic configuration of the NRDES are unsolved [231, 242], and there are four possible assignments for their configurations. We plan to measure time-resolved photoelectron

and photoion spectra with our developing few-cycle NIR pulse to unveil the lifetime and the decaying dynamics of the NRDES in the near future.

6.5 Summary

In summary, we used the ATAS to investigate XUV initiated nitrogen molecular dipole polarization of superexcited states. These states are neutral doubly-excited double-hole Rydberg states converged to excited ionic C-state. The major transient absorption signals we observed can be attributed to the perturbed autoionizing Rydberg states under the influence of a NIR pulse. We also constructed a simple dipole model with pondermotive energy shift imposed by a NIR pulse to explain the main features observed in the experimental spectrograms. However, in additional to known Rydberg states, other short-lived non-Rydberg states could play roles in the observed absorption changes, especially when the XUV and the NIR pulses are overlapped.

CHAPTER 7

The Experiments in Polyatomic Molecules and a Gas Mixture

7.1 The Carbon Dioxide (CO_2) Experiment

7.1.1 Coupled hole-nuclear dynamics near a conical intersection

As we learned from quantum mechanics, for a given Hamiltonian of a system, one can construct the temporal evolution of the system. However, the majority of reaction dynamics in real biochemical systems are not so simple, and they involve, for instance, the couplings of an electronic system to the nuclear motion. These electronic-nuclear couplings can lead to many interesting and important phenomena in photochemical reactions. For example, the photochemical initiation of vision arises from a conformational change [46], which is driven by the electron-nuclear couplings near a conical intersection (CI) between two adiabatic potential energy surfaces. Another example is the relaxation pathway through a CI of a DNA molecule, which provides a protection mechanism from the UV-induced damage [45].

In this Section, we studied the coupled hole-nuclear dynamics in CO_2 molecule. There are three vibrational modes of a linear CO_2 molecule, including a symmetric stretch mode (Q_g), a bending mode (Q_p), and an asymmetric stretch mode (Q_u) as shown in Fig. 7.1(a). These three modes have quantum numbers ν_1, ν_2, and ν_2, with the symmetries of σ_g^+, π_u, and σ_u^+, respectively. The 1D and 2D potential energy surfaces of the excited ionic A-state ($A^2\Pi_u$), B-state ($B^2\Sigma_u^+$), and C-state ($C^2\Sigma_g^+$), which are all above the ground ionic X-state ($X^2\Pi_g^+$), are shown in Fig. 7.1(b) and (c). Note that there is a CI due to the bilinear vibronic coupling between the A-state and the B-state.

In our lab, we conducted experiments to investigate the dynamics in CO_2 driven by the coupled hole-nuclear motion [16]. The schematic sketch of our previous time-resolved photonion experiment using a VMI setup is shown in Fig. 7.2(a). Briefly,

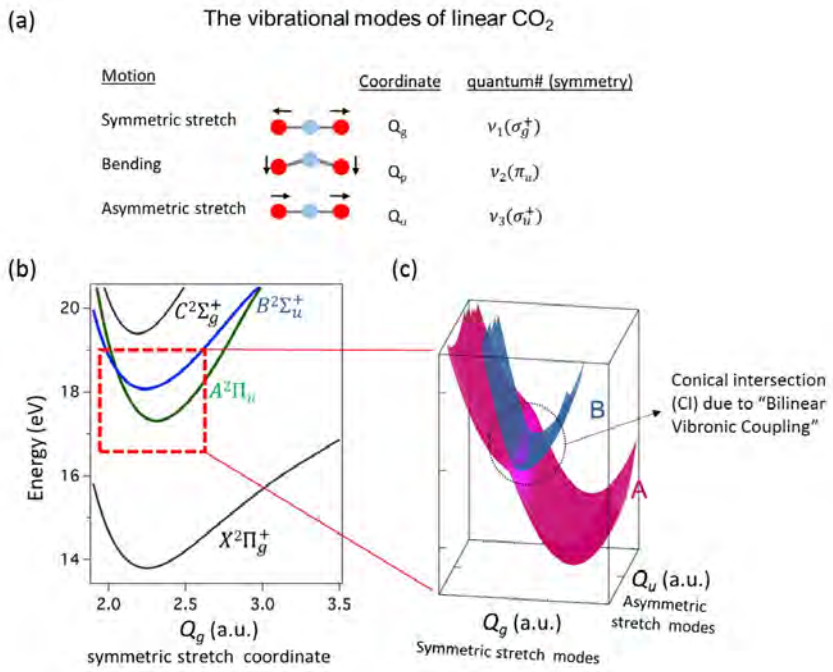

Figure 7.1: (**a**) Three vibrational modes of linear CO_2 molecule. (**b**) The 1D potential energy curves for CO_2 with respect to Q_g coordinate. The ionic A-state ($A^2\Pi_u$) and B-state ($B^2\Sigma_u^+$) intersect at a certain value of Q_g. (**c**) The 2D potential energy surfaces with respect to Q_g and Q_u coordinates. The conical intersection (CI) is due to bilinear vibronic coupling. Figures adapted from Ref. [15].

at delay time zero, the XUV pulse (H11) ionizes a CO_2 molecule, thereby generates a $3\sigma_u$ hole, and so the population is entirely in the excited ionic B-state. The brown color in the calculated molecular orbital represents the probability density of the hole. As the asymmetric stretch and the bending modes become active and start to distort the molecule, a charge population, i.e., the electronic hole, is then driven across the CI to $1\pi_u$ character at delay time $t = \tau$. When the population is in the A-state, it is no longer accessible by the probing IR pulse, resulting in a reduction of CO^+ ion signal detected by the VMI. Therefore, the oscillations in the CO^+ ion yield at a 115 fs cycle perfectly reflect the coherent beating between σ and π character as shown in Fig. 7.2(b).

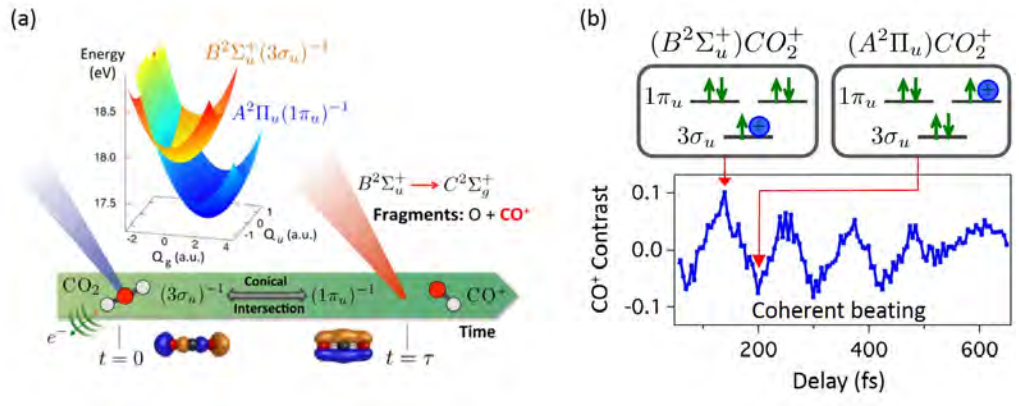

Figure 7.2: (**a**) The schematic sketch shows the process of the coupled hole-nuclear dynamics in CO_2. The distorted molecule due to the active stretching and bending modes, which drive the charge population across the conical intersection. (**b**) (Top) The electronic configurations of ionic B-state and A-state. The green arrows are electrons, and the blue circles are holes. (Bottom) The 115 fs coherent beating signal from CO^+ ion yield. Reprinted figure with permission from Ref. [16]. Copyright 2017 by the American Physical Society.

7.1.2 The Rydberg series in CO_2

In my recent experiments, the ATAS is used to study the same system as introduced in the previous section. However, what kind of new information can the ATAS provide is still under investigation. As we learned from N_2 experiments that the photoabsorption spectra are only sensitive to the neutral states, but not the excited ionic states. Also, each excited ionic state has a neutral Rydberg series converged onto it, and these Rydberg series could exhibit their own CIs. Therefore, it is possible to probe their hole-nuclear dynamics. Therefore, the goal of this study is to understand how does Rydberg electrons respond to the distorted molecule driven by nuclear motion.

We first examined the known Rydberg states converged to the A-, B-, and C-states. Early studies show that there are many Rydberg states converged to each of the excited ionic states as partly shown in Fig. 7.3. For the A-state, the Rydberg series is named Tanaka-Ogawa series [20], and it has the electronic configuration $1\pi_u^{-1}\, nd\delta_g\ (^1\Pi_u)$ ($\nu_1 = 0$–7). As for the B-state, the Rydberg series is called Henning

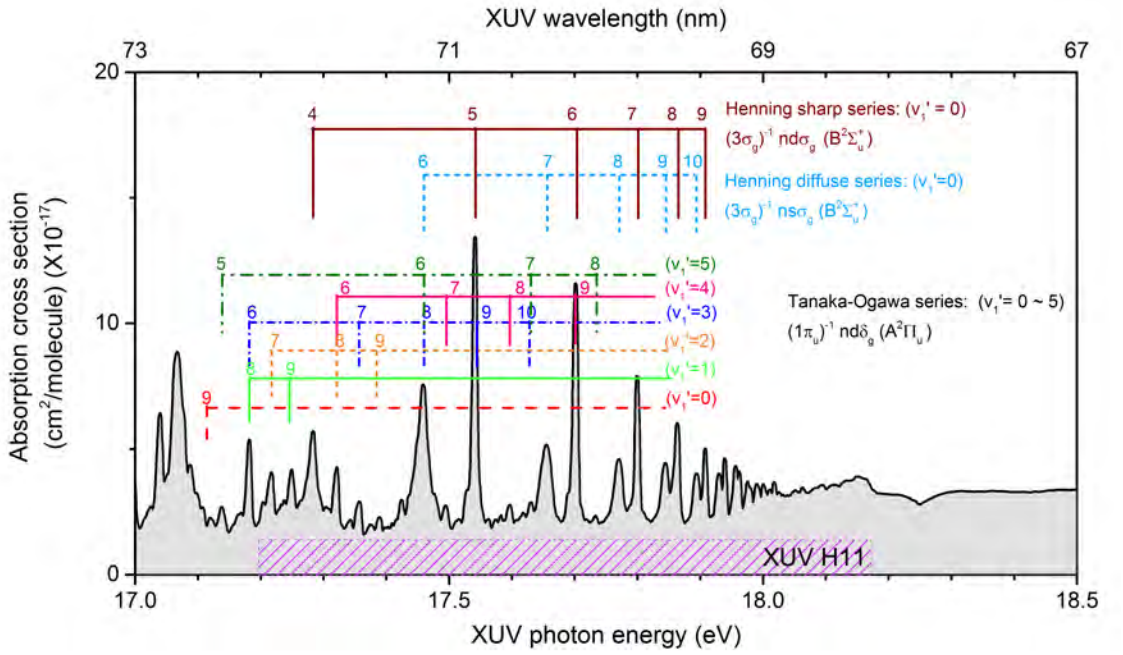

Figure 7.3: The measured static photoabsorption cross section adapted from Shaw *et al.* [17] and Huestis *et al.* [18]. The assignments of the Rydberg states converged to the A-state (Tanaka-Ogawa series) and the B-state (Henning series) are taken from Ref. [19–22]. The shaded purple box represents the spectral range of our XUV H11.

series [19], which includes the electronic configuration $3\sigma_u^{-1}\ ns\sigma_g\ (^1\Sigma_u^+)$ as a sharp series, and the electronic configuration $3\sigma_u^{-1}\ nd\sigma_g\ ^1\Sigma_u^+$ as a diffuse series. For the C-state, the three Rydberg series are termed the 'a' (absorption), 'w' (weak), and 'e' (emission) series. Their electronic configurations are $4\sigma_g^{-1}\ np\pi_u\ (\Pi_u)$, $4\sigma_g^{-1}\ nd\pi_u$ (Π_u), and $4\sigma_g^{-1}\ np\sigma_u\ (^1\Sigma_u^+)$, respectively. All of these states are summarized and organized in Ref. [21, 22].

Figure 7.3 also shows the measured static XUV photoabsorption spectrum, adapted from Shaw *et al.* [17] and Huestis *et al.* [18]. The spectral range of our XUV H11 is also shown in the figure, with the relevant Rydberg states labeled at the top, which include a portion of the Rydberg series in the A-state and the B-state. We can see that the strong absorption peaks come from ndσ_g and nsσ_g series of the B-state, which show many pairs of features as we observed before in O_2 Rydberg

series in Chapter 4. There are some weaker absorption peaks which stems from ndδ_g series of the A-state. In contrast to the Rydberg series in the A-state that includes the ground vibrational level only, the Rydberg series in the B-state have many vibrational progressions, including ν_1'=1–5.

7.1.3 Investigating the Hole-nuclear dynamics by the ATAS

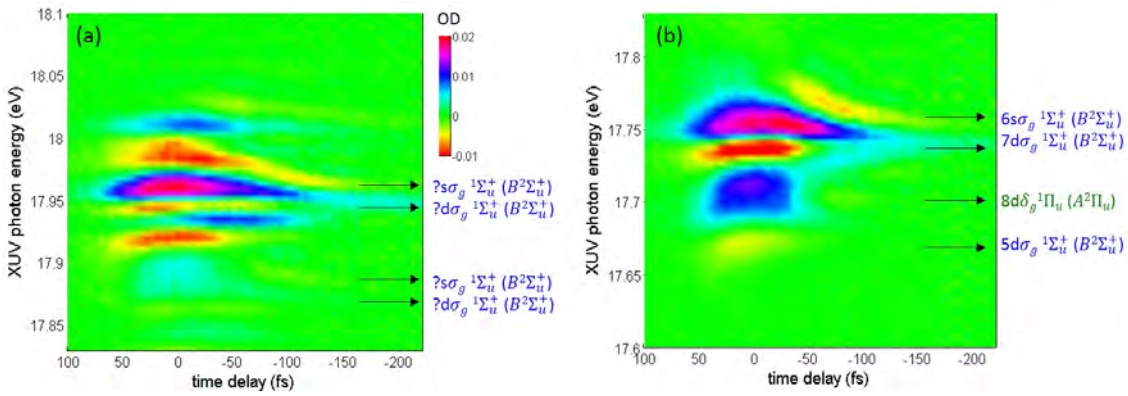

Figure 7.4: The ATAS spectrogrms of CO_2 with the IR photon energy at 0.76 eV (1630 nm). The XUV spectrum was turned to excite higher and lower energy Rydberg states in Fig.(**a**) and (**b**), respectively.

We recently conducted an ATAS experiment on CO_2 by monitoring the XUV H11. The IR pulses in the experiment are generated by an OPA and it has a tunable range from 0.76 eV (1630 nm) to 0.954 eV (1300 nm). Figure 7.4 shows our preliminary data of the CO_2 spectrograms with 0.76 eV IR photon energy and $\sim$1 TW/cm^2 IR peak intensity. The XUV spectra are tuned to excite higher energy states as in Fig. 7.4(a), and lower energy states as in Fig. 7.4(b). The tentative state assignments are labeled on the side. We observed that both ndσ_g and nsσ_g states show evolutions that are similar the experiments of O_2 and N_2. For instance, they exhibit common features of the PFID with parabolic structures. However, the dynamics of the 8dδ_g state show a very different relaxation lifetime. It seems that the OD signal at 8dδ_g state is truncated abruptly without a smoothed PFID feature. In addition, some features in Fig. 7.4(a) show delayed positive OD signal such as those at $\sim$17.93 ev, while other features with negative OD signal do not

show delayed signals. More detailed experiments and theoretical works are needed to resolve and understand what we have observed so far by monitoring the XUV transient absorption signals in this complex system.

7.2 The Sulfur Hexafluoride (SF_6) Experiment

(This section is adapted from C.-T. Liao *et al.*, "XUV Transient Absorption Spectroscopy: Probing Laser-Perturbed Dipole Polarization in Single Atom, Macroscopic, and Molecular Regimes.", Photonics 2017, 4(1), 17, as in Ref. [7].)

In this section, we demonstrated an application of the ATAS to investigate the polyatomic Sulfur Hexafluoride (SF_6) molecule that exhibits octahedral geometry. The SF_6 has been the focus of recent investigations that probed the ultrafast vibrational modes and shape resonances through the study of its photoelectron spectrum and HHG spectrum [243, 244], as well as the light-induced chemical reactions at sulfur L-edges by soft X-ray transient absorption [245].

Figure 7.5a shows a schematic of the effective molecular potential of SF_6 adapted from Ref. [23], where the radial distance is shown for illustrative purposes only. The excited state potential is partitioned into an inner well and an outer well. Inside the inner well, there are many virtual valence orbitals in which shape resonances have been identified. The assignments of these resonances embedded in the ionization continuum have been under debate because of the ambiguity in the ordering of valence orbitals [246, 247]. Here, we adopt accepted orbital configuration $4t_{1u}^6 t_{12g}^6 3e_g^4 (5t_{2u}^6 + 1t_{2u}^6) 6t_{1g}^6$. It is known that the photoabsorption cross section of SF_6 is unusual, in that the most prominent features are due to the inter-valence transitions, whereas Rydberg series are strongly suppressed in a few eV ranges [247, 248].

The absolute photoabsorption cross section in XUV range has been measured by Holland et al. [24] using a synchrotron source and is shown in Figure 7.5b. The H15 excites one of the most intense features in the inner well peaked around 23.5 eV, which could be attributed to two shape resonance enhanced inter-valence tran-

sitions [249, 250]. The first one is $5a_{1g} \rightarrow 6t_{1u}$, which is correlated with the 3s and 3p orbitals, and the second one is $5t_{1u} \rightarrow 2t_{2g}$, which arises from the fluorine $2p\pi$ orbitals and the sulfur 3d orbitals, respectively [23]. These two possible photoexcitation pathways are indicated by purple arrows in Figure 7.5a. However, it was suggested based on ab initio calculation that the first transition, $5a_{1g} \rightarrow 6t_{1u}$, is expected to be much stronger in its oscillator strength [23, 251].

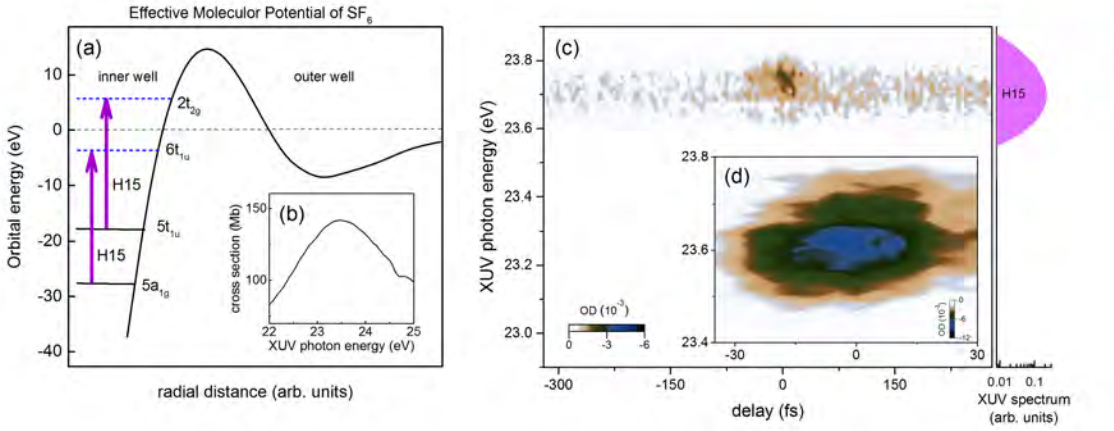

Figure 7.5: (**a**) a schematic effective molecular potential of SF_6 adapted from [23]. Dashed (solid) horizontal lines indicate vacant (occupied) virtual orbitals. Two purple arrows indicate two possible inter-valence photoexcitation pathways by H15. (**b**) Total photoabsorption cross section adapted from Ref. [24]; (**c**) our experimental transient absorption spectrogram in SF_6. The XUV spectrum of H15 is also shown on the side for reference; and (**d**) the transient absorption spectrogram of SF_6 near delay zero taken with smaller delay step size.

Similar to the experimental scheme used in previous sections, our XUV pulse first impulsively excites the superpositions of molecular polarizations corresponding to $5a_{1g} \rightarrow 6t_{1u}$ and/or $5t_{1u} \rightarrow 2t_{2g}$ transitions. A subsequent NIR pulse is applied to perturb these dipole polarizations. The NIR pulse used here has its wavelength centered at 780 nm with peak intensity at 1 ($\pm$0.5) TW/cm^2, and the SF_6 target gas cell has backing pressure 267 Pa. The measured transient absorption spectrogram of SF_6 is shown in Figure 7.5c. Unlike the ATAS spectrogram of helium, here we only observe the change in OD around delay zero, indicating short-lived molecular

polarization. A different set of data taken near delay zero with smaller delay step (5 fs) is shown in Figure 7.5d. This transient OD signal's spectral width is limited by the XUV bandwidth, as the broad static absorption feature shown in the inset of Figure 7.5c is wider than the H15 bandwidth shown on the right side of the figure. We note that, at H13 or H17 energies, we did not observe any transient signal within the detection limits of our method.

In the presence of strong-field NIR, only negative OD is observed in our experiment, which implies that the static XUV absorption is suppressed. Since the initial state is tightly bound, we believe the laser-induced modification of the final states is responsible for causing this effect. Considering the complexity of these shape resonance enhanced inter-valence transitions, the exact physical mechanism of this absorption suppression on these excited states due to NIR pulse is still unclear. In contrast to the study of atomic polarization and relatively simple diatomic polarization in previous ATAS studies, neither the laser-induced phase model nor the laser induced attenuation model [141] is sufficient to give us physical insight on this complex molecular system. More experimental and theoretical investigations are needed to fully understand these observations. The study of SF_6 serves as a starting point for future studies on complex molecular systems, in which the excited state dynamics resulting from electronic and nuclear motions can be resolved.

7.3 The Helium-Neon (He-Ne) Mixture Experiment

7.3.1 The working principle of a He-Ne laser

As the first gas laser invented in the world, the first He-Ne laser was built at Bell Labs in 1690 and it emitted IR radiation at wavelength 1150 nm. Later in 1962, the highest gain in the visible wavelength 633 nm emission was identified and implemented [252, 253]. The energy level diagram of the He-Ne mixture is shown in Fig. 7.6(a). The electron population of helium is first excited by a dc or radio-frequency discharge, in which the electron impact collision and excitation happens. The ground state electrons in helium are excited to 2s triplet and 2s singlet excited

states at ∼20.5 eV and ∼19.7 eV, respectively. After the He-Ne collision process, the population inversions are achieved by the excitation transfer from helium 2s metastable states to neon 4s and 5s states. In this process, helium metastable states are used as the energy carriers to excite other levels of neon to get an efficient and equivalent three-level system for the lasing process. In Fig. 7.6(a), neon levels are shown in extended gray box because of many LS-coupling induced sub-levels. The de-excitation pathways for lasing are $5s_2 \rightarrow 4p$ (3.39 μm), $5s_2 \rightarrow 3p_4$ (632.8 nm), and $4s_2 \rightarrow 3p_4$ (1.15 μm). The reaction equations are

$$He^*(2^3S_1) + Ne^1S_0 \rightarrow He(^1S_0) + Ne^*4s_2 + \Delta E, \tag{7.1}$$

$$He^*(2^1S_1) + Ne^1S_0 + \Delta E \rightarrow He(^1S_0) + Ne^*5s_2, \tag{7.2}$$

where ΔE is the small energy mismatch (∼50 meV) between two atoms supplied by kinetic energy. After the lasing transitions, there are many non-radiative transitions and spontaneous emission transitions that bring excited electrons back to the ground state. In a typical He-Ne laser, the partial or molar pressure ratio of the mixture is He:Ne = 7:1∼10:1 at 1–3 torr total pressure.

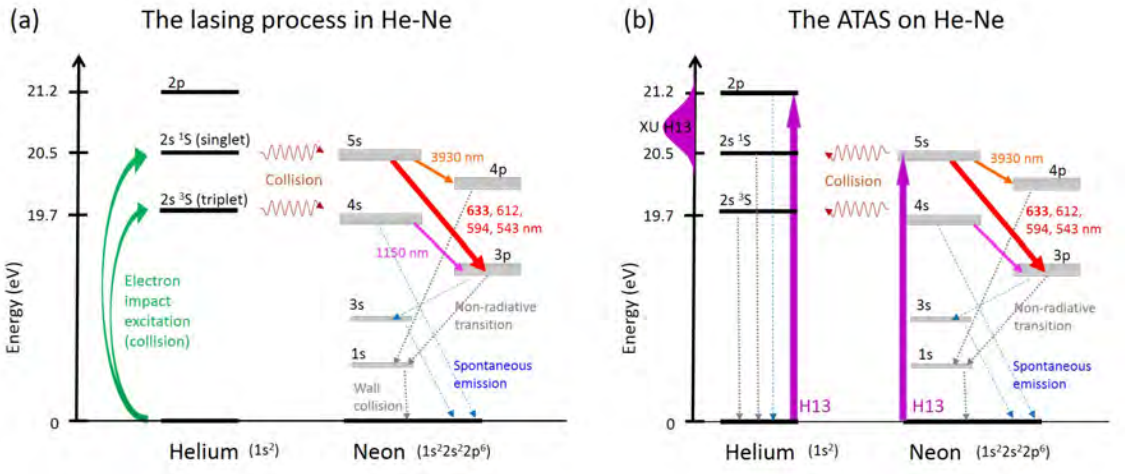

Figure 7.6: (**a**) A simplified schematic energy level diagram of the lasing process in He-Ne mixture. (**b**) A schematic energy level diagram of the ATAS experiment of He-Ne mixture using XUV H13 to prepare neon 5s state.

7.3.2 The collision-induced absorption and dipoles

The forbidden optical transition enabled by the interacting atoms or molecules in gases and liquids is termed the collision-induced spectroscopy [254]. The majority of this kind of spectroscopic measurement are conducted in the far-IR region, which plays important roles in planetary and atmospheric sciences. The main effects due to the collision are induced light absorption and induced light scattering in the spectral range of the IR and visible, respectively. The induced optical absorption stems from the distortion in the distribution of the bound electrons during the collision between two nonpolar atoms or molecules [255]. Also, the collision-induced dipole moment or the collision-induced polarizability only appears within the duration of the collision process for dissimilar atoms. This duration can be calculated by the relaxation time, τ_{re}, associated with collisions [256, 257]. This duration reads

$$\tau_{re} = \frac{3\pi b}{28}(\frac{2\pi m_r}{kT})^{1/2}, \tag{7.3}$$

where b is the collision diameter, i.e., the impact factor, m_r is the reduced mass, and T is the temperature. The theoretical relaxation time of He-Ne mixture at room temparature (T= 295 K) is 40.5 fs [258].

The collision process induces dipoles or polarizability. The induced dipole moments from inert gas mixtures are recently summarized in Ref. [259], including the He-Ne mixture in the far-IR region. As for the higher photon energy region, the inelastic collision process leads to the energy transfer between metastable and ground state species, which is an important process to understand plasma discharge and laser-plasma interactions. After the thermal collision between metastable and ground state species, the stored energy from metastable species can lead to many phenomena such as the collision-induced radiative deexcitation, fine-structure transitions, and the chemi-ionization [260]. In the vacuum-UV region, microsecond time-resolved emissions from He-Ne mixtures was measured [261].

7.3.3 What can we learn from the ATAS on He-Ne mixture?

We have acquired some preliminary measurement on the He-Ne mixture as shown in Fig. 7.7, where (a) is a spectrogram of a He-Ne mixture, (b) is a helium spectrogram, and (c) is a neon spectrogram. In Fig. 7.7(b), we observed familiar OD change on helium 1s2p state. In Fig. 7.7(c), the spectrogram shows many neon excited states as recently reported in Ref. [262, 263]. Without any collision or interaction process in a He-Ne mixture, we expect to observe a superimposed spectrogram from helium only and neon only spectrograms. However, as we can see in Fig. 7.7(a), there are some small but significant spectral features different from helium and neon only spectrograms, especially for the new structures near 20.5 eV where the collision-induced energy transfer could take place.

More experimental verification and replication are needed to confirm our preliminary findings on the new features in the He-Ne mixture. In addition, theoretical calculation and modeling are needed to understand and interpret our observations of this collision-induced transient absorption experiment. In short, these new spectral features in the He-Ne spectrogram could be the signature manifested by the ultrafast He-Ne collision process.

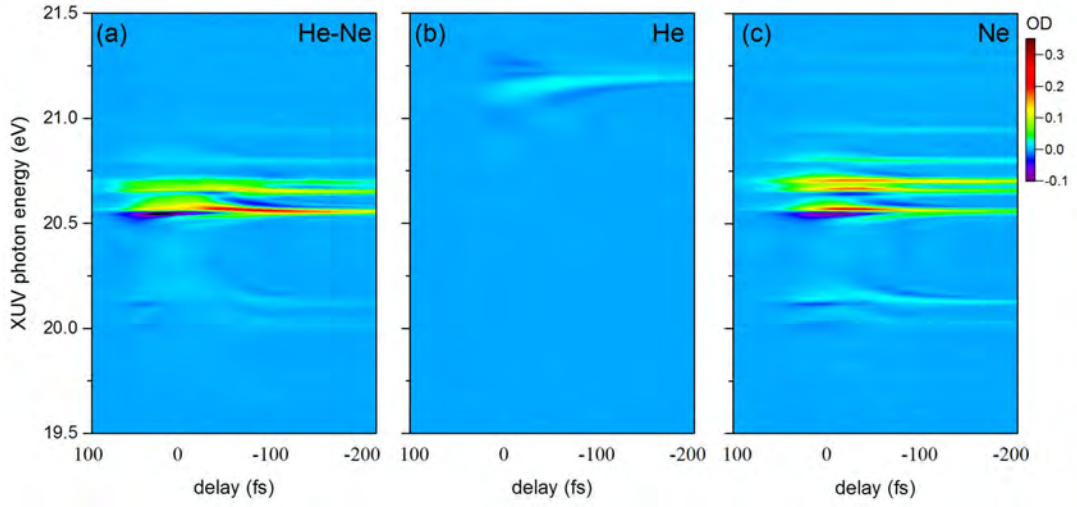

Figure 7.7: A preliminary data showing the He-Ne spectrogram (**a**), the He spectrogram (**b**), and the Ne spectrogram (**c**). The IR photon energy is 0.76 eV (1630 nm) and the peak intensity is $\sim$1 TW/cm^2.

CHAPTER 8

Conclusion

In my dissertation, the research goal is to understand the temporal evolution of highly excited atoms and molecules by perturbing the excited electronic states with light. The recently developed ultrafast spectroscopic technique–the XUV attosecond transient absorption spectroscopy–was utilized to investigate the charge dynamics on the timescale of tens of femtoseconds to hundreds of attoseconds. The systems under investigation, i.e., the excited atomic or molecular gases, were first excited by XUV attosecond pulses to prepare coherent superposition of excited bounded or metastable states. Then, a subsequent and phase-locked IR femtosecond pulse with a controllable wavelength, intensity, and field polarization, was introduced to perturb the systems under investigation while the delay-dependent change in the XUV spectrum was monitored. The perturbation from the strong-field IR pulse induces many transient effects, such as multi-photon coupling to nearby states and energy shifting/splitting/broadening. These excited or super-excited states in atoms and molecules can be considered as atomic or molecular polarization, which in the semi-classical picture refers to the collection of electric dipoles. We experimentally investigated the dynamics of these dipoles in He, Ar, O_2, N_2, CO_2, and SF_6.

In the He experiments as described in Chapter 3, we studied and quantified the time-dependence of various transient phenomena, including ac Stark shift, laser-induced phase, quantum path interference, and laser-induced continuum structure in 1snp Rydberg states of dilute helium gas. These phenomena can be understood under the single-atom response assumption. In the case of dense helium targets, we found that specific new spectral features in the absorption profile, and their evolution with propagation distance, can be attributed to the interplay between resonant XUV attosecond pulse propagation and IR-imposed quantum phase shifts in an optically thick medium. Our joint experimental-theoretical studies show that

this interplay manifests itself in the time domain, with the IR pulse influencing the reshaping of the XUV pulse transmitting through the resonant medium. As the optical depth increases, this nonlinear macroscopic interplay initially leads to a broadening of the IR modified absorption line, and subsequently to the appearance of new and narrow frequency domain features in the spectrum. We also developed a unified physical picture to account for all scenarios and an application guideline to consider the dense gas limit, which shows nonlinear effects.

In the O_2 experiments as described in Chapter 4, we studied the autoionizing states of oxygen in electronically and vibrationally resolved fashion. The observed transient absorption spectra showed opposite OD changes from states with different electron state symmetry. In the case of the $ns\sigma_g$ (and $nd\pi_g$) series, the OD changes are positive, while in the case of the $nd\sigma_g$ series, the OD changes are negative. The *ab initio* MCTDHF calculation was also implemented, and it agrees with our experimental findings. We also modeled the effect of IR perturbation on the molecular polarization of oxygen by two common approaches, namely the laser-induced phase shift model and the laser-induced attenuation model. We found that only the former agrees with both experimental and calculated results. On these grounds, we relate the state symmetry dependent sign of the absorption change to the Fano parameters of the static absorption line shapes.

In the argon experiments as described in Chapter 5, we investigated the possibility of controlling a Fano interferometer, which is an intrinsic electron wave packets interferometer occurring in an autoionizing state. We applied an external IR laser to control argon autoionizing 4p states by manipulating the polarization of the IR field from linear, either parallel or perpendicular to the XUV field, to circular polarization. We observed significantly modified spectral line shape transition from Lorentzian-like (Breit-Wigner-like) to Fano-like profiles. This study demonstrates the feasibility of using an external field to control a Fano interferometer of autoionization.

In the N_2 experiments as described in Chapter 6, we observed the relaxation dynamics of the XUV initiated nitrogen molecular dipole polarization of doubly-

excited vibrational progressions. We identified that the transient absorption spectrum is only sensitive to neutral Rydberg states, despite the complicated potential energy curves in this spectral range. We also constructed a laser-induced phase shift model and applied it to the superimposed seven vibrational states to understand the main features observed in the spectrograms. However, other short-lived non-Rydberg states could play roles in the observed OD change, especially if the XUV and IR pulses are overlapped.

In Chapter 7, we studied three different complicated systems, namely, CO_2, SF_6 and He-Ne mixture. These systems are beyond simple atomic and diatomic molecular gasses. The aim of the CO_2 study is to deepen our understanding of the charge dynamics near a conical intersection of the potential energy surfaces. Our preliminary measurement of the transient absorption of CO_2 is sensitive to many neutral Rydberg series converged to excited ionic states, which could exhibit coupled hole-nuclear driven dynamics in distorted molecules. In the SF_6 experiments, we observed the suppression of XUV photoabsorption that corresponds to the inter-valence transitions in the presence of a strong IR field. Lastly, the transient absorption characteristics of He-Ne mixture were investigated. Our preliminary data shows spectral features that cannot be explained by the linear superimposition of He and Ne spectrograms. These new features could be the signature manifested by the He-Ne collision process, which is related to the lasing mechanisms behind He-Ne lasers.

One of the goals of our planned research along this direction is to produce few-pulse broadband XUV continuum in conjunction with strong, robust, and tunable few-cycle IR pulses. With improved and upgraded light sources, we can then study charge dynamics in complex molecular and solid-state systems in 1D and 2D pump-probe geometries. As the glue that bonds atoms in complex chemical systems, electrons and their dynamical behavior governs chemical reactions. Therefore, a greater understanding of those phenomena is a key to steer chemical reactions on-demand in the industry, and to design and manufacture highly efficient energy devices [264]. As for the application to solid-state systems, we can also apply this ultrafast XUV

spectroscopic technique to explore semiconductors [265] and emerging 2D quantum materials [266]. This could then spur a revolution in ultrafast communication and computation by utilizing the light-wave technology in matter [267, 268]. In conclusion, the use of the transient absorption spectroscopy with XUV attosecond pulses have unveiled many ephemeral light-induced phenomena of excited atoms and molecules, which were probed, dressed, or modified through the interaction of a strong-field femtosecond IR pulse and the target medium. These studies shed light on the electronic processes, and deepen our insight of these processes in the time-domain perspective.

APPENDIX A

Abbreviation List

2DSI two-dimensional spectral shearing interferometry

ADK Ammosov-Delone-Krainov

APTs attosecond pulse trains

ASE amplified spontaneous emission

ATA attosecond transient absorption

ATAS attosecond transient absorption spectroscopy

BBO beta barium borate

CCD charge-coupled device

CI conical intersection

cw continuous wave

EPA electric dipole approximation

FID free induction decay

FROG frequency-resolved optical gating

FWHM full width at half maximum

FWHM full width at half maximum

FWM Four-wave mixing

GDD group velocity dispersion

GOD double optical gating

GVD group velocity dispersion

H13 13th harmonics

H15 15th harmonics

H17 17th harmonics

HCF holow-core fiber

HHG high harmonic generation

IAP isolated attosecond pulse

IR infrared

LIA laser-induced attenuation

LICS laser-induced continuum structure

LIP laser-induced phase

MCP microchannel plate

MCTDHF multiconfiguration time-dependent Hartree-Fock

MIR mid-infrared

mOD milli-optical density

MPI multi-photon ionization

MWE Maxwell wave equation

NIR near infrared

NRDES non-Rydberg doubly excited states

o.c. optical cycles

OD optical density

OPA optical parametric amplifier

PFID perturbed free induction decay

RABBIT reconstruction of atosecond beating by interference of two-photon transition

RPP resonant pulse propagation

SHG second harmonic generation

SIGC semi-infinite gas cell

SPIDER spectral phase interferometry for direct electric-field reconstruction

SPM self-phase modulation

TDSE time-dependent Schrödinger equation

TTL Transistor-transistor logic

UV ultraviolet

XUV extreme ultraviolet

APPENDIX B

List of Publications

1. **Chen-Ting Liao**, Coleman Cariker, Nathan Harkema, Luca Argenti, and Arvinder Sandhu. "Ultrafast laser control of autoionizing resonances in argon observed in attosecond transient absorption." In preparation (2017).

2. Nathan Harkema, **Chen-Ting Liao**, Arvinder Sandhu, Seth Camp, Kenneth J. Schafer, and Mette B. Gaarde. "Controlling electronic couplings with tunable long wavelength pulses: Study of Autler-Townes splitting and XUV emission spectra." In preparation (2017).

3. **Chen-Ting Liao**, Xuan Li, Daniel J. Haxton, Thomas N. Rescigno, Robert R. Lucchese, C. William McCurdy, and Arvinder Sandhu, "Probing autoionizing states of molecular oxygen with XUV transient absorption: Electronic-symmetry-dependent line shapes and laser-induced modifications." *Physical Review A* **95**, 043427(2017)

4. **Chen-Ting Liao** and Arvinder Sandhu. "XUV Transient Absorption Spectroscopy: Probing Laser-Perturbed Dipole Polarization in Single Atom, Macroscopic, and Molecular Regimes." *Photonics*, 4(1), 17 (2017).

5. **Chen-Ting Liao**, Arvinder Sandhu, Seth Camp, Kenneth J. Schafer, and Mette B. Gaarde. "Attosecond transient absorption in dense gases: Exploring the interplay between resonant pulse propagation and laser-induced line-shape control." *Physical Review A* **93**, 033405 (2016).

6. **Chen-Ting Liao**, Arvinder Sandhu, Seth Camp, Kenneth J. Schafer, and Mette B. Gaarde. "Beyond the single-atom response in absorption line shapes: probing a dense, laser-dressed helium gas with attosecond pulse trains." *Physical Review Letters* **114**, 143002 (2015).

REFERENCES

[1] J. Stöhr. *NEXAFS spectroscopy*, volume 25. Springer-Verlag Berlin (1992).

[2] T. Brabec and H. Kapteyn. *Strong field laser physics*, volume 134. Springer (2008).

[3] M. Gavrila. *Atoms in intense laser fields*. Academic Press Inc. (1992).

[4] H. Reiss. Limits on tunneling theories of strong-field ionization. *Physical Review Letters* **101**(4) 043002 (2008).

[5] H. R. Reiss. Theoretical methods in quantum optics: S-matrix and keldysh techniques for strong-field processes. *Progress in Quantum electronics* **16**(1) 1–71 (1992).

[6] S. L. Chin. *Multiphoton lonization of Atoms*. Elsevier (2012).

[7] C.-T. Liao and A. Sandhu. XUV transient absorption spectroscopy: Probing laser-perturbed dipole polarization in single atom, macroscopic, and molecular regimes. *Photonics* **4**(17) (2017).

[8] N. Shivaram, H. Timmers, X.-M. Tong, *et al.*. Attosecond-resolved evolution of a laser-dressed helium atom: Interfering excitation paths and quantum phases. *Physical Review Letter* **108** 193002 (2012).

[9] D. Holland, D. Shaw, S. McSweeney, *et al.*. A study of the absolute photoabsorption, photoionization and photodissociation cross sections and the photoionization quantum efficiency of oxygen from the ionization threshold to 490 å. *Chemical Physics* **173**(2) 315–331 (1993).

[10] P. V. Demekhin, D. Omelyanenko, B. Lagutin, *et al.*. Investigation of photoionization and photodissociation of an oxygen molecule by the method of coupled differential equations. *Optics and spectroscopy* **102**(3) 318–329 (2007).

[11] J. Berkowitz. *Atomic and molecular photoabsorption: absolute total cross sections*. Academic Press (2002).

[12] J.-I. Lo, M.-H. Tsai, H.-S. Fung, *et al.*. Observation of new Rydberg series in the many-electron transition region of N_2. *The Journal of chemical physics* **137**(5) 054315 (2012).

[13] A. J. Yencha, K. Ellis, and G. C. King. High-resolution threshold photoelectron and photoion spectroscopy of molecular nitrogen in the 15.0–52.7 ev photon energy range. *Journal of Electron Spectroscopy and Related Phenomena* **195** 160–173 (2014).

[14] P. Gürtler, V. Saile, and E. Koch. High resolution absorption spectrum of nitrogen in the vacuum ultraviolet. *Chemical Physics Letters* **48**(2) 245–250 (1977).

[15] H. R. Timmers. *Ultrafast XUV Spectroscopy: Unveiling the Nature of Electronic Couplings in Molecular Dynamics*. Ph.D. thesis, The University of Arizona. (2014).

[16] H. Timmers, Z. Li, N. Shivaram, *et al.*. Coherent electron hole dynamics near a conical intersection. *Physical Review Letter* **113** 113003 (2014).

[17] D. Shaw, D. Holland, M. Hayes, *et al.*. A study of the absolute photoabsorption, photoionisation and photodissociation cross sections and the photoionisation quantum efficiency of carbon dioxide from the ionisation threshold to 345 å. *Chemical physics* **198**(3) 381–396 (1995).

[18] D. L. Huestis and J. Berkowitz. Critical evaluation of the photoabsorption cross section of CO_2 from 0.125 to 201.6 nm at room temperature. *Planetary Science, Advances in Geosciences* **25** 229–242 (2011).

[19] H. J. Henning. Die absorptionsspektren von kohlendioxyd, kohlenmonoxyd und wasserdampf im gebiet von 600–900 å. *Annalen der Physik* **405**(5) 599–620 (1932).

[20] Y. Tanaka and M. Ogawa. Rydberg absorption series of CO_2 converging to the $^2\Pi_u$ state of CO_2^+. *Canadian Journal of Physics* **40**(7) 879–886 (1962).

[21] G. Cook, P. Metzger, and M. Ogawa. Absorption, photoionization, and fluorescence of CO_2. *The Journal of Chemical Physics* **44**(8) 2935–2942 (1966).

[22] L. Berg, A. Karawajczyk, and C. Stromholm. Synchrotron radiation study of photoionization and photodissociation processes of CO_2 in the 13-21 ev region. *Journal of Physics B: Atomic, Molecular and Optical Physics* **27**(14) 2971 (1994).

[23] K. Mitsuke, S. Suzuki, T. Imamura, *et al.*. Negative-ion mass spectrometric study of ion-pair formation in the vacuum ultraviolet. iii. *The Journal of Chemical Physics* **93**(12) 8717–8724 (1990).

[24] D. Holland, D. Shaw, A. Hopkirk, *et al.*. A study of the absolute photoabsorption cross section and the photoionization quantum efficiency of sulphur hexafluoride from the ionization threshold to 420 å. *Journal of Physics B: Atomic, Molecular and Optical Physics* **25**(22) 4823 (1992).

[25] W. E. Soothill and L. Hodous. *A dictionary of Chinese Buddhist terms: with Sanskrit and English equivalents and a Sanskrit-Pali index*. Motilal Banarsidass Publ. (1937).

[26] F. McClung and R. Hellwarth. Giant optical pulsations from ruby. *Journal of Applied Physics* **33**(3) 828–829 (1962).

[27] A. DeMaria, D. Stetser, and H. Heynau. Self mode-locking of lasers with saturable absorbers. *Applied Physics Letters* **8**(7) 174–176 (1966).

[28] C. Shank and E. Ippen. Subpicosecond kilowatt pulses from a mode-locked cw dye laser. *Applied Physics Letters* **24**(8) 373–375 (1974).

[29] E. Ippen and C. Shank. Techniques for measurement. In *Ultrashort light pulses*, 83–122. Springer (1977).

[30] A. H. Zewail. Femtochemistry: Atomic-scale dynamics of the chemical bond. *The Journal of Physical Chemistry A* **104**(24) 5660–5694 (2000).

[31] A. Dubietis, G. Jonušauskas, and A. Piskarskas. Powerful femtosecond pulse generation by chirped and stretched pulse parametric amplification in bbo crystal. *Optics Communications* **88**(4-6) 437–440 (1992).

[32] T. Brabec and F. Krausz. Intense few-cycle laser fields: Frontiers of nonlinear optics. *Reviews of Modern Physics* **72**(2) 545 (2000).

[33] J. L. Krause, K. J. Schafer, and K. C. Kulander. High-order harmonic generation from atoms and ions in the high intensity regime. *Physical Review Letters* **68**(24) 3535 (1992).

[34] P. B. Corkum. Plasma perspective on strong field multiphoton ionization. *Physical Review Letters* **71**(13) 1994 (1993).

[35] T. Udem, R. Holzwarth, and T. W. Hänsch. Optical frequency metrology. *Nature* **416**(6877) 233–237 (2002).

[36] M. Hentschel, R. Kienberger, C. Spielmann, *et al.*. Attosecond metrology. *Nature* **414**(6863) 509–513 (2001).

[37] M. Vrakking. *Attosecond and XUV Physics: Ultrafast Dynamics and Spectroscopy*. Wiley Online Library (2014).

[38] F. Lépine, M. Y. Ivanov, and M. J. Vrakking. Attosecond molecular dynamics: fact or fiction? *Nature Photonics* **8**(3) 195–204 (2014).

[39] Z. Chang. *Fundamentals of attosecond optics*. CRC Press (2016).

[40] M. T. Hassan, A. Wirth, I. Grguraš, *et al.*. Invited article: Attosecond photonics: Synthesis and control of light transients. *Review of Scientific Instruments* **83**(11) 111301 (2012).

[41] H. Fattahi, H. G. Barros, M. Gorjan, *et al.*. Third-generation femtosecond technology. *Optica* **1**(1) 45–63 (2014).

[42] A. Vaupel, N. Bodnar, B. Webb, *et al.*. Concepts, performance review, and prospects of table-top, few-cycle optical parametric chirped-pulse amplification. *Optical Engineering* **53**(5) 051507–051507 (2014).

[43] D. T. Reid, C. M. Heyl, R. R. Thomson, *et al.*. Roadmap on ultrafast optics. *Journal of Optics* **18**(9) 093006 (2016).

[44] T. Brixner, J. Stenger, H. M. Vaswani, *et al.*. Two-dimensional spectroscopy of electronic couplings in photosynthesis. *Nature* **434**(7033) 625–628 (2005).

[45] H. Satzger, D. Townsend, M. Z. Zgierski, *et al.*. Primary processes underlying the photostability of isolated dna bases: Adenine. *Proceedings of the National Academy of Sciences* **103**(27) 10196–10201 (2006).

[46] D. Polli, P. Altoè, O. Weingart, *et al.*. Conical intersection dynamics of the primary photoisomerization event in vision. *Nature* **467**(7314) 440–443 (2010).

[47] J. Yuen-Zhou, J. J. Krich, I. Kassal, *et al.*. *Ultrafast Spectroscopy: Quantum information and wavepackets*. 2053-2563. IOP Publishing (2014). ISBN 978-0-750-31062-8.

[48] C. Ruckebusch, M. Sliwa, P. Pernot, *et al.*. Comprehensive data analysis of femtosecond transient absorption spectra: A review. *Journal of Photochemistry and Photobiology C: Photochemistry Reviews* **13**(1) 1–27 (2012).

[49] L. Gallmann, C. Cirelli, and U. Keller. Attosecond science: recent highlights and future trends. *Annual review of physical chemistry* **63** 447–469 (2012).

[50] E. Goulielmakis *et al.*. Real-time observation of valence electron motion. *Nature* **466**(7307) 739–743 (2010).

[51] C. Iaconis and I. A. Walmsley. Spectral phase interferometry for direct electric-field reconstruction of ultrashort optical pulses. *Optics letters* **23**(10) 792–794 (1998).

[52] R. Trebino. *Frequency-resolved optical gating: the measurement of ultrashort laser pulses*. Springer Science & Business Media (2012).

[53] J. R. Birge, R. Ell, and F. X. Kärtner. Two-dimensional spectral shearing interferometry for few-cycle pulse characterization. *Optics letters* **31**(13) 2063–2065 (2006).

[54] F. Silva, M. Miranda, B. Alonso, *et al.*. Simultaneous compression, characterization and phase stabilization of gw-level 1.4 cycle VIS-NIR femtosecond pulses using a single dispersion-scan setup. *Optics express* **22**(9) 10181–10191 (2014).

[55] A. Rundquist, C. G. Durfee, Z. Chang, *et al.*. Phase-matched generation of coherent soft x-rays. *Science* **280**(5368) 1412–1415 (1998).

[56] B. L. Henke, E. M. Gullikson, and J. C. Davis. X-ray interactions: photoabsorption, scattering, transmission, and reflection at e= 50-30,000 ev, z= 1-92. *Atomic data and nuclear data tables* **54**(2) 181–342 (1993).

[57] C. G. Durfee III, A. R. Rundquist, S. Backus, *et al.*. Phase matching of high-order harmonics in hollow waveguides. *Physical Review Letters* **83**(11) 2187 (1999).

[58] C. Winterfeldt, C. Spielmann, and G. Gerber. Colloquium: Optimal control of high-harmonic generation. *Reviews of Modern Physics* **80**(1) 117 (2008).

[59] A. Fleischer, O. Kfir, T. Diskin, *et al.*. Spin angular momentum and tunable polarization in high-harmonic generation. *Nature Photonics* **8**(7) 543–549 (2014).

[60] A. Ferré, C. Handschin, M. Dumergue, *et al.*. A table-top ultrashort light source in the extreme ultraviolet for circular dichroism experiments. *Nature Photonics* **9**(2) 93–98 (2015).

[61] M. Chini, K. Zhao, and Z. Chang. The generation, characterization and applications of broadband isolated attosecond pulses. *Nature Photonics* **8**(3) 178–186 (2014).

[62] H. . G. Muller. Reconstruction of attosecond harmonic beating by interference of two-photon transitions. *Applied Physics B* **74**(1) s17–s21 (2002).

[63] N. Hirisave Shivaram. *Attosecond Resolved Electron Wave Packet Dynamics in Helium*. Ph.D. thesis, The University of Arizona. (2013).

[64] C.-T. , A. Sandhu, S. Camp, *et al.*. Beyond the single-atom response in absorption line shapes: Probing a dense, laser-dressed helium gas with attosecond pulse trains. *Physical Review Letter* **114** 143002 (2015).

[65] F. Krausz and M. Ivanov. Attosecond physics. *Reviews of Modern Physics* **81**(1) 163–234 (2009).

[66] H. Wang, M. Chini, S. Chen, *et al.*. Attosecond time-resolved autoionization of argon. *Physical Review Letter* **105** 143002 (2010).

[67] M. Chini, B. Zhao, H. Wang, *et al.*. Subcycle ac stark shift of helium excited states probed with isolated attosecond pulses. *Physical Review Letter* **109** 073601 (2012).

[68] S. Chen, M. J. Bell, A. R. Beck, *et al.*. Light-induced states in attosecond transient absorption spectra of laser-dressed helium. *Physical Review A* **86** 063408 (2012).

[69] W.-C. Chu and C. D. Lin. Photoabsorption of attosecond XUV light pulses by two strongly laser-coupled autoionizing states. *Physical Review A* **85** 013409 (2012).

[70] C. Ott, A. Kaldun, P. Raith, *et al.*. Lorentz meets fano in spectral line shapes: A universal phase and its laser control. *Science* **340**(6133) 716–720 (2013).

[71] S. Chen, M. Wu, M. B. Gaarde, *et al.*. Laser-imposed phase in resonant absorption of an isolated attosecond pulse. *Physical Review A* **88** 033409 (2013).

[72] A. Kaldun, C. Ott, A. Blättermann, *et al.*. Extracting phase and amplitude modifications of laser-coupled fano resonances. *Physical Review Letter* **112** 103001 (2014).

[73] J. C. Delagnes and M. A. Bouchene. Gain-dispersion coupling induced by transient light shifts in an atomic medium. *Physical Review A* **76**(2) 023422 (2007).

[74] Z.-H. Loh, M. Khalil, R. E. Correa, *et al.*. A tabletop femtosecond time-resolved soft x-ray transient absorption spectrometer. *Review of Scientific Instruments* **79**(7) 073101 (2008).

[75] M. Lucchini, J. Herrmann, A. Ludwig, *et al.*. Role of electron wavepacket interference in the optical response of helium atoms. *New Journal of Physics* **15**(10) 103010 (2013).

[76] A. N. Pfeiffer, M. J. Bell, A. R. Beck, *et al.*. Alternating absorption features during attosecond-pulse propagation in a laser-controlled gaseous medium. *Physical Review A* **88**(5) 051402 (2013).

[77] M. B. Gaarde, C. Buth, J. L. Tate, *et al.*. Transient absorption and reshaping of ultrafast XUV light by laser-dressed helium. *Physical Review A* **83** 013419 (2011).

[78] W. C. Chu and C. D. Lin. Resonant enhancement of a single attosecond pulse in a gas medium by a time-delayed control field. *Journal of Physics B-Atomic Molecular and Optical Physics* **45**(20) 201002 (2012).

[79] M. Wu, S. Chen, K. J. Schafer, *et al.*. Ultrafast time-dependent absorption in a macroscopic three-level helium gas. *Physical Review A* **87** 013828 (2013).

[80] M. Schultze *et al.*. Controlling dielectrics with the electric field of light. *Nature* **493**(7430) 75–78 (2013).

[81] C. M. Jiang, L. R. Baker, J. M. Lucas, *et al.*. Characterization of photo-induced charge transfer and hot carrier relaxation pathways in spinel cobalt oxide (co3o4). *Journal of Physical Chemistry C* **118**(39) 22774–22784 (2014).

[82] C. Altucci, A. Nebbioso, R. Benedetti, *et al.*. Nonlinear protein - nucleic acid crosslinking induced by femtosecond uv laser pulses in living cells. *Laser Physics Letters* **9**(3) 234–239 (2012).

[83] U. van Bürck. Coherent pulse propagation through resonant media. *Hyperfine Interactions* **123/124**(1-4) 483 (1999).

[84] U. Fano. Effects of configuration interaction on intensities and phase shifts. *Physical Review* **124** 1866–1878 (1961).

[85] M. D. Crisp. Propagation of small-area pulses of coherent light through a resonant medium. *Physical Review A* **1**(6) 1604 (1970).

[86] J. K. Ranka, R. W. Schirmer, and A. L. Gaeta. Coherent spectroscopic effects in the propagation of ultrashort pulses through a two-level system. *Physical Review A* **57** R36–R39 (1998).

[87] D. Strasser, T. Pfeifer, B. J. Hom, *et al.*. Coherent interaction of femtosecond extreme-uv light with he atoms. *Physical Review A* **73**(2) 021805 (2006).

[88] C. Ott, A. Kaldun, L. Argenti, *et al.*. Reconstruction and control of a time-dependent two-electron wave packet. *Nature* **516**(18) 374 (2014).

[89] C.-T. Liao, A. Sandhu, S. Camp, *et al.*. Attosecond transient absorption in dense gases: Exploring the interplay between resonant pulse propagation and laser-induced line-shape control. *Physical Review A* **93** 033405 (2016).

[90] M. Hentschel, R. Kienberger, C. Spielmann, *et al.*. Attosecond metrology. *Nature* **414**(6863) 509–513 (2001).

[91] R. Schoenlein, L. Peteanu, R. Mathies, *et al.*. The first step in vision: femtosecond isomerization of rhodopsin. *Science* **254**(5030) 412–415 (1991).

[92] R. Berera, R. van Grondelle, and J. Kennis. Ultrafast transient absorption spectroscopy: principles and application to photosynthetic systems. *Photosynthesis Research* **101**(2-3) 105–118 (2009).

[93] L. Gallmann, C. Cirelli, and U. Keller. Attosecond science: Recent highlights and future trends. *Annual Review of Physical Chemistry* **63**(1) 447–469 (2012). PMID: 22404594.

[94] A. I. Kuleff and L. S. Cederbaum. Ultrafast correlation-driven electron dynamics. *Journal of Physics B-Atomic Molecular and Optical Physics* **47**(12) 124002 (2014).

[95] S. Pabst, A. Sytcheva, A. Moulet, *et al.*. Theory of attosecond transient-absorption spectroscopy of krypton for overlapping pump and probe pulses. *Physical Review A* **86** 063411 (2012).

[96] X. Wang, M. Chini, Y. Cheng, *et al.*. Subcycle laser control and quantum interferences in attosecond photoabsorption of neon. *Physical Review A* **87** 063413 (2013).

[97] M. Holler, F. Schapper, L. Gallmann, *et al.*. Attosecond electron wave-packet interference observed by transient absorption. *Physical Review Letter* **106** 123601 (2011).

[98] M. Chini, X. Wang, Y. Cheng, *et al.*. Sub-cycle Oscillations in Virtual States Brought to Light. *Sci. Rep.* **3** (2013).

[99] E. Hosler and S. Leone. Characterization of vibrational wave packets by core-level high-harmonic transient absorption spectroscopy. *Physical Review A* **88** 023420 (2013).

[100] C. M. Jiang, L. R. Baker, J. M. Lucas, *et al.*. Characterization of photo-induced charge transfer and hot carrier relaxation pathways in spinel cobalt oxide (co3o4). *Journal of Physical Chemistry C* **118**(39) 22774–22784 (2014).

[101] S. Chen, M. J. Bell, A. R. Beck, *et al.*. Light-induced states in attosecond transient absorption spectra of laser-dressed helium. *Physical Review A* **86** 063408 (2012).

[102] J. Herrmann, M. Weger, R. Locher, *et al.*. Virtual single-photon transition interrupted: Time-gated optical gain and loss. *Physical Review A* **88** 043843 (2013).

[103] C. Ott, A. Kaldun, P. Raith, *et al.*. Lorentz meets fano in spectral line shapes: A universal phase and its laser control. *Science* **340**(6133) 716–720 (2013).

[104] L. Argenti, A. Jiménez-Galán, C. Marante, *et al.*. Dressing effects in the attosecond transient absorption spectra of doubly excited states in helium. *Physical Review A* **91**(6) 061403 (2015).

[105] A. N. Pfeiffer, M. J. Bell, A. R. Beck, *et al.*. Alternating absorption features during attosecond-pulse propagation in a laser-controlled gaseous medium. *Physical Review A* **88**(5) 051402 (2013).

[106] W. C. Chu and C. D. Lin. Absorption and emission of single attosecond light pulses in an autoionizing gaseous medium dressed by a time-delayed control field. *Physical Review A* **87**(1) 013415 (2013).

[107] S. Chen, M. Wu, M. Gaarde, *et al.*. Laser-imposed phase in resonant absorption of an isolated attosecond pulse. *Physical Review A* **88** 033409 (2013).

[108] E. Perfetto and G. Stefanucci. Some exact properties of the nonequilibrium response function for transient photoabsorption. *Physical Review A* **91** 033416 (2015).

[109] E. Perfetto, A.-M. Uimonen, R. van Leeuwen, *et al.*. First-principles nonequilibrium green's function approach to transient photoabsorption: Application to atoms. *Physical Review A* **92** 033419 (2015).

[110] M. D. Crisp. Propagation of small-area pulses of coherent light through a resonant medium. *Physical Review A* **1**(6) 1604 (1970).

[111] G. LAMB. Analytical descriptions of ultrashort optical pulse propagation in a resonant medium. *Review Modern Physics* **43** 99–124 (1971).

[112] M. Bouchene. Phase control of dispersion effects for an ultrashort pulse train propagating in a resonant medium. *Physical Review A* **66** 065801 (2002).

[113] J. Delagnes and M. Bouchene. Gain-dispersion coupling induced by transient light shifts in an atomic medium. *Physical Review A* **76** 023422 (2007).

[114] L. Costanzo, A. Coelho, D. Pellegrino, *et al.*. Zero-area single-photon pulses. *Physical Review Letters* **116**(2) 023602 (2016).

[115] M. Reduzzi, J. Hummert, A. Dubrouil, *et al.*. Polarization-control of absorption of virtual dressed-states in helium. *Physical Review A* (to appear, 2015).

[116] M. B. Gaarde, C. Buth, J. L. Tate, *et al.*. Transient absorption and reshaping of ultrafast XUV light by laser-dressed helium. *Physical Review A* **83** 013419 (2011).

[117] M. Wu, S. Chen, S. Camp, *et al.*. Theory of strong-field attosecond transient absorption. *Journal of Physics B: Atomic, Molecular and Optical Physics* **49**(6) 062003 (2016).

[118] S. Chen, M. Wu, M. B. Gaarde, *et al.*. Laser-imposed phase in resonant absorption of an isolated attosecond pulse. *Physical Review A* **88**(3) 033409 (2013).

[119] C. Ott, A. Kaldun, P. Raith, *et al.*. Lorentz meets fano in spectral line shapes: a universal phase and its laser control. *Science* **340**(6133) 716–720 (2013).

[120] M. Chini, B. Zhao, H. Wang, *et al.*. Subcycle ac stark shift of helium excited states probed with isolated attosecond pulses. *Physical Review Letters* **109**(7) 073601 (2012).

[121] M. Holler, F. Schapper, L. Gallmann, *et al.*. Attosecond electron wave-packet interference observed by transient absorption. *Physical Review Letters* **106**(12) 123601 (2011).

[122] L. Armstrong Jr, B. L. Beers, and S. Feneuille. Resonant multiphoton ionization via the fano autoionization formalism. *Physical Review A* **12**(5) 1903 (1975).

[123] Y. I. Heller and A. Popov. Parametric generation and absorption of tunable vacuum-ultraviolet radiation controlled by laser-induced autoionizing-like resonances in the continuum. *Optics Communications* **18**(4) 449–451 (1976).

[124] P. L. Knight, M. Lauder, and B. J. Dalton. Laser-induced continuum structure. *Physics Reports* **190**(1) 1–61 (1990).

[125] N. Shivaram, H. Timmers, X.-M. Tong, *et al.*. Attosecond-resolved evolution of a laser-dressed helium atom: interfering excitation paths and quantum phases. *Physical Review Letters* **108**(19) 193002 (2012).

[126] T. Ding, C. Ott, A. Kaldun, *et al.*. Time-resolved four-wave-mixing spectroscopy for inner-valence transitions. *Optics Letters* **41**(4) 709–712 (2016).

[127] S.-I. Chu and D. A. Telnov. Beyond the floquet theorem: generalized floquet formalisms and quasienergy methods for atomic and molecular multiphoton processes in intense laser fields. *Physics reports* **390**(1) 1–131 (2004).

[128] X. Tong and N. Toshima. Controlling atomic structures and photoabsorption processes by an infrared laser. *Physical Review A* **81**(6) 063403 (2010).

[129] N. Shivaram, H. Timmers, X.-M. Tong, *et al.*. Measurement of the absolute timing of attosecond XUV bursts with respect to the driving field. *Physical Review A* **85**(5) 051802 (2012).

[130] N. Shivaram, H. Timmers, X.-M. Tong, *et al.*. Photoionization dynamics in the presence of attosecond pulse trains and strong fields. *Chemical physics* **414** 139–148 (2013).

[131] R. W. Boyd. Nonlinear optics. In *Handbook of Laser Technology and Applications (Three-Volume Set)*, 161–183. Taylor & Francis (2003).

[132] S. Chakrabarti, H. Muench, and T. Halfmann. Adiabatically driven frequency conversion towards short extreme-ultraviolet radiation pulses. *Physical Review A* **82**(6) 063817 (2010).

[133] T. Rickes, J. Marangos, and T. Halfmann. Enhancement of third-harmonic generation by stark-chirped rapid adiabatic passage. *Optics communications* **227**(1) 133–142 (2003).

[134] A. Popov, V. V. Kimberg, and T. F. George. Large enhancement of fully resonant sum-frequency generation through quantum control via continuum states. *Physical Review A* **69**(4) 043816 (2004).

[135] R. Hodgson, P. Sorokin, and J. J. Wynne. Tunable coherent vacuum-ultraviolet generation in atomic vapors. *Physical Review Letters* **32**(7) 343 (1974).

[136] W. Cao, E. R. Warrick, A. Fidler, *et al.*. Noncollinear wave mixing of attosecond XUV and few-cycle optical laser pulses in gas-phase atoms: Toward multidimensional spectroscopy involving XUV excitations. *Physical Review A* **94**(5) 053846 (2016).

[137] W. Cao, E. R. Warrick, A. Fidler, *et al.*. Near-resonant four-wave mixing of attosecond extreme-ultraviolet pulses with near-infrared pulses in neon: Detection of electronic coherences. *Physical Review A* **94**(2) 021802 (2016).

[138] B. Ritchie. Third-harmonic generation from a laser-induced autoionizing level. *Physical Review A* **31**(2) 823 (1985).

[139] B.-n. Dai and P. Lambropoulos. Laser-induced autoionizinglike behavior, population trapping, and stimulated raman processes in real atoms. *Physical Review A* **36**(11) 5205 (1987).

[140] L. Yatsenko, B. Shore, T. Halfmann, *et al.*. Source of metastable h (2s) atoms using the stark chirped rapid-adiabatic-passage technique. *Physical Review A* **60**(6) R4237 (1999).

[141] C.-T. Liao, X. Li, D. J. Haxton, *et al.*. Probing autoionizing states of molecular oxygen with XUV transient absorption: Electronic-symmetry-dependent line shapes and laser-induced modifications. *Physical Review A* **95** 043427 (2017).

[142] U. Becker and D. A. Shirley. *VUV and Soft X-ray Photoionization*. Springer Science & Business Media (2012).

[143] C.-Y. Ng. *Vacuum ultraviolet photoionization and photodissociation of molecules and clusters*. World Scientific (1991).

[144] R. L. Platzman. Superexcited states of molecules. *Radiation Research* **17**(3) 419–425 (1962).

[145] Y. Hatano. Interaction of vacuum ultraviolet photons with molecules. formation and dissociation dynamics of molecular superexcited states. *Physics Reports-Review Section of Physics Letters* **313**(3) 110–169 (1999).

[146] H. Nakamura. What are the basic mechanisms of electronic transitions in molecular dynamic processes? *International Reviews in Physical Chemistry* **10**(2) 123–188 (1991).

[147] R. P. Wayne. *Chemistry of Atmosphere: An Introduction to the Chemistry of the Atmosphere of Earth, the Planets and Their Satellites*. Oxford, Clarendon (1991).

[148] B. Boudaıffa, P. Cloutier, D. Hunting, *et al.*. Resonant formation of dna strand breaks by low-energy (3 to 20 ev) electrons. *Science* **287**(5458) 1658–1660 (2000).

[149] A. Florescu-Mitchell and J. Mitchell. Dissociative recombination. *Physics Reports* **430** 277 – 374 (2006).

[150] V. Kokoouline, N. Douguet, and C. H. Greene. Breaking bonds with electrons: Dissociative recombination of molecular ions. *Chemical Physics Letters* **507** 1 – 10 (2011).

[151] N. Douguet, A. E. Orel, C. H. Greene, *et al.*. Dissociative recombination of highly symmetric polyatomic ions. *Physical Review Letter* **108** 023202 (2012).

[152] V. Kokoouline, C. H. Greene, and B. D. Esry. Mechanism for the destruction of O_3^+ ions by electron impact. *Nature* **412**(6850) 891–894 (2001).

[153] S. L. Guberman and A. Giusti-Suzor. The generation of $O(^1s)$ from the dissociative recombination of O_2^+. *The Journal of Chemical Physics* **95**(4) 2602–2613 (1991).

[154] C. Jungen and S. T. Pratt. Low-energy dissociative recombination in small polyatomic molecules. *The Journal of Chemical Physics* **133**(21) 214303 (2010).

[155] A. Rundquist, C. G. Durfee, Z. Chang, *et al.*. Phase-matched generation of coherent soft x-rays. *Science* **280**(5368) 1412–1415 (1998).

[156] P. Paul, E. Toma, P. Breger, *et al.*. Observation of a train of attosecond pulses from high harmonic generation. *Science* **292**(5522) 1689–1692 (2001).

[157] E. Gagnon, P. Ranitovic, X.-M. Tong, *et al.*. Soft x-ray-driven femtosecond molecular dynamics. *Science* **317**(5843) 1374–1378 (2007).

[158] A. S. Sandhu, E. Gagnon, R. Santra, *et al.*. Observing the creation of electronic feshbach resonances in soft x-ray–induced O_2 dissociation. *Science* **322**(5904) 1081–1085 (2008).

[159] E. Goulielmakis, Z.-H. Loh, A. Wirth, *et al.*. Real-time observation of valence electron motion. *Nature* **466**(7307) 739–743 (2010).

[160] H. Wang, M. Chini, S. Chen, *et al.*. Attosecond time-resolved autoionization of argon. *Physical Review Lett.* **105**(14) 143002 (2010).

[161] M. Chini, B. Zhao, H. Wang, *et al.*. Subcycle ac stark shift of helium excited states probed with isolated attosecond pulses. *Physical Review Letters* **109**(7) 073601 (2012).

[162] S. Chen, M. J. Bell, A. R. Beck, *et al.*. Light-induced states in attosecond transient absorption spectra of laser-dressed helium. *Physical Review A* **86**(6) 063408 (2012).

[163] M. Holler, F. Schapper, L. Gallmann, *et al.*. Attosecond electron wave-packet interference observed by transient absorption. *Physical Review Letter* **106**(12) 123601 (2011).

[164] E. R. Warrick, W. Cao, D. M. Neumark, *et al.*. Probing the dynamics of Rydberg and valence states of molecular nitrogen with attosecond transient absorption spectroscopy. *The Journal of Physical Chemistry A* **120** 3165 (2016).

[165] M. Reduzzi, W. Chu, C. Feng, *et al.*. Observation of autoionization dynamics and sub-cycle quantum beating in electronic molecular wave packets. *Journal of Physics B: Atomic, Molecular and Optical Physics* **49**(6) 065102 (2016).

[166] A. E. Miroshnichenko, S. Flach, and Y. S. Kivshar. Fano resonances in nanoscale structures. *Review Modern Physics* **82** 2257–2298 (2010).

[167] U. Fano. Effects of configuration interaction on intensities and phase shifts. *Physical Review* **124**(6) 1866–1878 (1961).

[168] F. R. Gilmore. Potential energy curves for N_2, NO, O_2 and corresponding ions. *Journal of Quantitative Spectroscopy and Radiative Transfer* **5**(2) 369 – IN3 (1965).

[169] P. Baltzer, B. Wannberg, L. Karlsson, *et al.*. High-resolution inner-valence uv photoelectron spectra of the O_2 molecule and configuration-interaction calculations of $^2\Pi_u$ states between 20 and 26 ev. *Physical Review A* **45** 4374–4384 (1992).

[170] A. Ehresmann, L. Werner, S. Klumpp, *et al.*. De-excitation dynamics of Rydberg states in O_2. *Journal of Physics B: Atomic, Molecular and Optical Physics* **37**(22) 4405 (2004).

[171] C. Ott, A. Kaldun, L. Argenti, *et al.*. Reconstruction and control of a time-dependent two-electron wave packet. *Nature* **516**(7531) 374–378 (2014).

[172] M. Wu, S. Chen, S. Camp, *et al.*. Theory of strong-field attosecond transient absorption. *J. Phys. B: Atom. Mol. Phys.* **49**(6) 062003 (2016).

[173] R. E. Stratmann and R. R. Lucchese. A graphical unitary group approach to study multiplet specific multichannel electron correlation effects in the photoionization of O_2. *Journal of Chemical Physics* **102**(21) 8493–8505 (1995).

[174] R. E. Stratmann, R. W. Zurales, and R. R. Lucchese. Multiplet-specific multichannel electron-correlation effects in the photoionization of no. *Journal of Chemical Physics* **104**(22) 8989–9000 (1996).

[175] J. Dunning, Thom H. Gaussian basis sets for use in correlated molecular calculations. i. the atoms boron through neon and hydrogen. *Journal of Chemical Physics* **90**(2) 1007–1023 (1989).

[176] R. A. Kendall, J. Dunning, Thom H., and R. J. Harrison. Electron affinities of the first-row atoms revisited. systematic basis sets and wave functions. *Journal of Chemical Physics* **96**(9) 6796–6806 (1992).

[177] C. R. Wu. Assignments of autoionization states of O_2. *Journal of Quantitative Spectroscopy and Radiative Transfer* **37**(1) 1 – 15 (1987).

[178] O. E. Alon, A. I. Streitsov, and L. S. Cederbaum. Unified view on multi-configurational time propagation for systems consisting of identical particles. *Journal of Chemical Physics* **127** 154103 (2007).

[179] J. Caillat *et al.*. Correlated multielectron systems in strong laser fields: A multiconfiguration time-dependent hartree-fock approach. *Physical Review A* **71** 012712 (2005).

[180] T. Kato and H. Kono. Time-dependent multiconfiguration theory for ultrafast electronic dynamics of molecules in an intense laser field: Electron correlation and energy redistribution among natural orbitals. *Chemical Physics* **366** 46 (2009).

[181] I. S. Ulusoy and M. Nest. The multi-configuration electron-nuclear dynamics method applied to lih. *Journal of Chemical Physics* **136** 054112 (2012).

[182] R. P. Miranda, A. J. Fisher, L. Stella, *et al.*. A multiconfigurational time-dependent hartree-fock method for excited electronic states. i. general formalism and application to open-shell states. *Journal of Chemical Physics* **134** 244101 (2011).

[183] H. Miyagi and L. B. Madsen. Time-dependent restricted-active-space self-consistent-field theory for laser-driven many-electron dynamics. *Physical Review A* **87** 062511 (2013).

[184] T. Sato and K. L. Ishikawa. Time-dependent complete-active-space self-consistent-field method for multielectron dynamics in intense laser fields. *Physical Review A* **88** 023402 (2013).

[185] D. J. Tannor. *Introduction to Quantum Mechanics: A Time Dependent Perspective*. University Science Press, Sausalito (2007).

[186] M. B. Gaarde, C. Buth, J. T. Tate, *et al.*. Transient absorption and reshaping of ultrafast XUV light by laser-dressed helium. *Physical Review A* **83** 013419 (2011).

[187] W.-C. Chu and C. Lin. Absorption and emission of single attosecond light pulses in an autoionizing gaseous medium dressed by a time-delayed control field. *Physical Review A* **87**(1) 013415 (2013).

[188] D. Cubric, A. Wills, J. Comer, *et al.*. Selective population of spin-orbit levels in the autoionization of O_2. *Journal of Physics B: Atomic, Molecular and Optical Physics* **26**(18) 3081 (1993).

[189] H. Liebel, S. Lauer, F. Vollweiler, *et al.*. Neutral photodissociation of O_2 Rydberg states accompanied by changes of the Rydberg electron's quantum numbers n and l. *Physics Letters A* **267**(5) 357–369 (2000).

[190] H. Liebel, A. Ehresmann, H. Schmoranzer, *et al.*. De-excitation dynamics of Rydberg states in O_2. *Journal of Physics B: Atomic, Molecular and Optical Physics* **35**(4) 895 (2002).

[191] Y. Hikosaka, P. Lablanquie, M. Ahmad, *et al.*. Competition between autoionization and dissociation in the $[O_2^+ (b^2\Sigma_g^-)]$ nl and $[O_2^+ (c^4\Sigma_u^-)]$ nl Rydberg states investigated by photon-induced dissociation to neutral fragments. *Journal of Physics B: Atomic, Molecular and Optical Physics* **36**(21) 4311 (2003).

[192] B. Doughty, C. J. Koh, L. H. Haber, *et al.*. Ultrafast decay of superexcited $c^4\Sigma_u^-$ $nl\sigma_g$ ν=0,1 states of O_2 probed with femtosecond photoelectron spectroscopy. *Journal of Chemical Physics* **136**(21) 214303 (2012).

[193] H. Lefebvre-Brion and R. W. Field. *The Spectra and Dynamics of Diatomic Molecules*. Elsevier Inc. (2004).

[194] X. Li, B. Bernhardt, A. R. Beck, *et al.*. Investigation of coupling mechanisms in attosecond transient absorption of autoionizing states: comparison of theory and experiment in xenon. *Journal of Physics B: Atomic, Molecular and Optical Physics* **48**(12) 125601 (2015).

[195] A. Padmanabhan, M. MacDonald, C. Ryan, *et al.*. An angle-resolved dissociative photoionization study of the $c^4\Sigma_u^-$ state in O_2^+ using the tpepico technique. *Journal of Physics B: Atomic, Molecular and Optical Physics* **43**(16) 165204 (2010).

[196] J. E. Bækhøj, L. Yue, and L. B. Madsen. Nuclear-motion effects in attosecond transient-absorption spectroscopy of molecules. *Physical Review A* **91** 043408 (2015).

[197] B. Bernhardt, A. R. Beck, X. Li, *et al.*. High-spectral-resolution attosecond absorption spectroscopy of autoionization in xenon. *Physical Review A* **89** 023408 (2014).

[198] A. N. Pfeiffer, M. J. Bell, A. R. Beck, *et al.*. Alternating absorption features during attosecond-pulse propagation in a laser-controlled gaseous medium. *Physical Review A* **88** 051402 (2013).

[199] X. Li, B. Bernhardt, B. A. R., *et al.*. Investigation of coupling mechanisms in attosecond transient absorption of auto-ionizing states: comparison of theory and experiment in xenon. *Journal of Physics B: Atomic, Molecular and Optical Physics* **87**(1) 013415 (2015).

[200] M. Eckstein, C.-H. Yang, F. Frassetto, *et al.*. Direct imaging of transient fano resonances in n 2 using time-, energy-, and angular-resolved photoelectron spectroscopy. *Physical Review Letters* **116**(16) 163003 (2016).

[201] D. J. Haxton, K. V. Lawler, and C. W. McCurdy. Multiconfiguration time-dependent hartree-fock treatment of electronic and nuclear dynamics in diatomic molecules. *Physical Review A* **83** 063416 (2011).

[202] U. Fano and J. Cooper. Spectral distribution of atomic oscillator strengths. *Reviews of Modern Physics* **40**(3) 441 (1968).

[203] W. Westerveld, T. Mulder, and J. van Eck. Determination of oscillator strengths from the self-absorption of resonance radiation in rare gases–ii. neon and argon. *Journal of Quantitative Spectroscopy and Radiative Transfer* **21**(6) 533 – 546 (1979).

[204] R. Madden, D. Ederer, and K. Codling. Resonances in the photo-ionization continuum of ar i (20-150 ev). *Physical Review* **177**(1) 136 (1969).

[205] S. Wu, Z. Zhong, R. Feng, *et al.*. Electron-impact study in valence and autoionization resonance regions of argon. *Physical Review A* **51**(6) 4494 (1995).

[206] N. Berrah, B. Langer, J. Bozek, *et al.*. Angular-distribution parameters and r-matrix calculations of ar resonances. *Journal of Physics B: Atomic, Molecular and Optical Physics* **29**(22) 5351 (1996).

[207] Z. Lin-Fan, C. Hua-Dong, L. Xiao-Jing, *et al.*. Optically forbidden excitations of 3s electron of argon by fast electron impact. *Chinese physics letters* **20**(10) 1718 (2003).

[208] B. W. Shore. Scattering theory of absorption-line profiles and refractivity. *Reviews of Modern Physics* **39**(2) 439 (1967).

[209] B. W. Shore. Analysis of absorption profiles of autoionizing lines. *JOSA* **57**(7) 881–884 (1967).

[210] B. W. Shore. Parametrization of absorption-line profiles. *Physical Review* **171**(1) 43 (1968).

[211] L. Huang, Y.-C. Lai, H.-G. Luo, *et al.*. Universal formalism of fano resonance. *AIP Advances* **5**(1) 017137 (2015).

[212] A. Bärnthaler, S. Rotter, F. Libisch, *et al.*. Probing decoherence through fano resonances. *Physical Review Letters* **105**(5) 056801 (2010).

[213] A. Clerk, X. Waintal, and P. Brouwer. Fano resonances as a probe of phase coherence in quantum dots. *Physical Review Letters* **86**(20) 4636 (2001).

[214] A. Zielinski, V. P. Majety, S. Nagele, *et al.*. Anomalous fano profiles in external fields. *Physical Review Letters* **115**(24) 243001 (2015).

[215] N. Shivaram, X.-M. Tong, H. Timmers, *et al.*. Attosecond quantum-beat spectroscopy in helium. *Journal of Physics B: Atomic, Molecular and Optical Physics* **49**(5) 055601 (2016).

[216] T. Carette, J. Dahlström, L. Argenti, *et al.*. Multiconfigurational hartree-fock close-coupling ansatz: Application to the argon photoionization cross section and delays. *Physical Review A* **87**(2) 023420 (2013).

[217] Á. Jiménez-Galán, F. Martín, and L. Argenti. Two-photon finite-pulse model for resonant transitions in attosecond experiments. *Physical Review A* **93**(2) 023429 (2016).

[218] P. Lambropoulos and P. Zoller. Autoionizing states in strong laser fields. *Physical Review A* **24**(1) 379 (1981).

[219] A. Arora and S. Ghosh. A twisted periscope arrangement for transporting elliptically polarized light without change in its polarization state. *Review of Scientific Instruments* **81**(12) 123102 (2010).

[220] A. Trabattoni, M. Klinker, J. González-Vázquez, *et al.*. Mapping the dissociative ionization dynamics of molecular nitrogen with attosecond time resolution. *Physical Review X* **5** 041053 (2015).

[221] T. Okino, Y. Furukawa, Y. Nabekawa, *et al.*. Direct observation of an attosecond electron wave packet in a nitrogen molecule. *Science advances* **1**(8) e1500356 (2015).

[222] M. Eckstein, C.-H. Yang, F. Frassetto, *et al.*. Direct imaging of transient fano resonances in n2 using time-, energy-, and angular-resolved photoelectron spectroscopy. *Physical Review Letters* **116**(16) 163003 (2016).

[223] M. Eckstein, C.-H. Yang, M. Kubin, *et al.*. Dynamics of n2 dissociation upon inner-valence ionization by wavelength-selected XUV pulses. *The journal of physical chemistry letters* **6**(3) 419–425 (2015).

[224] Y. Cheng, M. Chini, X. Wang, *et al.*. Reconstruction of an excited-state molecular wave packet with attosecond transient absorption spectroscopy. *Physical Review A* **94**(2) 023403 (2016).

[225] J. E. Bækhøj, L. Yue, and L. B. Madsen. Nuclear-motion effects in attosecond transient-absorption spectroscopy of molecules. *Physical Review A* **91**(4) 043408 (2015).

[226] J. E. Bækhøj and L. B. Madsen. Light-induced structures in attosecond transient-absorption spectroscopy of molecules. *Physical Review A* **92**(2) 023407 (2015).

[227] J. E. Bækhøj and L. B. Madsen. Attosecond transient-absorption spectroscopy on aligned molecules. *Physical Review A* **94**(4) 043414 (2016).

[228] E. R. Warrick, W. Cao, D. M. Neumark, *et al.*. Probing the dynamics of Rydberg and valence states of molecular nitrogen with attosecond transient absorption spectroscopy. *The Journal of Physical Chemistry A* (2016).

[229] M. Reduzzi, W. Chu, C. Feng, *et al.*. Observation of autoionization dynamics and sub-cycle quantum beating in electronic molecular wave packets. *Journal of Physics B: Atomic, Molecular and Optical Physics* **49**(6) 065102 (2016).

[230] E. R. Warrick, J. E. Bækhøj, W. Cao, *et al.*. Attosecond transient absorption spectroscopy of molecular nitrogen: Vibrational coherences in the b' state. *Chemical Physics Letters* (2017).

[231] J. E. Furst, T. J. Gay, J. Machacek, *et al.*. Orientation of doubly excited states in N_2. *Physical Review A* **86** 041401 (2012).

[232] H. Yoshii, T. Tanaka, Y. Morioka, *et al.*. New N_2^+ electronic states in the region of 23–28 ev. *Journal of molecular spectroscopy* **186**(1) 155–161 (1997).

[233] M. Ukai, K. Kameta, N. Kouchi, *et al.*. Neutral decay of double-holed doubly excited resonances of N_2. *Physical Review A* **46**(11) 7019 (1992).

[234] K. Codling. Structure in the photo-ionization continuum of N_2 near 500 å. *The Astrophysical Journal* **143** 552 (1966).

[235] D. Shaw, D. Holland, M. MacDonald, *et al.*. A study of the absolute photoabsorption cross section and the photionization quantum efficiency of nitrogen from the ionization threshold to 485 å. *Chemical physics* **166**(3) 379–391 (1992).

[236] P. Langhoff, S. Langhoff, T. Rescigno, *et al.*. Theoretical studies of inner-valence-shell photoionization cross sections in N_2 and CO. *Chemical Physics* **58**(1) 71–91 (1981).

[237] A. Tabche-Fouhaile, K. Ito, I. Nenner, *et al.*. N_2^+ (A $\rightarrow$ X) and N_2^+ (B $\rightarrow$ X) fluorescence excitation spectra by photon impact. *The Journal of Chemical Physics* **77**(1) 182–188 (1982).

[238] L. Berg, P. Erman, E. Källne, *et al.*. Studies of photoionization and photodissociation of N_2 in the 15-30 ev region using intense synchrotron radiation. *Physica Scripta* **44**(2) 131 (1991).

[239] G. Wendin. Collective effects, relaxation, and localization of hole levels in atoms, molecules, solids, and adsorbates. *International Journal of Quantum Chemistry* **16**(S13) 659–670 (1979).

[240] P. Sannes and L. Veseth. Doubly excited autoionizing states in N_2. *Physical Review A* **56** 2893–2902 (1997).

[241] P. Erman, A. Karawajczyk, E. Rachlew-Källne, *et al.*. Neutral dissociation by non-Rydberg doubly excited states. *Physical Review A* **60** 426–430 (1999).

[242] P. Bolognesi, G. Alberti, D. Thompson, *et al.*. A study of the partial photoionization cross sections of the N_2 valence-shell states. *Journal of Physics B: Atomic, Molecular and Optical Physics* **37**(23) 4575 (2004).

[243] A. Ferré, D. Staedter, F. Burgy, *et al.*. High-order harmonic transient grating spectroscopy of SF_6 molecular vibrations. *Journal of Physics B: Atomic, Molecular and Optical Physics* **47**(12) 124023 (2014).

[244] N. L. Wagner, A. Wüest, I. P. Christov, *et al.*. Monitoring molecular dynamics using coherent electrons from high harmonic generation. *Proceedings of the National Academy of Sciences* **103**(36) 13279–13285 (2006).

[245] Y. Pertot, C. Schmidt, M. Matthews, *et al.*. Time-resolved x-ray absorption spectroscopy with a water window high-harmonic source. *Science* aah6114 (2017).

[246] T. Gustafsson. Partial photoionization cross sections of SF_6 between 20 and 54 ev: An interpretation of the photoelectron spectrum. *Physical Review A* **18** 1481–1489 (1978).

[247] J. L. Dehmer, A. C. Parr, S. Wallace, *et al.*. Photoelectron branching ratios and angular distributions for the valence levels of SF_6 in the range $16 \leq h\nu \leq 30$ ev. *Physical Review A* **26** 3283–3292 (1982).

[248] V. Nefedov. Quasistationary states in x-ray absorption spectra of chemical compounds. *Journal of Structural Chemistry* **11**(2) 272–276 (1970).

[249] K. Sze and C. Brion. Inner-shell and valence-shell electronic excitation of SF_6, SeF_6 and TeF_6 by high energy electron impact: An investigation of potential barrier effects. *Chemical Physics* **140**(3) 439–472 (1990).

[250] T. Ferrett, D. Lindle, P. Heimann, *et al.*. Shape-resonant and many-electron effects in the s 2p photoionization of SF_6. *The Journal of Chemical Physics* **89**(8) 4726–4736 (1988).

[251] H. Nakamatsu, T. Mukoyama, and H. Adachi. Theoretical x-ray absorption spectra of SF_6 and H_2S. *The Journal of Chemical Physics* **95**(5) 3167–3174 (1991).

[252] A. Javan, W. R. Bennett Jr, and D. R. Herriott. Population inversion and continuous optical maser oscillation in a gas discharge containing a he-ne mixture. *Physical Review Letters* **6**(3) 106 (1961).

[253] A. White and J. Rigden. Continuous gas maser operation in visible. *Proceedings of the Institute of Radio Engineers* **50**(7) 1697 (1962).

[254] G. C. Tabisz and M. Neuman. *Collision-and interaction-induced spectroscopy*, volume 452. Springer Science & Business Media (2012).

[255] W. F. Huebner and W. D. Barfield. *Opacity*. Springer (2014).

[256] A. Maryott and G. Birnbaum. Collision-induced microwave absorption in compressed gases. i. dependence on density, temperature, and frequency in CO_2. *The Journal of Chemical Physics* **36**(8) 2026–2032 (1962).

[257] G. Birnbaum, H. B. Levine, and D. A. McQuarrie. Determination of two-and three-body relaxation times from collision-induced absorption. *The Journal of Chemical Physics* **46**(5) 1557–1561 (1967).

[258] H. B. Levine and G. Birnbaum. Classical theory of collision-induced absorption in rare-gas mixtures. *Physical Review* **154**(1) 86 (1967).

[259] M. El-Kader. Collision-induced absorption (cia) spectra and ground-state potentials of inert gas mixtures. *Journal of Quantitative Spectroscopy and Radiative Transfer* **112**(10) 1533–1542 (2011).

[260] H. Ferkel, A. Koch, and R. Feltgen. Fine-structure transitions in metastable $Ne^*(^3P_{0,2})$ colliding with ground state rare gases at thermal energies. *The Journal of chemical physics* **100**(4) 2690–2696 (1994).

[261] P. K. Leichner, J. D. Cook, and S. J. Luerman. Time dependence of the vacuum-uv emissions from neon, and energy transfers to the resonance states $Ne(^1p_1)$ and $Ne(^3p_1)$ in helium-neon mixtures. *Physical Review A* **12** 2501–2513 (1975).

[262] X. Wang, M. Chini, Y. Cheng, *et al.*. Subcycle laser control and quantum interferences in attosecond photoabsorption of neon. *Physical Review A* **87** 063413 (2013).

[263] A. R. Beck, B. Bernhardt, E. R. Warrick, *et al.*. Attosecond transient absorption probing of electronic superpositions of bound states in neon: detection of quantum beats. *New Journal of Physics* **16**(11) 113016 (2014).

[264] P. B. Corkum and F. Krausz. Attosecond science. *Nature Physics* **3**(6) 381–387 (2007).

[265] M. Schultze, K. Ramasesha, C. Pemmaraju, *et al.*. Attosecond band-gap dynamics in silicon. *Science* **346**(6215) 1348–1352 (2014).

[266] R. Won. Photovoltaics: graphene-silicon solar cells. *Nature Photonics* **4**(7) 411 (2010).

[267] E. Goulielmakis, V. S. Yakovlev, A. L. Cavalieri, *et al.*. Attosecond control and measurement: lightwave electronics. *Science* **317**(5839) 769–775 (2007).

[268] F. Krausz and M. I. Stockman. Attosecond metrology: from electron capture to future signal processing. *Nature Photonics* **8**(3) 205–213 (2014).